The morphological identity of insect dendrites

Friedrich Förstner

München 2010

The morphological identity
of insect dendrites

Friedrich Förstner

Dissertation

zur Erlangung des Doktorgrades
der Naturwissenschaften (Dr. rer. nat.)
an der Fakultät für Biologie
der Ludwig–Maximilians–Universität München

Angefertigt am Max-Planck-Institut für Neurobiologie
Abteilung Neuronale Informationsverarbeitung

vorgelegt von
Friedrich Förstner
aus Heidelberg

München 2010

Contents

1 summary

Dendrite morphology is the most prominent feature of nerve cells, investigated since the origins of modern neuroscience. The last century of neuroanatomical research has revealed an overwhelming diversity of different dendritic shapes and complexities. Its great variability, however, largely interferes with understanding the underlying principles of neuronal wiring and its functional implications.

This work addresses this issue by studying a morphological and functional exceptionally conserved network of neurons located in the visual system of flies. Lobula Plate Tangential Cells (LPTCs) have been shown to compute motion vision and contribute to the impressive flight capabilities of flies. Cells of this system exhibit a high degree of constancy in topographic location, morphology and function over all individuals of one species. This constancy allows investigation of functionally identical cells over a large population of flies, and therefore potentially to truly understand the underlying principles of their morphologies.

Supported by a large database of *in vivo* cell reconstructions and a computational quantification framework, it was possible to uncover some of those principles of LPTC anatomy. We show that the key to the cells' morphological identity lies in the size and shape of the area they span into. Their detailed branching structure and topology is then merely a result of a common growth program shared by all analyzed cells. Application of a previously published branching theory confirmed this finding. When grown into the spanning fields obtained from the *in vivo* cell reconstruction, artificial cells could be synthesized that resembled all anatomical properties that characterize their natural counterparts.

Furthermore, the morphological comparison of the same identified cells in *Calliphora* and *Drosophila* allowed to study a functionally conserved system under the influence of extensive down-scaling. The huge size reduction did not affect the underlying branching principles: *Drosophila* LPTCs followed the very same rules as their *Calliphora* counterparts. On the other hand, we observed significant differences in complexity and relative diameter scaling. An electrotonic analysis revealed that these differences can be explained by a common functional architecture implemented in the LPTCs of both species.

Finally, we could modify the LPTC neuronal interaction behavior thanks to the genetical

accessibility of *Drosophila*'s wiring program. The transmembrane protein family Dscam has been shown to mediate the process of adhesion and repulsion of neurites. By manipulating the molecular Dscam profile in *Drosophila* LPTCs it was possible to change their morphological expansion. The low variability of the LPTCs spanning field in wild type flies and their two-dimensional extension allowed to thoroughly map these morphological alterations in flies with Dscam modifications. In line with the LPTCs retinotopic input arrangement, electrophysiological experiments yielded an inherent linear relationship of their locally reduced dendritic coverage and their locally reduced stimulus sensitivity.

With this work I hope to contribute to the general understanding of neuronal morphology of LPTCs and to present a valuable workflow for the analysis of neuronal structure.

2 introduction

2.1 the fly visual system

LPTCs

The *Calliphora* fly brain consists of an estimated number of several hundreds of thousand cells and the visual system represents the most prominent sensory system by numbers (Strausfeld, 1976). This correlates with the high contribution of vision to the general behavior of the fly (Fig. 2.1A). Many behavioral and functional components of the visual circuitry have been investigated down to the level of network and even cellular implementations (Borst et al., 2010; Fischbach and Hiesinger, 2008). The Lobula Plate Tangential Cells (LPTC) represent one of these functionally defined networks. Decades ago, this anatomically and functionally compact network has been identified as one of the key structures in the processing of motion information (Hausen, 1984; Borst and Haag, 2002). In *Calliphora* flies it consists of around 60 partly interconnected cells. Due to their stereotyped appearance, size and an axonal thickness of 10 μm and their mainly planar extension without self-overlapping dendrites they allow access to a wide range of currently available research techniques in electrophysiology and microscopy - *in vivo* (Fig. 2.1B).
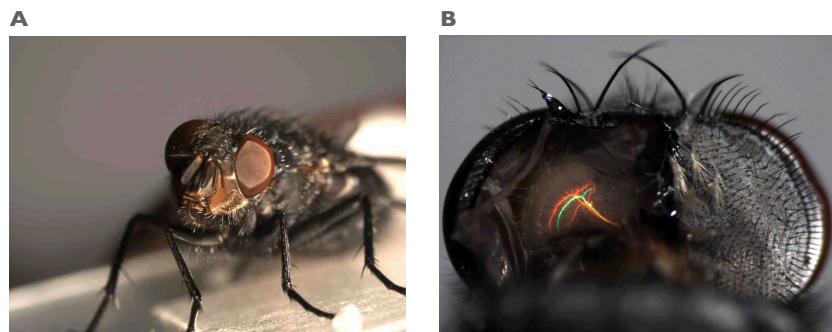
Figure 2.1: Lobula Plate Tangential Cells in Calliphora vicina. (A) Close-up of a female *Calliphora vicina*, big facet eyes shape the head of the fly. (B) Look into the lobula plate of *Calliphora* fly with three fluorescent dye filled Lobula Plate Tangential Cells (Haag and Borst, 2004)

input arrangement

While the biological implementation is part of ongoing research it is assumed that the LPTCs input can be modeled as an array of elementary motion detectors (EMDs). EMDs supply motion information at the level of a single facet (corresponding to a "pixel" in the visual image) for up-, down-, left- and rightward motion of the visual scene of the fly (Haag et al., 2004; Borst et al., 2010). The neighborhood relationship of each of these channels is preserved from the Retina down to the lobula plate. This implies that the visual input can be mapped directly to the input arrangement of the lobula plate. For example, movements in the frontal hemisphere lead to activation of cells in the lateral area of the LP, movements in the back (caudal) to activation of cells
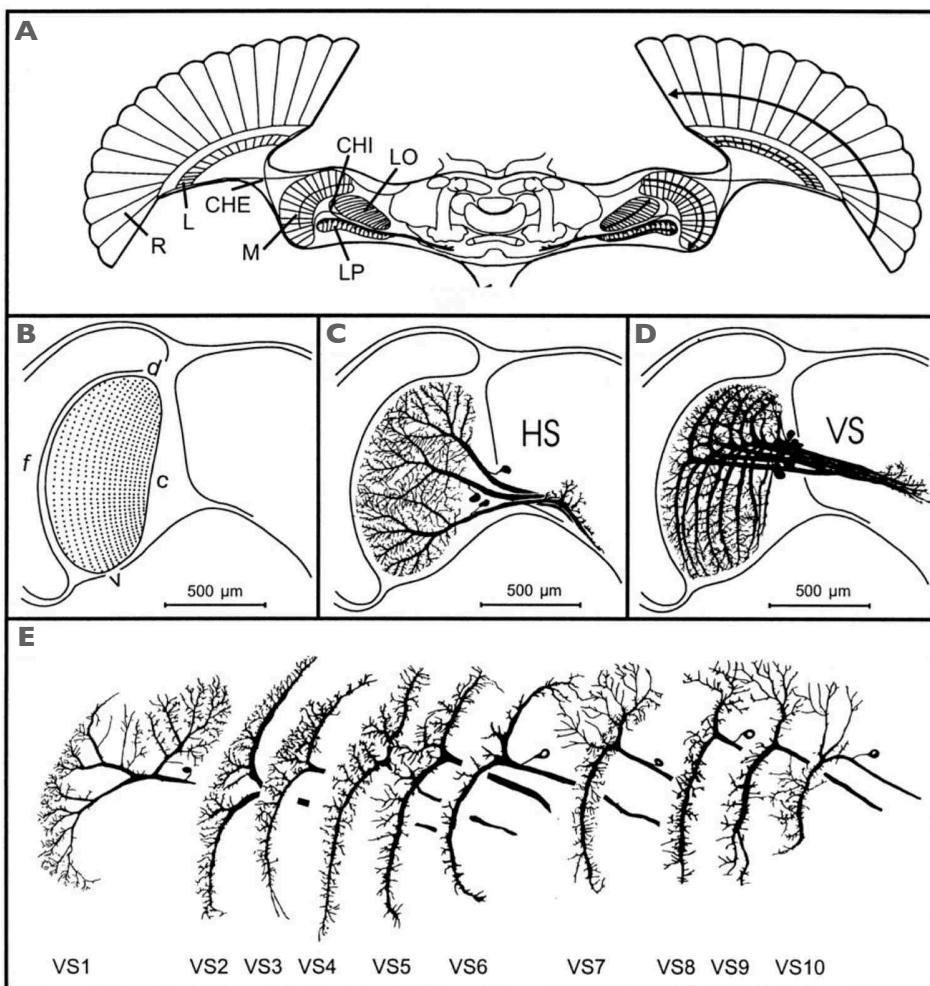
Figure 2.2: The visual system of flies. (A) Overview of the visual lobes and cascade of motion processing from the Retina (R), to the Lamina (L), Medula (M), Lobula (LO) and the lobula plate (LP). CHE and CHI indicate the two optical fiber tract chiasms, where the orientation of the visual input map is mirrored (B) Estimated input organization at the level of the lobula plate: each dot on the surface of the lobula plate represents one columnar input. (C) Drawing of the three cells of the horizontal system (HS) based on cobalt-impregnations. The 10 cells of the vertical system (VS) together (D) and separated out (E). HS and VS cells can be identified by their location in the lobula plate, their distinct morphology and their response properties (from Krapp et al. 1998).

located in the medial side of the LP (Fig. 2.2, A and B, Fig. 2.3A). Apart from this retinotopic arrangement, Buchner et al. showed that the LP is also layered into regions for up-, down-, left- and rightward motion (Fig. 2.3B, Buchner et al. 1984). Different LPTCs pool their inputs from different subsets of information from these layers and hence, are tuned to different motion characteristics e.g. speed, direction, size and location of motion stimuli in the visual hemisphere of the fly. Due to the topological arrangement of EMD input many of these properties can simply be estimated by the location and dendritic coverage of the LPTCs in the lobula plate (Hengstenberg, 1982; Hausen, 1984; Borst and Haag, 2002).
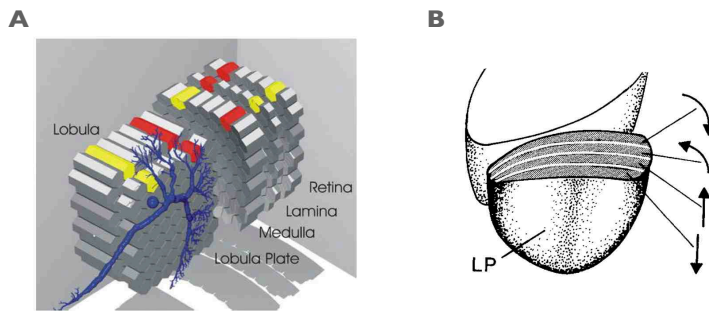
Figure 2.3: Retinotopic input arrangement. (A) Schematic plot showing the conserved relative position of the columnar input from the Retina downstream to the lobula plate (Borst and Haag, 2002). Red and yellow color show cells which respond to stimuli in two distinct locations of the visual field. (B) Schematic drawing of a horizontal cut through the lobula plate (LP) with different input layers. Buchner et al. used deoxiglucose experiments to map the sensitivity for motion direction at the level of the lobula plate. Four different layers from anterior to posterior encode for the four different directions: front-to-back ($\rightarrow$), back-to-front ($\leftarrow$), upward ($\uparrow$) and downward ($\downarrow$) movement (from Buchner et al. 1984).

individually identifiable cells

The most prominent property of the LPTC network compared to other neural systems is the strong degree of constancy in function and morphology throughout individuals (Hengstenberg, 1982; Hausen, 1982, 1984; Borst and Haag, 2002). Cells can be precisely identified in all individuals of one species and therefore studied over a whole population of one species. Each LPTC has unique response properties and occurs only once per hemisphere at the same position in the LP. Fly researchers therefore speak of identified neurons within cell classes and each LPTC has been given a unique name. For these reasons, the LPTC network currently represents one of the best understood neural system in neuroscience (Borst and Haag, 2002; Borst et al., 2010).

horizontal system

Two well investigated sub systems of the LPTC network are subject of this thesis. The horizontal system (HS) in *Calliphora* consists of three cells covering different sections of the LP in the dorsal-ventral direction and are geographically named HSN for north, HSE for equatorial and HSS for south (Fig. 2.2 C, Braitenberg 1970; Hausen 1982). They
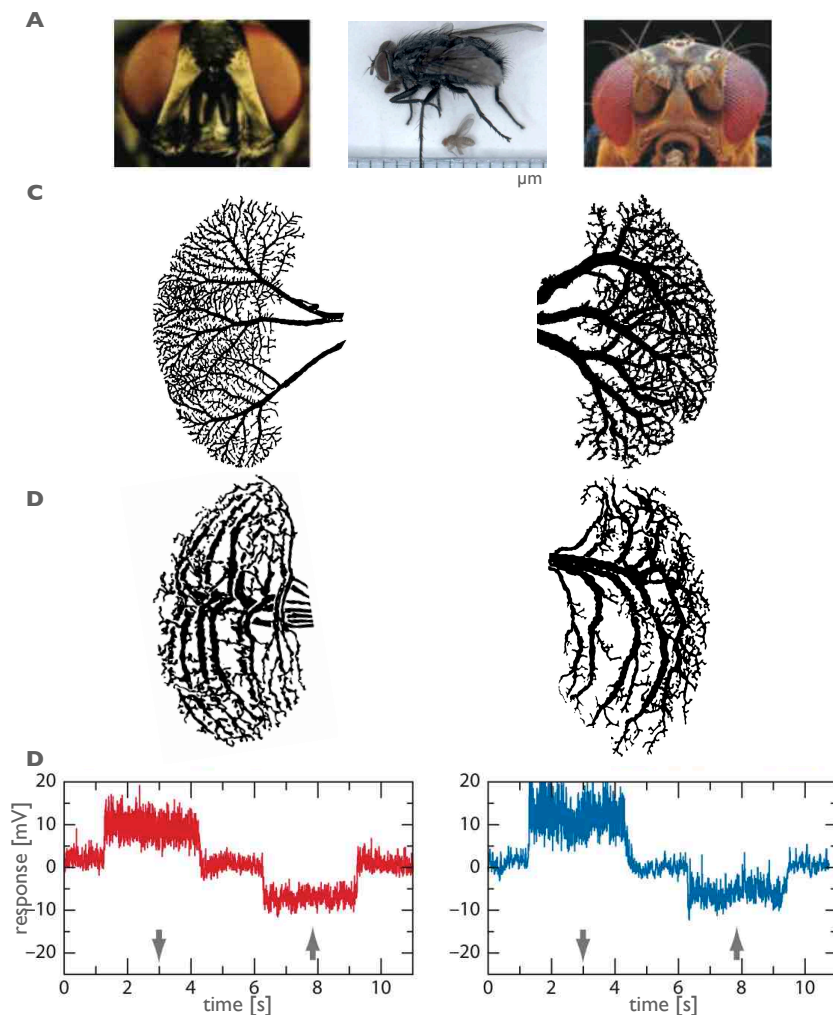
Figure 2.4: LPTCs in different fly species. Comparison of *Calliphora vicina* (left column) and *Drosophila melanogaster* (right column). (A) Overview of fly heads and bodies. Left: *Calliphora vicina*; right: *Drosophila melanogaster*, middle: bodies of blow fly (top) and fruit fly (bottom) (heads: Borst et al. 2010, bodies: Varija Shamprasad Raghu, PhD, unpublished). (B) The horizontal system in both fly species consists of three cells (Fischbach and Heisenberg, 1984). (C) The vertical system has 10 members in *Calliphora* and 6 in *Drosophila* (Rajashekhar and Shamprasad, 2004). The relative location and shape of HS and VS cells is conserved in the two fly species. (D) Example of response properties in VS cells to a vertical bar stimulus presented to a stationary fly (modified from Borst et al. 2010).

respond to large field motion in the horizontal direction by de- or hyperpolarization depending on the direction of motion.

vertical system   The vertical system (VS) in *Calliphora* consists of 10 T-shaped cells that are stacked in the lateral to medial extension of the lobula plate (Fig. 2.2 D and E, Pierantoni 1976). With two thick dendritic branches they span from the ventral to the dorsal side of the LP. They are simply enumerated starting from the lateral site of the LP from VS1 to VS10 and predominantly respond to vertical motion which corresponds to their posterior location in the LP (Hengstenberg, 1982; Haag et al., 1997). Functionally the cells are tuned to different axes of rotations and their sequential interconnectivity allows robust estimation of the fly's current axis of rotation (Cuntz et al., 2007b; Elyada et al., 2009; Weber et al., 2008).

LPTC in Drosophila   HS and VS cells can be easily distinguished functionally and morphologically. They can be found in every individual and even have been identified in different species. *Drosophila melanogaster* deserves special mentioning here (Fig. 2.4, Fischbach and Heisenberg 1984). Although it is harder to access due to its size, *Drosophila* recently gained major interest in neuro-scientific research as combinations of modern imaging techniques and genetic manipulation promise new insights into the wiring of neuronal structures there (Bilen and Bonini, 2005; Muqit and Feany, 2002; Sokolowski, 2001; Borst, 2009). *Drosophila* LPTCs have been shown to resemble *Calliphora* counterparts functionally (Fig. 2.4D, Joesch et al. 2008; Schnell et al. 2010; Borst et al. 2010). The question arises to which extent the significant reduction in overall size (Fig. 2.4A, midddle) has to be compensated and what principles define the common morphological feature space of the two fly species.

With their easy accessibility, their defined input mapping and an exceptional invariability over many individuals the LPTCs represent a great system to study the principles of neuronal shape and its genetic implementation.

2.2 describing, measuring and generating dendritic morphology

neuroanatomy   The variety of different dendritic structures correlates with the functional and behavioral variability of neuronal systems (Fig. 2.5A). However, functional classification of neurons based on anatomical observations alone represent a poor method due to the complexity arising from neuronal branching, intrinsic membrane and cytosolic properties as well as the network a cell is embedded in. Still, for centuries the morphological description and classification of neuronal structures remained the only available research technique and allowed Ramón y Cajal and Camillo Golgi to build the fundaments of

modern neuroscience (Sotelo, 2003; y Cajal, 1995). Today for electrophysiologically inaccessible cells it sometimes constitutes the only hint to their functional contribution. In systems where the sensory input map is preserved it allows for reliable a priori assumptions (Yuste and Tank, 1996; Chklovskii and Koulakov, 2004; London and Häusser, 2005; Miller and A, 1984; Luo and Flanagan, 2007). Additionally, identifying reoccurring morphological patterns can help scientists to further constrain the space of experimental examinations necessary to understand the underlying wiring and function. In order to objectively characterize and compare these patterns, descriptive metrics have been developed (Haug, 1986; Uylings et al., 1986).
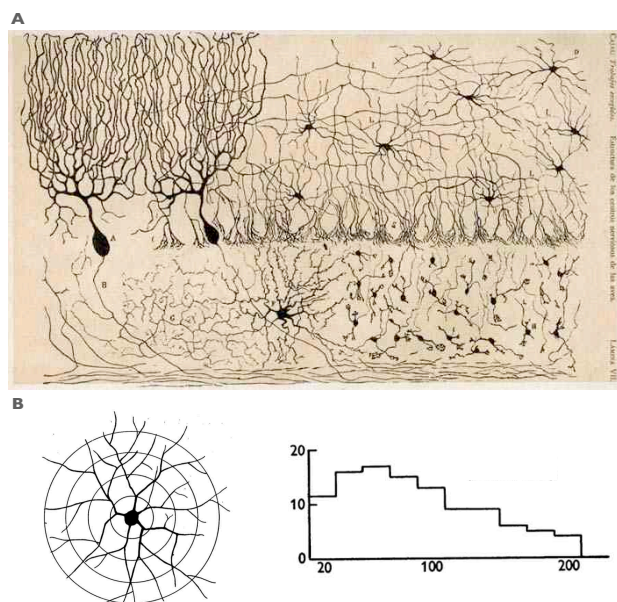
Figure 2.5: Neuronal morphology. (A) Variability of neuronal morphology as captured by Ramón y Cajal. The picture denotes his drawing of cell types in the chick cerebellum with Purkinje, stellate, basket, Golgi and granule cells (Sotelo, 2003; y Cajal, 1995). Research at that time consisted of qualitative classification of neuronal structure. (B) Early quantification technique developed by Sholl. Concentric circles are drawn around the soma of a neuron (here: stellate cell of a cat visual cortex). Intersections with dendrites are counted, plotted and can be compared to other neurons (from Sholl 1953).

The most characteristic feature of neurons compared to other cell types arises from it's complex branching structure. Simple metrics to describe and compare neuronal branching have been around for decades including the popular Sholl analysis (Fig. 2.5B) that can be manually derived directly from cell drawings or digital image recordings (Bok, 1936; Sholl, 1953). Here, concentric circles are drawn around the soma of a neuron. Intersections with dendrites are counted, plotted and can then be com-

metrics and statistics

pared to other neurons. Sholl plots provide a basic assignment of neuronal complexity and allow reliable classification of cell types with significant differences in branching distribution. They combine measures for general topology of a neuron, e.g. branch numbers and levels of branching as well as geometric components like branch length and overall extension. Other statistical measurements separate these two fields. Topological metrics ignore length, scales and dimensions and resemble the sequential order of branch points and terminations points. A neuronal branch point can thereby be seen as node that has two or more connected children nodes, an axonal or dendritic terminal as a node without children. Metrics like depth, complexity and symmetry of a neuron. While two cells with identical branching structure but different scales would have identical topologies, geometrical measures could distinguish these two cells by adding the spatial domain. Parameters like branch angle, direction, length, curviness and diameter largely contribute to the richness of neuronal variability (Hillman, 1979; Uylings et al., 1986; Uylings and van Pelt, 2002). Before computers became a common scientific instrument, these measures had to be manually extracted from images and cell drawings.

reconstructions Comparison of neuronal structures at the level of raw image data is usually restricted to very basic analysis and small sample sizes. Automatic analysis in a massive and detailed manner works best with vectorized, discrete structures. Early vectorized reconstructions resembled neuronal structure as simple node schemes as mentioned before (Hollingworth and Berry, 1975). Here, topological points like branch points and terminals of a neuron were modeled as simple graphs of interconnected nodes, thus only preserving the topographic domain. At the same time computer assisted microscope system came up that allowed coordinate based 3D reconstructions of stained neurons (Macagno et al., 1979). Later, multi-compartmental models were established that also considered the diameters of neurons (Turner et al., 1991). Here, neuronal branching structure is represented by interconnected cylinders with varying diameters (Fig. 2.6 A and B). These cylinder models represent a realistic but reduced, computationally accessible representation of a neuron, also valuable for functional simulations. So called compartmental models can implement Rall's cable theory of current flowing in a passive neuronal fiber or it's active complement defined by Hodgkin and Huxley to model information processing in a biophysically realistic fashion. Each cylinder is thereby seen as a electronic circuit, that connects to other cylinders and is characterized by passive conductance properties and/or active channel dynamics. Thus, faithful cylinder reconstructions can contribute to realistic simulations of neuronal response properties. Many simulation frameworks have implemented support for multi-compartmental models (Eeckman et al., 1994; Hines and Carnevale, 1997; Bower et al., 1998; Gleeson et al., 2007).

While initial reconstructions were performed directly at the experimental setup (Borst

and Haag, 1996; Glaser and Glaser, 1990), modern image acquisition and computational resources allow assisted or even automatic reconstructions from 3D image stacks (Evers et al., 2005; Myatt and Nasuto, 2008; Mann, 2010). Direct comparison of neuronal reconstructions even though discretely represented remains a great challenge due to the immense variety of neuronal structure. Biological randomness, spatial jitter and reconstruction artifacts further increase the hardness of this problem. A reduction to statistical parameters and robust morphological metrics as described for the manual parameterzation have therefore been widely applied (Fig. 2.6C, Ascoli et al. 2001; Scorcioni and Ascoli 2001; Ascoli et al. 2007).
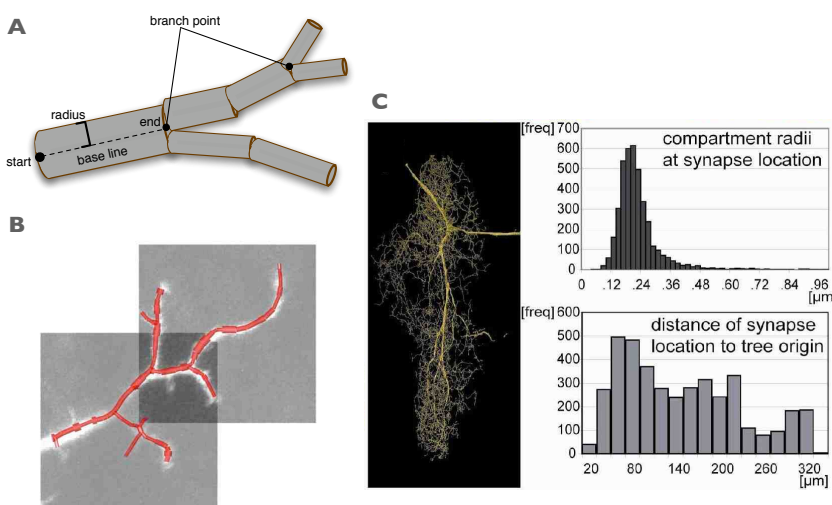
Figure 2.6: Quantitative analysis of neuromorphology. (A) Representation of a neuronal branch using connected cylinders. Each cylinder is defined by a starting point, an ending point and a diameter. (B) Example of a cylinder reconstruction from a 3D image stack. (C) Even complex neurons can be quantified in an automatic fashion when discretized this way. Two exemplifying statistics are shown: the distribution of the radii of the cylinders and the distances of marked synapses to the origin of the dendrite (from Evers et al. 2005).

In electrophysiology the process of reproducing experimental data with a theoretical model allows to condense a complex biophysical system to its functional core. It represents a critical step in understanding underlying functional principles of a neuron (Herz et al., 2006). In anatomical neuroscience such a model could represent a powerful tool e.g. to verify previous morphological classifications, to understand rules of dendritic growth (Ascoli, 2002) or to create network simulations with populations of synthetic neurons (Markram, 2006). Optimally, a model should allow to reproduce neuronal anatomy at the level of eye inspection as well as the parametric space. It should reflect identifying key features of the modeled cell type but also include natural variability.

artificial cells

In recent decades, several such models have been proposed (Ascoli, 1999). They can be distinguished by the principles which constrain their growth. For example, Lindenmayer system (Prezemyslaw and Lindenmayer, 1996) based models assume a general fractal organization of dendrites and are built around iterative growth algorithm based on branching statistics (Ascoli et al., 2001). Resource based models take into account that biological resources are extrinsically limited and construct a competitive environment in which cells grow (Senft, 1997). Global optimization models assume intrinsic optimization rules that a neuron tries to implement and follow while growing (Cuntz et al., 2007a; Budd et al., 2010). None of these systems gained wide acceptance in the neuroscientific community partly due to the complexity of neural branching and differences between individual neuron types. The reduced inter-individual variability in fly neurons might allow to reliably constrain and validate one such model. Additionally, *Drosophila*'s genetic toolbox provides insight into the biological growth program.

2.3 the criticial role of Dscam in shaping neuronal morphology

molecules and morphology

Our current view on neuronal growth reflects a quite complicated process with many molecular players involved (Corty et al., 2009; Georges et al., 2008; Dickson, 2002). Cell intrinsic and extracellular signals are integrated and tightly controlled by a wide range of different molecules. Changes in concentration, location and timing of their expression can lead to very different morphological structures. With a descriptive view in mind, different molecular components can be attributed to different morphological characteristics of a neuron. Alterations of the Golgi outpost or manipulations of the growth cone for example have direct influence on the development of dendritic branching. Genetically changing guidance behavior or dendro-dendritic interaction on the other hand alters the area a neuron is able to span into (Corty et al., 2009). Using *Drosophila*'s rich genetic toolbox we are now able to precisely map the molecular mechanisms to their role in neuronal formation.

surface proteins

Essential wiring behavior of neurons like self-avoidance, tiling, synaptogenesis and fasciculation all require the identification of neuronal branches within the extracellular space (Fig. 2.7, Hattori et al. 2008). Extracellular interactions are commonly mediated through transmembrane proteins (Fig. 2.8A). Target specific docking of the extracellular domain leads to changes in conformation and subsequently the intracellular domain to initiate signaling cascades that can alter cell growth processes (Corty et al., 2009).

Dscam1

This work focuses on the Down Syndrome Cell Adhesion Molecule (Dscam) a trans-
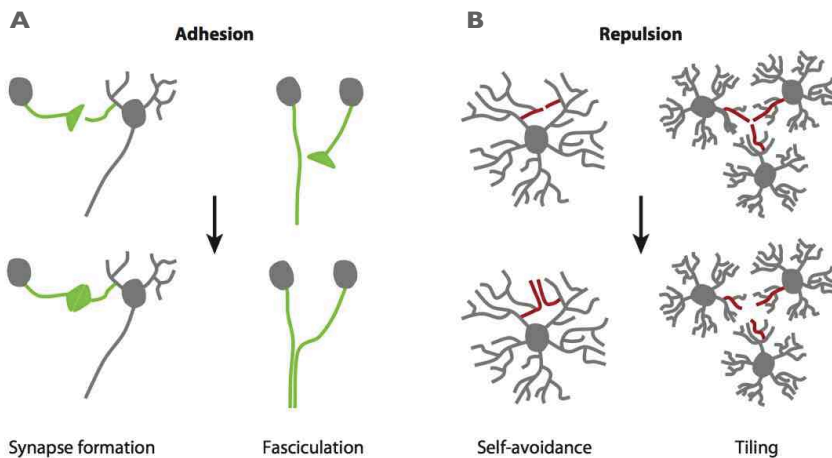
Figure 2.7: Neuronal interactions. Neuronal wiring highly depends on interactions of neurites. Four important reactions are shown. (A) Expression of adhesive molecules (green) synapse formation can lead to direct connections of neurons or bundling of axons (fasciculation). (B) Repulsive molecules (red) lead to self-avoidance and tiling of neurites and allow to efficiently cover a certain input area (from Hattori et al. 2008).

membrane protein (Chen et al., 2006; Schmucker et al., 2000; Hughes et al., 2007; Hummel et al., 2003; Zhu et al., 2006; Wang et al., 2004; Zhan et al., 2004) that has been shown to be disrupted in down syndrome patients. So far four genetic *Dscam* loci have been identified on different chromosomes in *Drosophila*, with the Dscam1 as the most intensively investigated. Through alternative splicing, the *Dscam1* gene has the potential to encode for a number of 38,016 Dscam protein variants that share common transmembrane domains but vary in their distinct ways of interfacing intra- and extracellular domains (Fig. 2.8B). In general the binding behavior can be modeled as a repulsion of same variants (Fig. 2.8C and D). Cells usually express several Dscam1 variants and evidence exists that they encode their identity through their distinct Dscam1 profile (Hattori et al., 2008). *Dscam1* research is still very young and many aspects remain to be unraveled: The process of the Dscam1 profile establishment as well as the intracellular signaling cascade have not been revealed yet. No functional nor behavioral implications of manipulated Dscam1 profiles have been studied. The lack of quantitative analyses only allowed vague statements about the influence on the neuronal morphology and wiring. It is also unclear whether all neurons express Dscam1. In this respect, the LPTC system being easily accessible and with its strong stereotypic morphology and topographic mapping represents a great opportunity to further investigate the influence of the Dscam1 protein at the level of morphology, function and behavior.

Global *Dscam*1 knock-out in *Drosophila* has been shown to be lethal (Schmucker et al.,   *Gal4-UAS*
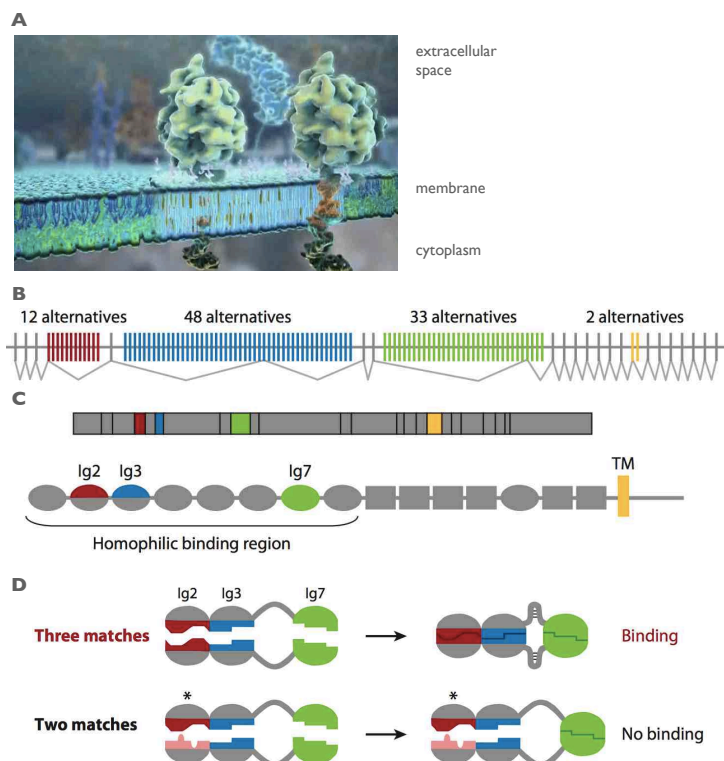
Figure 2.8: Dscam transmembrane protein family. (A) Digital reconstruction of a transmembrane protein with it's three domains (from the 'Inner life of a cell' movie, http://multimedia.mcb. harvard.edu/). (B) The *Drosophila Dscam1* gene encodes a large family of transmembrane proteins. *Dscam1* contains four blocks of alternative exons that encode 12 different variants for the N-terminal half of Ig2 (red), 48 different variants for the N-terminal half of Ig3 (blue), 33 different variants for Ig7 (green), and two different variants for the transmembrane domain (TM) (yellow). Splicing leads to the incorporation of one alternative exon from each block (C). (D) Dscam1 proteins exhibit isoform-specific homophilic binding between identical isoforms that match at all three variable Ig domains. Isoform pairs that contain only two matches and differ at the third variable domain do not bind to one another (from Corty et al. 2009).
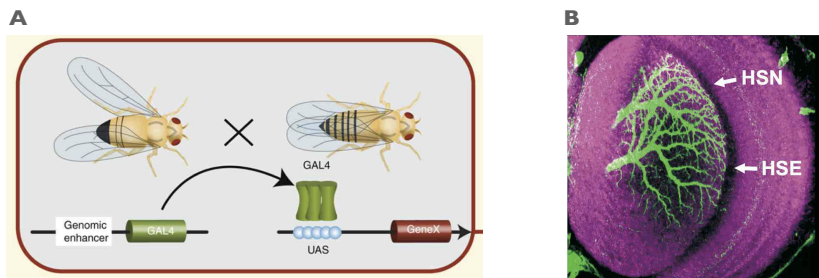
Figure 2.9: Cell specific targeting using the the Gal4-UAS system. (A) A driver line with a cell specific Gal4 gene is crossed with an effector line containing a gene with a Gal4 binding UAS site (Upstream Activating Sequence). Offspring containing both constructs show cell specific expression of the UAS controlled gene (from Borst 2009). (B) Example of a transgenetic fly line (NP 0282, Otsuna and Ito 2006) that labels two LPTCs (from Schnell et al. 2010).

2000). In order to study *Dscam1*'s effects in detail one has to limit experiments to smaller populations of cells. Cell specific transgenic expression systems like the Gal4-UAS system allow cell specific targeting in *Drosophila* (Brand and Perrimon, 1993; Borst, 2009). The system consists of two different genetic script injections: a yeast originated Gal4 transcription factor gene controlled by a cell specific enhancer is responsible for the specific location of expression; a UAS (Upstream Activating Sequence) initiated gene encodes for a certain effect e.g. Overexpression of a Dscam variant and is controlled by Gal4 (Fig. 2.9). The cell specificity of driver lines and the timing of expression relative to the development are commonly characterized through large-scale, random screenings. As both genetic scripts originate from the yeast, interactions with other genes remain negligible. Gal4 driver and UAS effector are usually prepared in different fly lines to combine different targets and effects. Additionally a reporter protein like GFP can be added to visualize a cell's morphology and to confirm the success of the targeted expression. Recently several fly lines have been described that consistently show cell specific expression in subgroups of different Lobula Plate Tangential Cells (Schnell et al., 2010; Joesch et al., 2008). Combinations of these driver lines with Dscam1-UAS constructs enable additions and overexpressions of Dscam1 variants and subsequently change the contact characteristics of the targeted LPTCs.

2.4 project outline

This thesis is composed of four interconnected research projects:

1. **morphological characterization of LPTCs in blow flies**
   LPTCs can be easily identified according to their morphology in every individual
   fly. However, little is known about the underlying principles of this constancy.
   Supported by a large database of *in vivo* cell reconstructions and a computational
   quantification framework, I investigate the anatomy of four LPTCs in blow flies.
   The morphological identity of the four cell types is characterized by a statistical
   analysis over morphological parameters and modeled using a synthetic growth
   algorithm.

   Results of this project have been published in Cuntz et al. 2007b, 2008, 2010.

2. **morphological analysis of down-scaled LPTCs in fruit flies**
   The observation of similar form and functionality but a large difference in size
   of LPTCs in blow flies and fruit flies raises the question to which extent mor-
   phological principles are maintained. I explore this issue with a qualitative and
   quantitative analysis of HS cells in transgenic *Drosophila* flies. *Drosophila* cell
   reconstructions and the established quantification framework facilitate detailed
   comparison of the HS system in *Calliphora* and *Drosophila*.

   Results of the qualitative analysis of *Drosophila* HS cells have been contributed
   to Schnell et al. 2010.

3. **functional implications of LPTC scaling in blow and fruit flies**
   In this part of my thesis I take a closer look at the impact of HS cell scaling onto
   their functional properties. Passive signal propagation is largely affected by the
   length and membrane surface of a neuron and the difference in cell size therefore
   implies different properties of signal propagation. Simulations of current injec-
   tions into computational models of *Drosophila* HS cells quantify this functional
   impact of size and branching architecture.

   Results of project 2 and 3 are subject to a manuscript in preparation:
   Forstner et al. 2011.

4. **impact of Dscams onto LPTC morphology and function**
   The transmembrane protein family Dscam has been shown to mediate the pro-
   cess of adhesion and repulsion of neurites and consequently, has been attributed
   to essential wiring behaviors of neurons such as tiling, self-avoidance and synapse
   formation. With their topographic input arrangement, their two dimensional ex-
   tension and electrophysiological accessibility, LPTCs represent a great system to
   study Dscam in detail. In this project I describe the morphological consequences

of Dscam overexpression on LPTCs and compare the impact of this manipulation onto the morphological and electrophysiological properties.

Results are part of a manuscript in preparation: Shi et al. 2011.

3 materials and methods

3.1 cell imaging and reconstruction in blow flies

data workflow

In order to study neuronal anatomy in detail, adequate high resolution techniques were required to resolve even small dendritic structures. A large number of cells was necessary for our quantitative approach. Traditionally biological imaging produces 2D pixel and 3D voxel data that is inaccessible to many computational algorithms due to data size and complexity. Therefore, image data had to be transformed into simple binary trees of connected cylinders that encoded well the core features of the cell morphology while being computationally tractable.

animal preparation

The preparation and cell identification procedure was performed by our technical assistant Renate Gleich and Jürgen Haag. Female blowflies (*Calliphora vicina*) were briefly anesthetized with CO_2 and waxed on a small preparation platform. The head capsule was opened from behind; the trachea and air sacs that cover the lobula plate were removed. To eliminate movements of the brain caused by peristaltic contractions of the esophagus, the proboscis of the animal was cut away and the gut was pulled out. The fly was then mounted on a heavy recording table looking down onto two stimulus monitors.

cell identification

Cells were initially identified according to their location in the lobula plate and their stimulus response properties. Cells of interest were then filled with a fluorescent Alexa dye (Alexa 488) and morphologically identified under a fluorescence microscope (Fig. 2.1 B). Preparations in which the cells were properly filled were transferred to the 2-photon-microscope.

2PM setup

A custom-built two-photon microscope (Haag and Borst, 2004; Denk et al., 1990) consisting of the following components was used: a 5 W pumped titanium:sapphire laser (MaiTai; Spectra Physics, San Jose, CA), a Pockels cell (Conoptics, Danbury, CT), scan mirrors including drivers (Cambridge Technology, Lexington, MA), a scan lens (4401 302; Rodenstock, Columbus, OH), a tube lens (MXA 22018; Nikon, Tokyo, Japan), a dichroic mirror (DCSPR 25.5 x 36; AHF, Tübingen, Germany), and a 40x water immersion lens (Zeiss). The lens can move along all three axes by a step-motor-driven micromanipulator (MP285 3Z; Sutter Instruments, Novato, CA). Emitted light is filtered in parallel by two bandpass filters (HQ 535/50M and HQ 610/75M; Chroma Technology, Brattleboro, VT) and collected by multi-alkali photomultipliers (R6357; Hamamatsu, Bridgewater, NJ). The whole system is controlled by custom-written software (CfNT version 1.569; Michael Müller, Max Plank Institute for Medical Research, Heidelberg, Germany).

image recording

Flies were rotated until the cells were placed orthogonally with respect to the laser beam to minimize the amount of images in the Z-direction. In order to capture the entire extent of the cells, 6 to 15 adjacent stacks (210 μm x 210 μm area in XY x 30

in 2 mu m Z-steps) were taken from different XYZ positions with an overlap of about 10 percent (Fig. 3.1A).

Image stacks were then transferred to Matlab (Mathworks, Natick, MA, http://www. mathworks.com) and all further analysis was performed there in custom written software. Manual fine tuning of the original coordinates from the individual stacks was usually necessary to obtain a precise alignment in three dimensions. Reconstruction was done directly on the raw images. Only the color mapping was changed to increase contrast if necessary. Projections of maximum intensity and corresponding depth were computed along the Z-axis. This reduction from 3D-data to two 2D images was sensible as there were no or very few 3D crossings of branches and all cells were planar. Based on these images, cylinder models of the branching structure were obtained in a semiautomated way: the interactive software allowed switched viewing of either Z-projection or an individual slice of an image stack Fig. 3.1B. The widths of 2D rectangles connecting the end points were fitted by gauss functions to suggest a diameter for the cylinders (Fig. 3.1C). Z-values were attributed to each cylinder directly from the depth-map according to their 2D location. Quick tracing results (30 min) were achievable working with maximum Z-projections alone, although slight movements of the living fly compromised the accuracy of the projection image (Fig. 3.1B). In order to achieve a higher accuracy, some manual corrections based on individual slices were necessary in all reconstruction steps. Taking advantage of the planar cell morphology allowed quicker reconstructions compared to other approaches (Schmitt et al., 2004): detailed cell models with about 600 to 2000 compartments were obtained typically within around 2 hours. Jumps in the Z-axis were smoothed by use of linear interpolation. Reconstructions were stored as SWC files where each cylinder is defined by a unique cylinder ID starting with 1 and progressively incrementing for each cylinder, an area code (soma=1, axon=2, dendrite=3), XYZ components of the cylinder end point, a diameter and the cylinder ID of its origin also referred as parent ID (Cannon et al., 1998). In a SWC file all these values are written in one line of text representing one cylinder. The first cylinder does not have a origin cylinder and therefor receives the parent ID -1. SWC files represent a non-redundant data structure that can be transformed to geometrical cylinder structures by taking each entry's coordinates as end point and it's corresponding parent ID's coordinates as start point of a cylinder with the radius given by the end point entry.

cylinder reconstructions

3.2 genetics, cell imaging and reconstruction in Drosophila

Drosophila genetics, preperation and imaging were performed by Jing Shi and Sham-

fly preparation
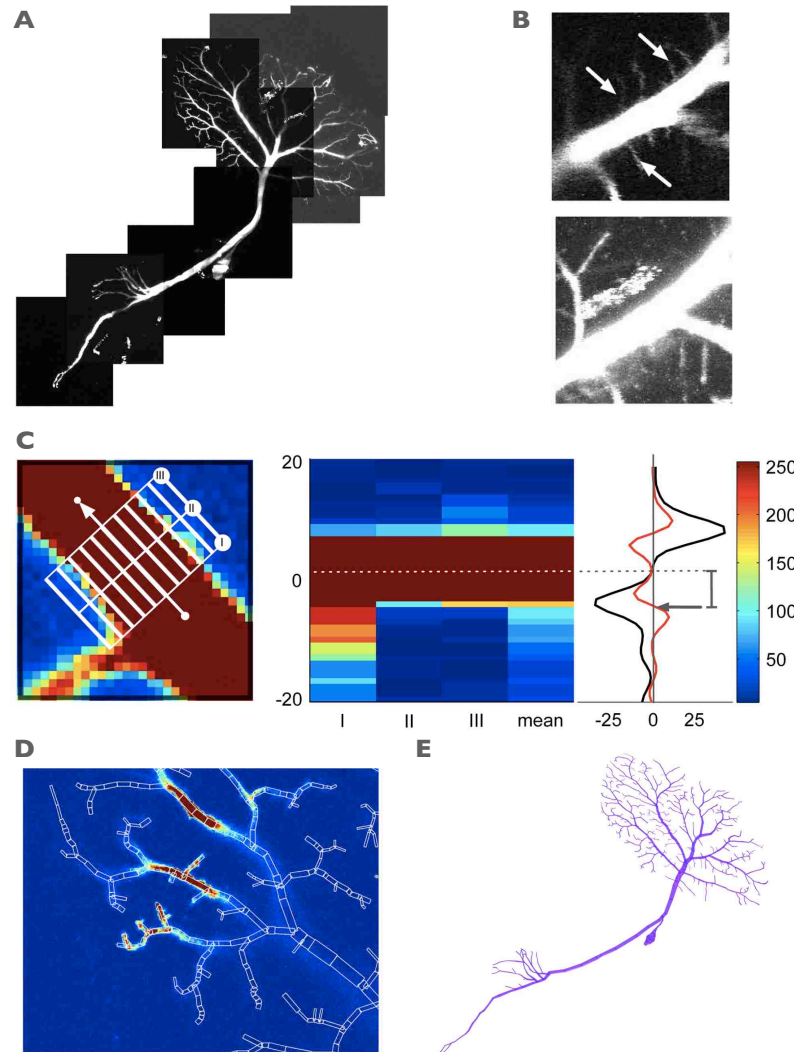
Figure 3.1: Cell imaging and reconstruction process. (A) Assembled maximum Z-projection of an HSN from ten overlapping image stacks. (B) Comparison between a single slice (upper panel) and a maximum Z-projection (bottom panel) of a small example stack. Slight movements and blurring leads to a loss of visible dendrites (white arrow). (C) Example of an automatic diameter approximation. Normalized positions 0.25, 0.5 and 0.75 on the midline and 40 half pixels in the orthogonal direction were used to construct a sampling grid that covered the full extent of the branch thickness (first and second panels). The average over the resulting sampling matrix was convolved with the first derivative of a Gaussian distribution to emphasize brightness changes (black line). The diameter was obtained by the distance from the centre of the maximum plateau in the mean signal to the null in the derivative of the convolved signal (red line). (D) Example of a reconstructed sub-tree of an HSN cell superimposed on a single slice from one image stack. (E) Complete cylinder reconstruction of (A), rendered in the Blender animation system (Blender Website, http://www.blender.org).

prasad Varija Raghu, PhD. Four fly lines were used Table 3.1. The brains of female flies were excised, fixed in 4 % Paraformaldehyde for 30 minutes and washed for 45-60 minutes in phosphate-buffered saline (PBS) including 1 % Triton X-100 (PBT). The brains were further incubated for one hour in PBT with 2 % normal goat serum (Sigma Aldrich, St. Louis, MO). The primary antibody Alexa Fluor 488 rabbit anti-GFP-IgG (A-21311, Molecular Probes, Eugene, OR) was added (1:200) overnight at 4° C and removed by a series of washing steps in PBT. Subsequent to a final washing step in PBS for 45-60 minutes, the stained brains were mounted in Vectashield (Vector Laboratories, Burlingame, CA) and analyzed by confocal microscopy.

genotype	application
+/+ UAS-mCD8-GFP/+ Gal4-NP0282/UAS-GFP	wildtype analysis
DB331-Gal4/+ UAS-mCD8-GFP/CyO Dscam11.31.25.1/+	Dscam 11.31.25.1 overexpression experiments
DB331/+; mCD8-GFP/CyO +/+	control for Dscam overexpression experiments

Table 3.1: Fly lines. Crossings were performed by Jing Shi and Shamprasad Varija Raghu, PhD.

Serial optical sections were taken at ∼0.33 μm intervals with 1024 x 1024 pixel resolution using a confocal microscope (LEICA TCSNT) and oil-immersion 63X or 40X plan apochromat objectives. In all cases, frontal (coronal) sections were taken from the posterior side of the brain. Cells and lobula plate were captured with single stacks. *image recording*

The NP0282 driver line labeled HSN and HSE cells in both optic lobes (Otsuna and Ito, 2006; Schnell et al., 2010). The reconstruction procedure required slight adjustments for the use with *Drosophila*. Cells showed a much higher branching complexity and GFP co-labeling of HSE and HSN led to a more time consuming slice by slice reconstruction (5-6 hours/cell). Due to the high number of co-labeled structures outside of the lobula plate, axons could not be reconstructed. For complete reconstructions a few cells were additionally filled with fluorescent dyes. *reconstruction in NP0282*

In the DB331 line all VS and HS cells were labeled and small dendrites could not be reliably attributed to one particular cell (Joesch et al., 2008). Here analysis was limited to the area covered by the dendrite. Thicker, easily attributable branches were followed from the root to the dendritic tips until the dendritic coverage was faithfully sampled (see Fig. 4.30 in the results chapter for details). Background stains allowed reconstruction of the lobula plate volume. The border of the the LP was traced in *reconstruction in DB331*

each slice using the ImageJ polygon tool. Polygons were stored in ROI files and later transferred to Matlab using a roiread function (see software listing in section 3.6).

3.3 morphological analysis

post-processing

For simplification, the reconstructed directed graphs were transformed into strict binary trees by substituting multifurcations with several bifurcations after minimally shifting the branches on their parent cylinder. Region indices (soma (1), axon (2) or dendrite (3)) were manually attributed and written to a SWC file (see cylinder reconstructions, above). The somata in all cells consisted of a clearly separated bag-like structure that branched from the axon or dendrite. The last branch point (very short branches were ignored) before the soma was chosen to be the end of the dendrite and the beginning of the axon. The dendrite root was set to the primary branching point. All LPTC reconstructions were rotated for both the dendrite root and the furthest axon terminal tip to lie on the horizontal line building the axonal axis later used to normalize the orientation of the cells. Dendrite flattening was performed as a morphometric transform (Zador et al., 1995) to shift all further analysis from 3D to 2D space (3.2B).

spanning field calculation

A distance isoline to any point on the dendrite was drawn at a 25 μm (7 μm in *Drosophila*) threshold to determine the dendrite spanning fields (3.2B). This corresponds to performing a morphological dilation on the same points with a radial disc with 25 μm radius. A second estimation of the dendritic coverage was given by the additionally computed convex hull. The resulting area representations were parameterized in several ways (see results chapter 4).
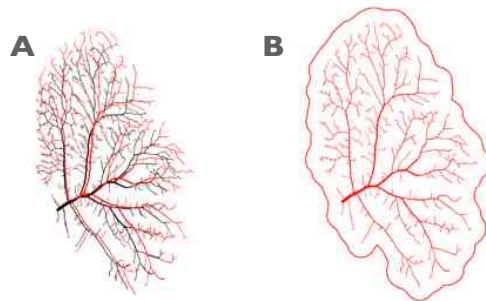
Figure 3.2: Spanning field calculation and vector operations. (A) Flattening of dendrites, 3D in black, flattened 2D in red, (B) Dendrite spanning field, a distance isoline to any point on the dendrite was drawn at a 25 μm (prepared by Hermann Cuntz).

branching statistics

As mentioned before the neuronal branching structure of LPTCs was captured using interconnected cylinders. For the extraction of branching metrics this structure was

interpreted as a graph structure built of nodes, where each cylinder was represented by one node (Fig. 3.3A). Each node was attributed with spatial SWC information like the XYZ coordinates and the diameter, representing the morphological component. The topological properties of the nodes were defined by the connections with other nodes. In the SWC file connections are described by the ID and the parent ID of each entry. This tuple can also be seen as a sparse representation of an adjacency matrix (Cuntz et al., 2010). An adjacency matrix displays the connections for all nodes in a two dimensional matrix by assigning a '1' to connecting nodes and a '0' to unconnected nodes (Fig. 3.3B). The adjacency matrix was primarily used as supporting structure for various parameter calculations. The separation of topology and morphology allowed to quickly extract various branching metrics as will be seen in the results section.

A   **B**   **C**

node parent ID

node ID	1	2	3	4	5	6	7	8	9	9	10	11	12	14
1	0	0	0	0	0	0	0	0	0	0	0	0	0	0
2	1	0	0	0	0	0	0	0	0	0	0	0	0	0
3	0	1	0	0	0	0	0	0	0	0	0	0	0	0
4	0	0	1	0	0	0	0	0	0	0	0	0	0	0
5	0	0	0	1	0	0	0	0	0	0	0	0	0	0
6	0	0	0	0	1	0	0	0	0	0	0	0	0	0
7	0	0	0	0	0	1	0	0	0	0	0	0	0	0
8	0	0	0	0	0	0	1	0	0	0	0	0	0	0
9	0	0	0	0	0	0	0	1	0	0	0	0	0	0
10	0	0	0	0	0	0	0	0	1	0	0	0	0	0
11	0	0	0	0	0	1	0	0	0	0	0	0	0	0
12	0	0	0	0	0	0	0	0	0	0	1	0	0	0
13	0	0	0	0	0	0	0	0	0	0	0	1	0	0
14	0	0	0	0	0	0	0	0	0	0	0	0	1	0

• root

• continuation point
• branch/termination point
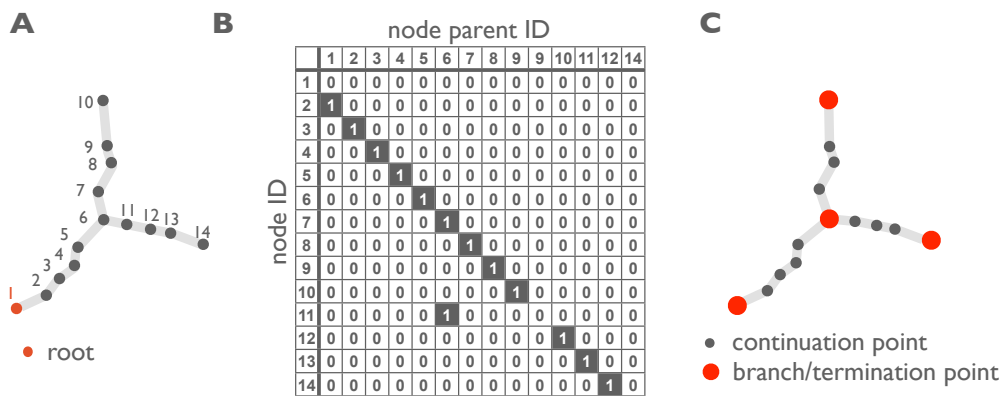
Figure 3.3: Reconstructions as graphs (A) Example of a dendrite as directed graph. Each dot resembles one node. Edges are connecting the nodes. Nodes correspond to ending points of the cylinders in the cylinder reconstruction. Edges correspond to the cylinders. (B) The topology of the directed graph can be expressed as an adjacency matrix. Here, connections are denoted as ones, everywhere else the matrix is zero. (C) Topological points were defined as termination and branch points. Continuation points lie in between topological points and can be shifted and split on the given path without morphological alterations of the overall structure. In the adjacency matrix branch points can be identified by columns with two 1s, continuation points by columns with one 1 and termination points by rows with no 1s.

In this thesis nodes and points will be used interchangeably. Branch points are defined as nodes with two connecting nodes, termination points as nodes with no connecting nodes. Nodes of the graph that are inclosed by branch and/or termination points are defined as continuation points (Fig. 3.3C). While the location of branch and termination points are fixed within the neuronal reconstructions, continuation nodes can be split quite arbitrarily and even joined without morphological alterations when diameter and direction are consistent. To emphasize this difference, branch points and termination points were defined as topological points.

Visualization was done using cylinders and frusti. A frustum is a cone with a pruned top, it can therefore implement smoother tapering between two diameters. Figure 3.4 denotes the applied polygon sampling of a cylinder from coordinate and diameter data.

software frameworks

All analyses were performed using a customized version of the TREES toolbox, a Matlab toolbox for quantifying, exploring and creating neuronal morphology (Cuntz et al., 2010) and TREES website, http://www.treestoolbox.org). The TREES toolbox was established and maintained by Dr. Hermann Cuntz. All results were confirmed with an independent Matlab framework developed by the author (Forstner, 2005), that eventually merged with the TREES toolbox published during the thesis (Cuntz et al., 2010).
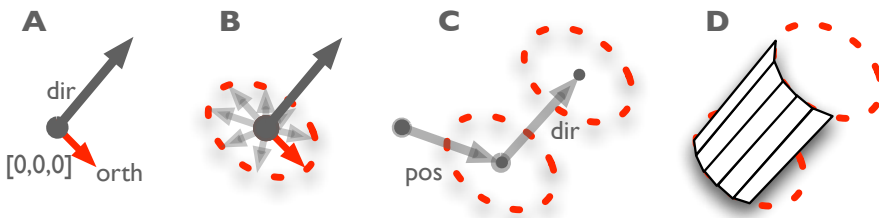
Figure 3.4: Efficient cylinder visualization (A-D) Polygon sampling of a cylinder. (A) Each cylinder's 3D orientation can be described by direction vector (dir). An orthonormal vector (orth) to the direction vector was used to sample the circular base with vertices (B). One copy of this base was shifted to the beginning of the cylinder by adding the position vector (pos), another copy was shifted to the end by adding both pos and dir (C). The shifted vertices were then connected to polygons (D). This procedure was repeated for each cylinder.

3.4 generating artificial cells

minimum spanning trees

Artificial *Calliphora* neurons were created by Dr. Hermann Cuntz using a minimum spanning tree algorithm (Cuntz et al., 2007a). *Drosophila* neurons were created by customizing his scripts and the Matlab TREES toolbox. A minimum spanning tree (mst) represents a graph theoretical structure that - given a set of control points in 2D or 3D - connects points with a minimum amount of wiring. To grow realistically appearing trees the wiring cost criterion was extended by a cost for path distance of any point to the dendritic root. This can be seen as a measure for what is called "synaptic democracy" when considering the conduction time of synapses distributed along the dendrite. A balancing factor bf weighted the influence of the path distance. The mst algorithm starts at a defined starting point and adds points iteratively in a point-by-point fashion. In each step a distance matrix from all already connected
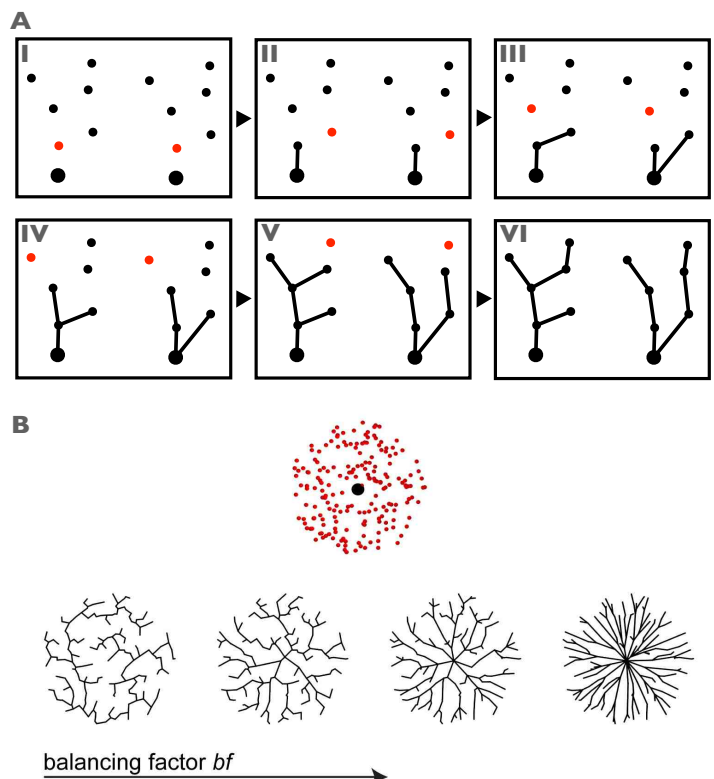
Figure 3.5: Minimum spanning algorithm. (A) Sketches of the minimum spanning tree algorithm with two different balancing factors (lower bf left and higher bf). Each box represents one step in the iterative growth. Dots are target points, red dots are minimizing the applied cost function are consecutively connected next. In step III the two trees/dendrites start to grow differently. The left tree connects points by saving material while the right tree tends to reduce the path distance to the root. (B) Distributing random points on a disk shaped surface (red dots) and growing dendrites onto these points with different bf values. The root was located in the centre of the circular surround in all cases.
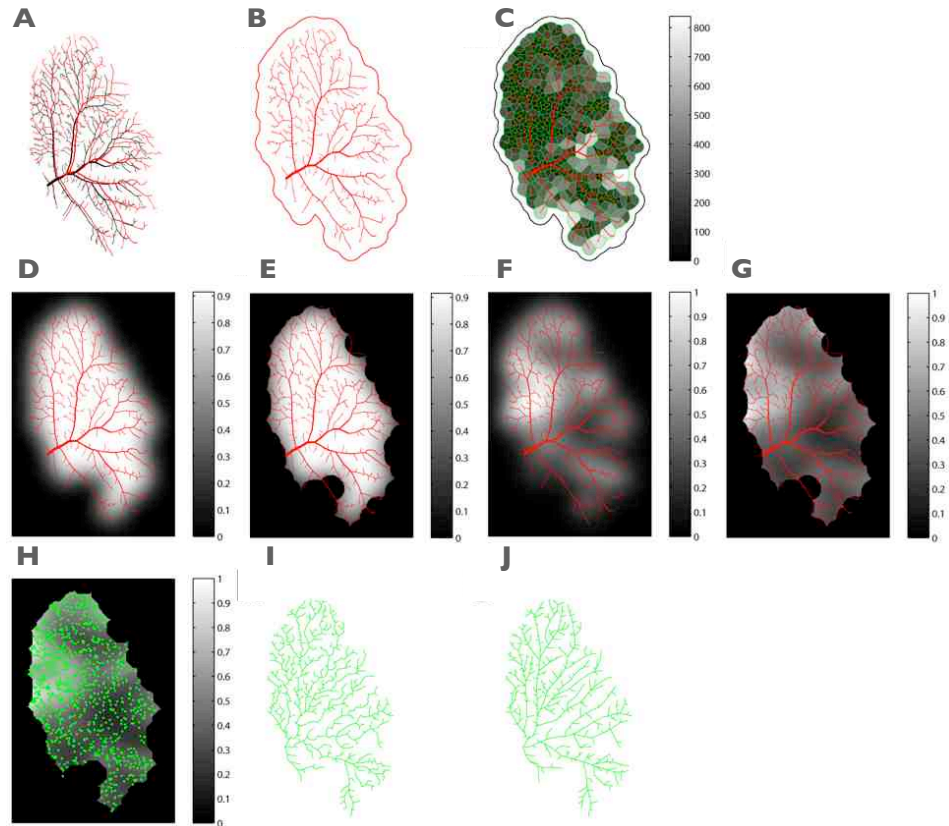
Figure 3.6: Synthesizing LPTCs. (A) Planar dendrites were mapped entirely to two dimensional space (black original, red flattened dendrite). (B) The dendrite spanning fields were determined by drawing a region at 25 μm away from any point on the dendrites. (C) Topological point density distribution was obtained by Voronoi segmentation (green borders) with a dendrite spanning field boundary. Shaded gray scale indicates surface area of Voronoi pieces. Overlaid dendrite in red. (D) dendrite topological points were morphologically closed (dilation followed by erosion) with a 25 μm radius disc and the resulting binary image smoothed with a Gaussian filter of 25 μm variance; (E) This was then cut out by the boundaries of the closed image, representing for each location in the dendrite spanning field the error made when smoothly averaging the density; (F) density estimation of topological points by Gaussian filtering with a 25 μm variance. (G) the density map in (F) was normalized by the estimation error obtained in (E); (H) random points (green) were distributed according to the corrected density distribution with sharp boundaries; (I) preliminary artificial dendrite following the iterative greedy algorithm presented previously (Cuntz et al., 2007a) on green points in (H); (J) Artificial dendrite after smoothing along heavier branches; (K) quadratic diameter decay was mapped on the resulting dendritic structure according to an optimization of electrotonic synaptic democracy (Cuntz et al., 2007a). The resulting artificial dendrite shows similarity with the original tree in (A), (prepared by Hermann Cuntz).

points P_i to all free points (P_j) was calculated and weighted by bf times the path distance to the dendritic root P_0:

$$D_{i,j} = ||P_i P_j|| + bf ||P_0 \rightarrow P_j|| \tag{3.1}$$

The point connection with the lowest cost was then established and the algorithm continued with the next iteration. Figure 3.5A depicts two trees grown with a low and a high bf. Lower bf values result in trees with less wiring, while higher bf values lead to more direct connections to the root. A realistic example of a cell grown into a disc shaped structure is shown in Figure 3.5B.

The complete workflow of synthesis is shown in Figure 3.6. Cells were grown into the flattened spanning fields of the original *in vivo* reconstructions (Fig. 3.6A and B). The root of the *in vivo* dendrite was set as starting point for the mst algorithm. Points were randomly distributed in the spanning fields but the point densities were localized by following the relative point densities of the individual *in vivo* reconstruction (Fig. 3.6C-H). Only the topological points (branching, termination) were considered for the calculation of the point density. This pseudo-random distribution of carrier points was introduced to take into account the inhomogeneous distribution of the *in vivo* carrier points while creating a truly new cell. The total number of random points was increased until the resulting number of topological points in the artificial dendrites matched the original dendrites. In a post processing step, XY-coordinates of points on longer branches were smoothed by spline interpolation to result in more realistic dendrites (Fig. 3.6I and J).

mst workflow

3.5 passive compartmental models

Simulations were fitted to electrophysiological *in vivo* recordings in *Drosophila* which were performed by Bettina Schnell.

fly preparation

Flies were anesthetized on ice and waxed on a Plexiglas holder. The head was bent down to expose the caudal backside of the head and the extended proboscis was fixed. Aluminum foil with a hole of about 1-2 mm sustained by a ring-shaped metal holder was placed on top of the fly and separated the upper wet part (covered with Ringer solution; Wilson et al. 2004) of the preparation from the lower dry part. Water-immersion optics was used from above; visual patterns were presented to dry and fully intact compound eyes. A small window was cut into the backside of the head, and during mild protease treatment (protease XIV, E.C.3.4.24.31, P-5147; Sigma Aldrich; 2 mg/ml, max 4 min), the neurolemma was partially digested and the main tracheal branches and fat body were removed. The protease was rinsed off carefully and replaced by Ringer solution.

A saline jet was generated with a Ringer-filled electrode to remove the extracellular matrix and to expose the HS cell somata for recording.

recordings   Genetically labeled green fluorescent HS cell somata were approached with a patch electrode filled with a red fluorescent dye (intracellular solution, Wilson and Laurent 2005) containing an additional 5 mM Spermine (S-2876, Sigma-Aldrich) and 30 mM Alexa Fluor 568 hydrazide-Na (A-10441, Molecular Probes) adjusted to pH 7.3). Recordings were established under visual control with a x40 water-immersion objective (LumplanF, Olympus), a Zeiss microscope (Axiotech Vario 100, Zeiss, Oberkochen, Germany), fluorescence excitation (100-W fluorescence lamp, heat filter, neutral-density filter OD 0.3; all from Zeiss), and a dual-band filter set (EGFP/DsRed, Chroma Technology, Bellows FallsVT). During the recordings, the fluorescence excitation was shut off to prevent blinding of the fly. Patch electrodes of 6- to 8-$M\Omega$ resistance (thin wall, filament, 1.5 mm; WPI, Sarasota, FL) were pulled on a Sutter- P97 (Sutter Instrument, Novato, CA). A reference electrode (Ag-AgCl) was immersed in the extracellular saline (pH 7.3, 1.5 mM CaCl2, no sucrose). Signals were recorded on a BA-1S Bridge Amplifier (npi electronics, Tamm, Germany), low-pass filtered at 3 kHz, and digitized at 10 kHz via a D/A converter (PCI-DAS6025, Measurement Computing, Norton, MA) with Matlab.

compartmental simulation   A passive compartmental model simulation was implemented using Matlab and the TREES toolbox. The electrotonic representation of the neuronal branching was defined by the specific axial resistance R_a in Ωcm, the specific resistance of the membrane R_m in Ωcm^2 and the specific membrane capacitance C_m in $\frac{\mu F}{cm^2}$. While the specific passive parameters were assumed to be homogeneously distributed, the varying cylinder radius (r) was considered when calculating axial resistance/conductance

$$r_a = \frac{R_a}{\pi r^2} = 1/g_a \tag{3.2}$$

membrane resistance/conductance

$$r_m = \frac{R_m}{2\pi r} = 1/g_m \tag{3.3}$$

and membrane capacitance

$$c_m = C_m 2\pi r \tag{3.4}$$

as length dependent parameters from their specific variants R_a, R_m and C_m (Fig. 3.7).

A passive compartmental model equation system was setup using Matlab and the TREES toolbox. First, the conductance matrix was established. For a three compart-
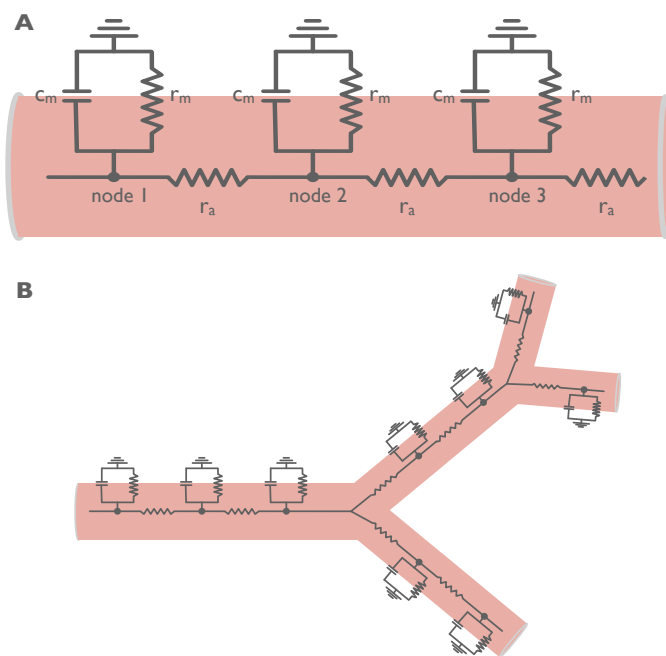
Figure 3.7: Electrotonic representation of neuronal structure. (A) Three linearly connected nodes (compartments) exemplifying the principles of the electrical cable representation of a neuron. The red tube depicts the intracellular space, white the extracellular domain. r_a - axial resistivity, r_m - membrane resistance, c_m - membrane conductance. (B) Electrotonic representation of a small branching structure with nine compartments and varying diameter.

mental sequential cable model, M would have been:

$$M = \begin{pmatrix} g_{m,1} + g_{i,1} + \frac{c_m}{\Delta t} & -g_{i,1} & 0 \\ -g_{i,1} & g_{m,2} + g_{i,1} + g_{i,2} + \frac{c_m}{\Delta t} & -g_{i,2} \\ 0 & -g_{i,2} & g_{m,2} + g_{i,2} + \frac{c_m}{\Delta t} \end{pmatrix} \quad (3.5)$$

This is a direct consequence of the topology of a cell. As can be seen in Figure 3.7 A each compartment receives and gives input from and to all directly connected compartments. In contrast to the morphological representation, the graph becomes undirected. Still, M can be computed using the adjacency matrix, one just has to additionally consider the connectivity in the direction to the root. This can be simply achieved by using A^T (Cuntz et al., 2010) and so M with absolute values becomes:

$$M = G_m Ds + G_a(diag(sum(AD_{iv} + D_{iv}A^T)) - AD_{iv} + D_{iv}A^T) + \frac{C_m}{\Delta t}D_l \quad (3.6)$$

with A being the adjacency matrix
G_m: the specific membrane conductance
G_a: the specific axial conductance
C_m: the specific membrane capacitance
D_{iv}: diagonal matrices of compartment inverse volumes
D_s: diagonal matrices of compartment surfaces
and Δt the simulation step duration.

The voltage state of each node at time t is then calculated using the explicit forward Euler method

$$V_t = M \backslash (I_{inj,t} + V_{t-1}\frac{C_m}{\Delta t}D_l) \quad (3.7)$$

Simulations, parameter scans and the comparison with experimental data were all implemented in Matlab. Results were confirmed using the Neuron simulation environment (Hines and Carnevale, 1997).

3.6 software listing

The software listing ordered by primary usage:

- image processing, reconstruction and statistical analysis
  ImageJ 1.43, http://rsbweb.nih.gov/ij/, image viewer/processor: initial screening, filtering, conversion of images and stacks
  Mathworks Matlab 2010a, http://www.mathworks.com, numerical computing environment, morphological reconstruction, statistical analysis, initial visualization, code prototyping

external Matlab toolboxes and functions,
TREES toolbox, http://www.treestoolbox.org,
Mathworks' statistics and image processing toolbox,
Moo K. Chung's roiread for importing ImageJ ROI files, http://www.stat.wisc.edu/~mchung/softwares/ImageJ/roiread.m,
Robert Schleicher's ibar for bar plot customization, http://www.mathworks.com/matlabcentral/fileexchange/

- visualization
Blender 2.49b, http://www.blender.org, 3D modeling software: ray tracing of reconstructed cells
OpenGL, http://www.opengl.org/, interactive OpenGL rendering
Inkscape 0.47, http://www.inkscape.org, vector graphics editor: figures and post-processing
OmniGraffle 4.2.3, http://www.omnigroup.com/products/omnigraffle/, vector graphics editor: figures and post-processing
Keynote, http://www.apple.com/de/iwork/keynote/, presentation, figures and post-processing
Gimp 2.6.8, http://www.gimp.org/, bitmap editor: figures and post-processing
Visage Imaging Amira 5.2, www.amira.com, visualization tool: volumetric visualization and stereoscopic imaging

- file formats
SWC, described in (Cannon et al., 1998), stores neuro-morphological data
XML (eXtensible Markup Language), http://www.w3.org/XML/, storage of reconstruction setups
COLLADA (COLLAborative Design Activity), http://www.collada.org industry standard for exchanging 3D model data: storage format for the polygon data
X3d, , ISO standard XML-based file format for representing 3D computer graphics: storage format for the polygon data

- movie processing
iMovie '09, http://www.apple.com/de/ilife/imovie/, cutting, merging and converting movies
ffmpeg 0.5, http://www.ffmpeg.org, open source movie conversion tool, compiled using Macports for movie conversion and creation from rendered image sequence

- additional frameworks
Python 2.6, http://www.python.org, multipurpose scripting framework, with numpy 2.1.1, numerical library: used for Blender scripting
Java 6, http://www.java.com, multipurpose programming framework, with the

MatriX3d class: platform and language independent sampling of cylinders to polygons

Processing 1.0, http://processing.org, visualization scripting framework: interactive OpenGL visualization

- text editors
  TeXShop 2.33, http://pages.uoregon.edu/koch/texshop/, Latex editor with Latex, typesetting system: scientific writing
  VoodooPad Pro 4.2.3, flyingmeat.com/voodoopad/, desktop wiki: for general information keeping, brain storming and sketching
  Eclipse, http://www.eclipse.org/, multipurpose IDE, with the pydev plugin: Python programming
  Smultron, smultron.sourceforge.net/, multipurpose coding editor: various coding

- operating systems
  Mac OS 10.6, http://www.apple.com/
  Windows XP SP3, http://www.microsoft.com/

- hardware plattform
  MacBookPro 2,2, Intel Core 2 Duo, 2.16 GHz, 3 GB Memory
  G5 Quadcore PowerMac, 2x2 2.7 GHz G5, 2 GB RAM
  Dell Optiplex, 2.1 Dual Xeon, 16 GB RAM

4 results

4.1 morphological characterization of LPTCs in blow flies

The interindividual constancy and variability of LPTC morphology were studied in four identified cell types: the equatorial and the northern cell of the horizontal system (HSE and HSN) and two members of the vertical system (VS2 and VS4) (Fig. 4.1).
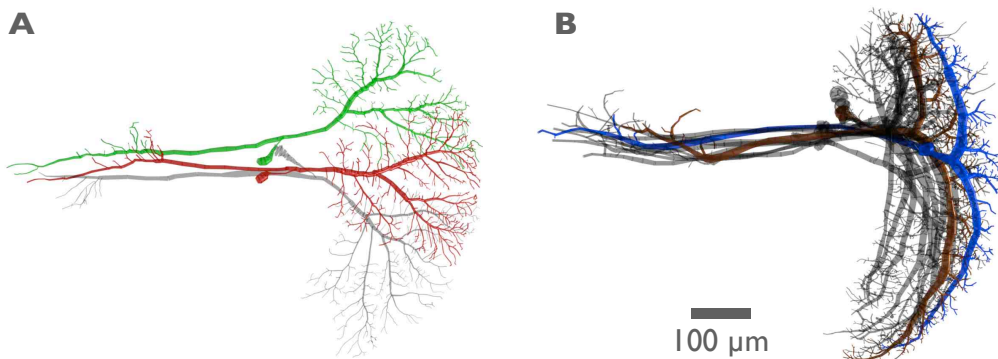
Figure 4.1: Cell target selection. (A) All three cells of the HSE network: HSN (green), HSE (red) and HSS (grey). HSE and HSN were selected for this analysis. (B) All ten VS cells: VS1-VS10, with highlighted VS2 (blue) and VS4 (brown). Selected cells were easily identifiable in all flies.

qualitative analysis

All selected cells were reliably identifiable by their distinct position in the lobula plate as well as their discriminating receptive field properties (Table 4.1). Taken the morphology alone, T-shaped VS cells could be easily distinguished visually from roundish-shaped HS cells. Within one cell class, cells showed identifiable yet less obvious characteristics. Looking at the finer dendritic branches, one was unable to consistently identify reoccurring patterns in the same identified cells from different individuals. This was tested with small pieces of branching patterns from different HS and VS cell images shown in a randomized order. Subjects were unable to reliably identify cells based on these branching pieces. This was in line with previous conclusions (Hausen, 1982), where the branching pattern of different HS cells were described qualitatively.

LPTC database

A representative database of LPTC images was created, capturing as much morphological detail as possible. Two-photon image stacks were acquired from cells filled with fluorescent dye in the living blowfly, *Calliphora vicina*. Subsequently, the anatomy of each neuron was manually traced and described by a set of connected cylinders (using custom-made software, see details in the materials and methods chapter 3). Each identified cell type was represented by at least ten individuals from different flies (Fig. 4.2 and Fig. 4.3). Only completely filled cells were taken into account and though the

cell ID	lobula plate location	optimal stripe stimulus, orient. and loc.	morphological characteristic
HSN	dorsal, anterior	left-right, dorsal	round, kidney-shaped
HSE	equatorial, anterior	left-right, central	round, symmetric
VS2	lateral, posterior	up-down, frontal	T-shaped, balanced dorsal and ventral primary dendrite length
VS4	central, posterior	up-down, medial	T-shaped, ventral primary dendrite length longer than dorsal

Table 4.1: Qualitative characteristics to identify the cells. All targeted cells could be easily distinguished by their location in the lobula plate, the preferred orientation of their responses to a moving stripe pattern, their location in the visual hemisphere and the morphological structure of the cells.

analysis was focused on the dendritic branching, soma, axon were also reconstructed and digitally labeled in the reconstruction in order to define the specific context of each dendrite.

The idea was then, in line with previous publications (Hillman, 1979; van Pelt and B., 1999; Uylings and van Pelt, 2002), to use statistical distributions over morphological parameters thereby isolating key features of dendritic branching in a quantitative manner. Next to classical branching parameters (see below) the so-called dendrite spanning field (Hausen, 1982) was parameterized. The spanning field was defined by drawing a contour around the dendrite at a distance of 25 μm after orienting the reconstructed neuron along its axonal axis (Fig. 4.4A). Measures included the spanning field area in μm^2, the ratio of the convex hull and spanning field area as well as the global extent in all three dimensions. Parameters relating to the spanning field plainly reflected cell type specific differences: All four cells could be readily discriminated by their dendrite spanning field parameters (Fig. 4.5). HS and VS spanning fields were easily distinguished by either their convexity index (Fig. 4.5C) or the ratio of width against height (Fig. 4.5D). Finer differentiation of HSE against HSN and VS2 against VS4 respectively was provided directly by their relative location to the axonal axis (Fig. 4.5B), and accordingly by their centre of mass (Fig. 4.5F).

spanning field properties

The spanning field represents a rough, global description of a neuron's shape. Next, a closer look was taken at the branching structure and the topology of the four identified cell types. A total of 32 parameters and combinations were calculated, out of which six were chosen as representatives (Fig. 4.6). Considering branching-specific statistics (Fig. 4.7), qualitative distinction of HS and VS was possible only by detailed examination of path length to the root and branch order. Ratios between direct and

branching pattern
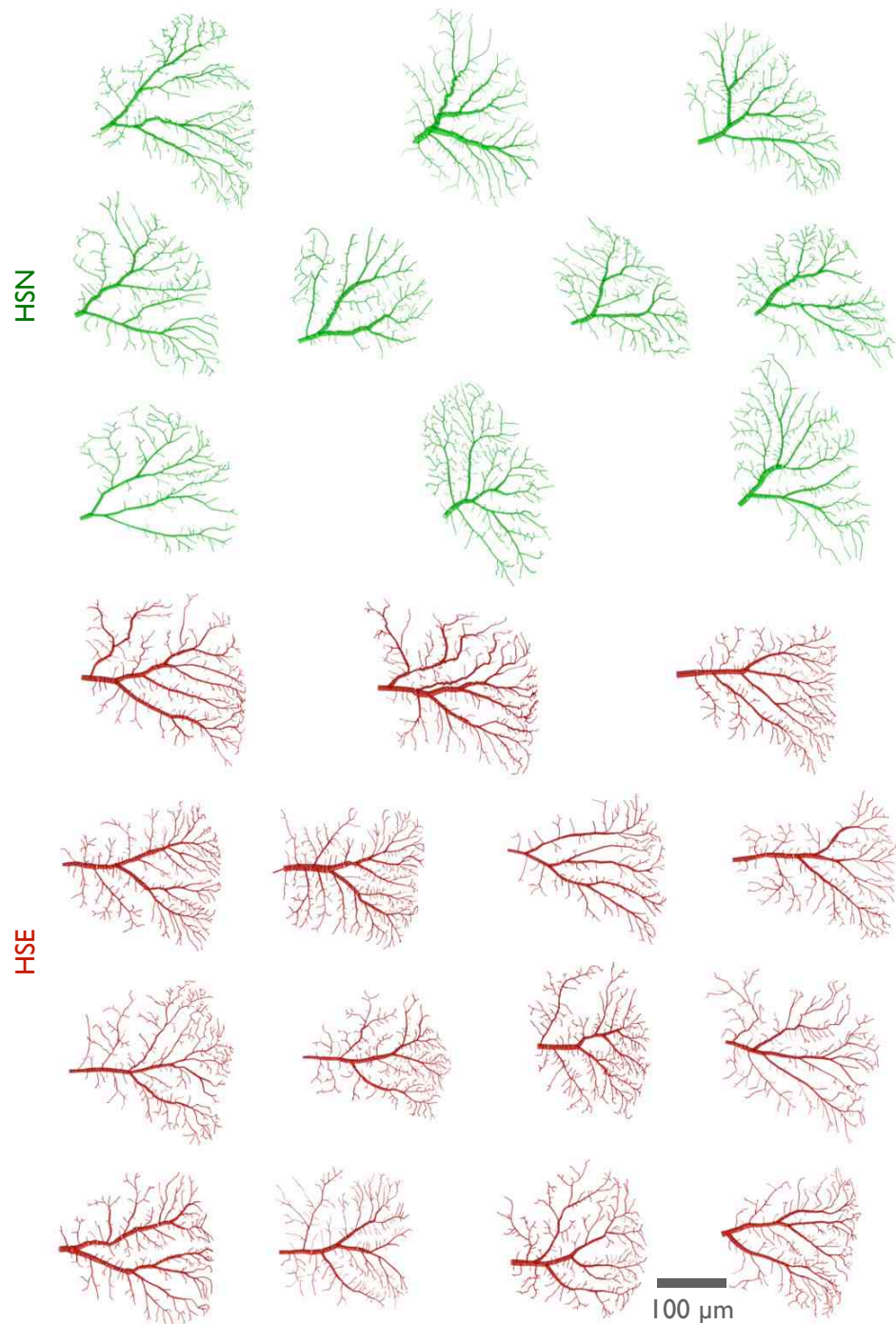
Figure 4.2: Database of reconstructed HS cells. 15 HSE cells and 10 HSN cells, identified by their location in the lobula plate, receptive field and shape properties. While the general shape appears stereotypic, the branching structure between different cells varied strongly.
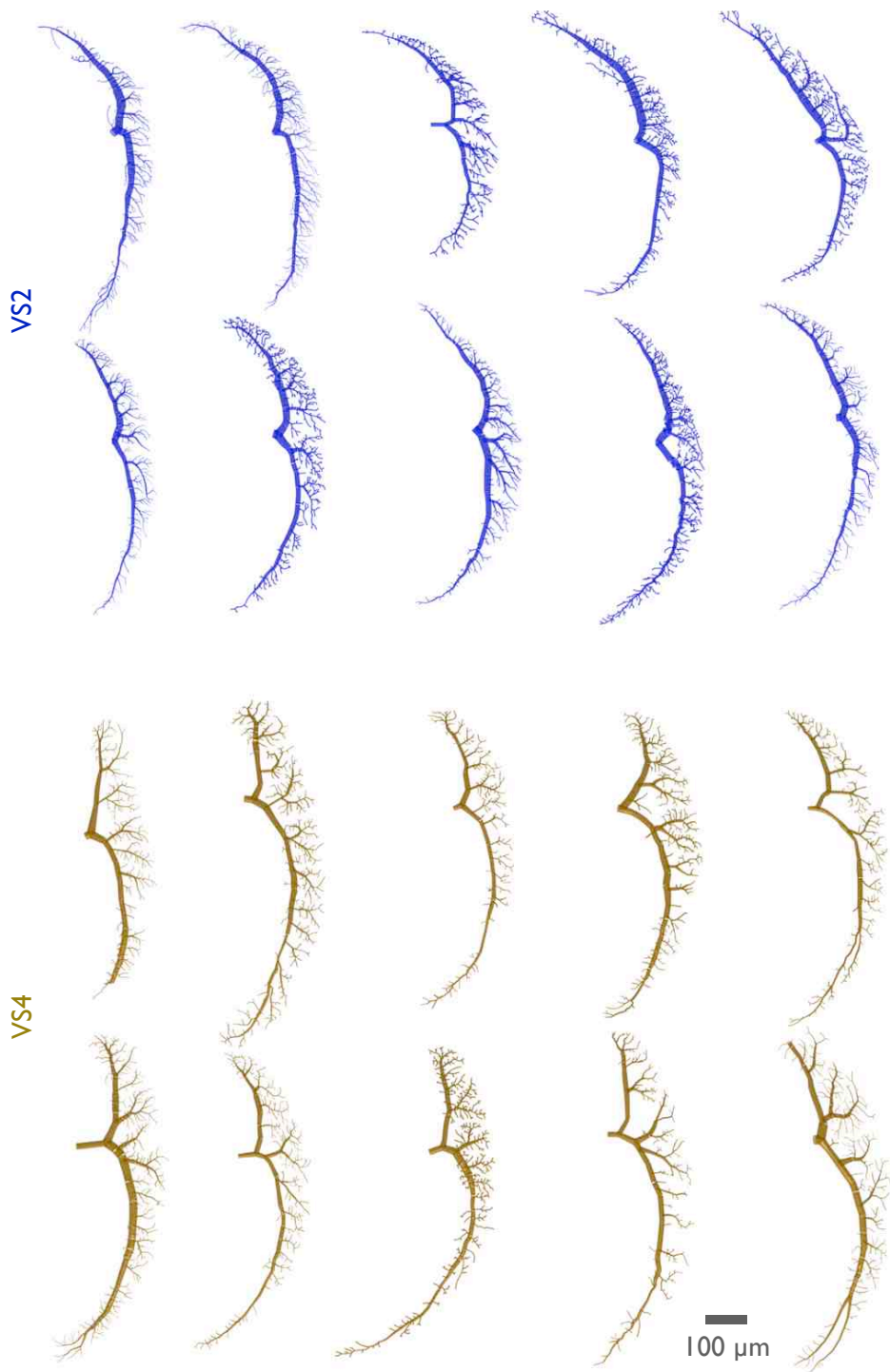
Figure 4.3: Database of reconstructed VS cells. 10 VS2 cells and 10 VS4 cells, identified by their location in the lobula plate, receptive field and shape properties. Finer branching structure appears arbitrary.
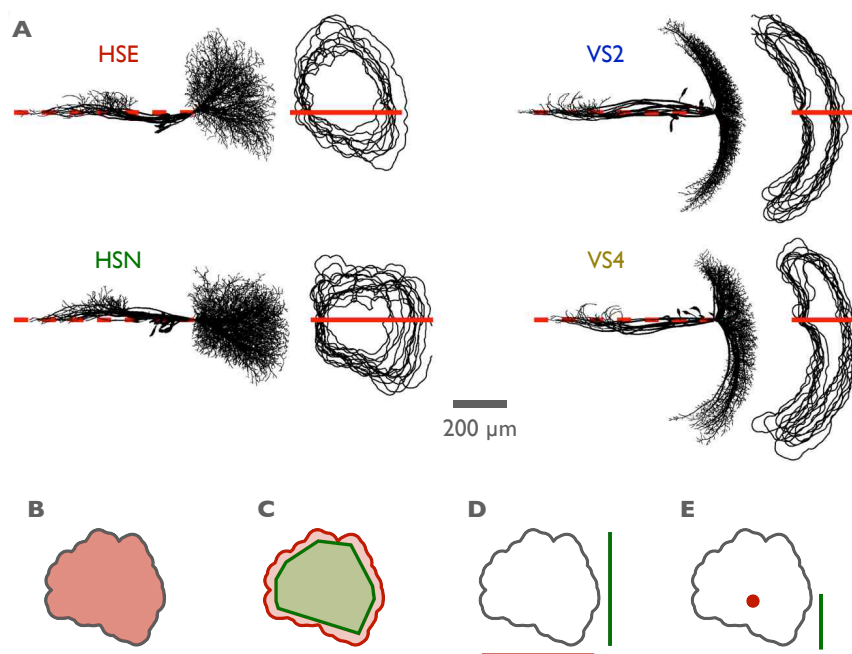
Figure 4.4: Spanning field analysis. (A) Cells were normalized by drawing an axonal axis (dotted red line) from the axonal terminal tip to the root of the dendritic tree. A 25 μm line was drawn around the dendrites and defined as spanning field. The dendritic spanning field was parameterized by i.e. the percentage of the area below the axonal axis (A, red line), (B) total area, (C) convexity index derived by the ratio of convex hull (green) to spanning field area (red), (D) width vs. height and (E) location of the center of mass in X and Y.
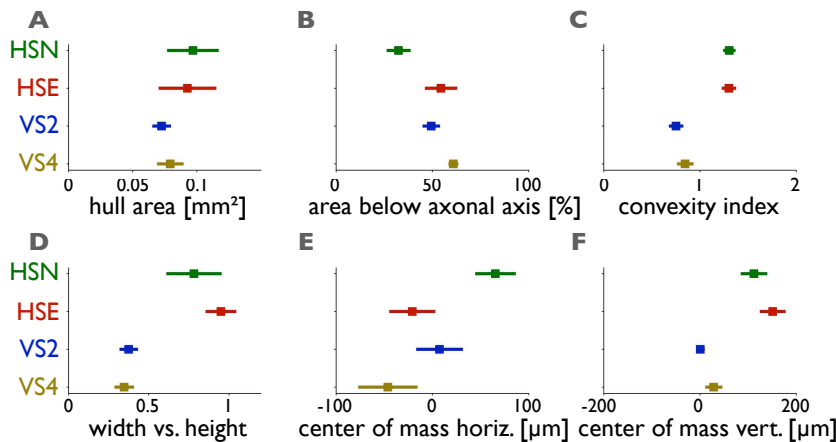
Figure 4.5: Spanning field parameters. Mean and standard deviation for each identified cell type and parameter explained in Figure 4.4. Some parameters allowed the classification of HS and VS cells (C, D), others finer differentiation into HSN and HSE (B, F), and VS2 and VS4 respectively (B, E, F).

path distances to the root (Fig. 4.7B) followed a narrow distribution close to one in all cases. Path length histograms (Fig. 4.7A) therefore corresponded to the Sholl intersection diagram (Fig. 4.7F), a measure typically used to describe branching structure. Branch length and branching angle reflected a very similar branching structure throughout all four identified cell types. No parameter allowed reliable identification of subtypes (HSN/HSE and VS2/VS4).

The descriptive power of spanning field parameters versus branching parameters was further investigated in a quantitative way, using cluster analysis (Fig. 4.8). Spanning field related parameters readily grouped individual cells into their respective cell types as shown simply by plotting convexity index values against the contextual relative location relative to the axonal axis (Fig. 4.8A). Even a high-dimensional clustering analysis on the basis of parameterized shape fits of the distributions in Fig. 4.7A-F or subsets of these did not allow the separation of the real cells into their respective groups. Best clustering was obtained using path length, density and branching order distributions which separated HS from VS cells but not the members of the two families (Fig. 4.8B). Therefore the spanning area best determines neuronal appearance, the particularities in branching parameter distributions might be merely a consequence of the neuronal target zone.

clustering

In order to identify the critical impact of spanning field shape on branching parameters, artificial dendrites were constructed covering the same region. Inside the contours of the original cells, random points were distributed following their respective density map. An iterative minimum spanning tree algorithm was launched starting at the

artificial cell synthesis
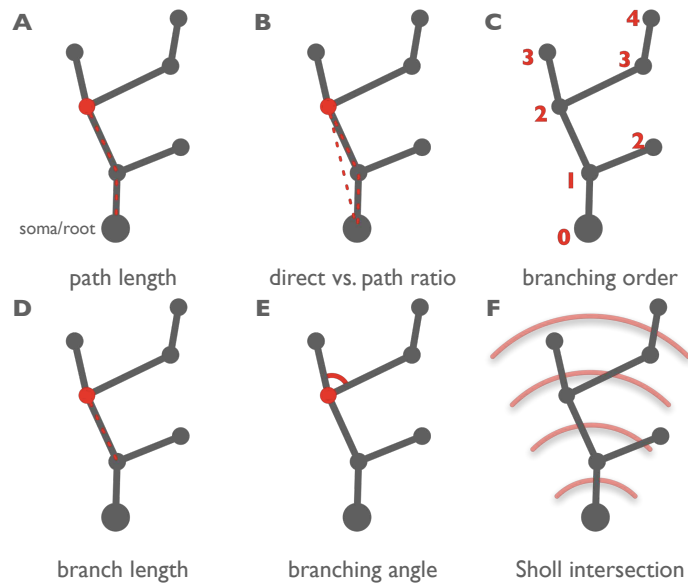
Figure 4.6: Parameters of branching pattern. Sketches exemplifying the selected branching parameters. Parameters were individually computed for each branch point and termination point. (A) Path length from the root to a branch/termination point, (B) a measure for local wiring efficiency measured by the ratio of the Euclidean distance to the root and the path length, (C) the hierarchical structure set by the branching order, starting with a value of zero at the root and progressively increasing with each branch point, (D) the branch length defined by the distance to the last branch point in direction to the root, (E) the angle between two sister branches and (F) the Sholl distance, a measure for the dendritic expansion calculated by drawing iso-spaced concentric circles around the root and counting the intersections with the cell.
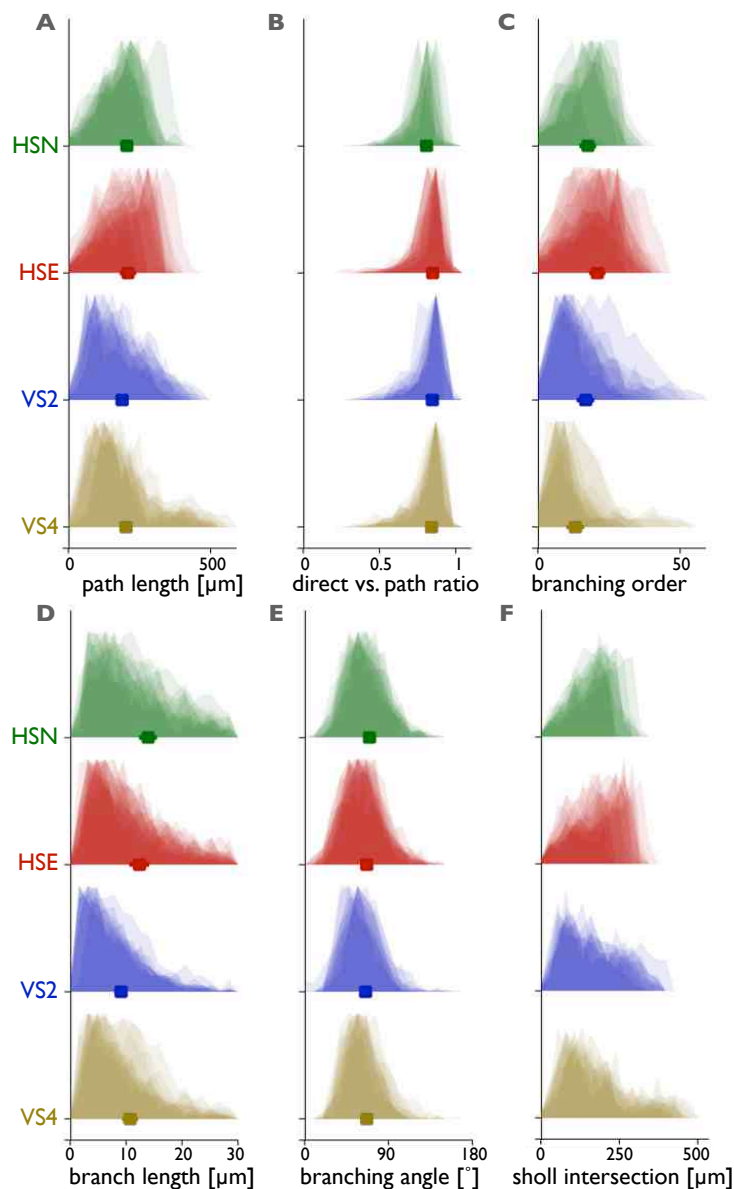
Figure 4.7: Branching parameter distribution. (A-F) Distributions according to the parameters described in Figure 4.6. Distributions are visualized using transparent curves, each representing one cell. The opacity and fuzziness of the overlays allow to estimate the similarity of the distributions within one identified cell type. Mean values are shown as boxes. VS and HS cells show quite different morphologies but their branching parameter distributions look very similar. Direct vs. path ratio (B) and the branching angle (E) are similar in all analyzed LPTCs. Some parameters allow the identification of HS and VS cells (A,C,F) but none reliable identification of subtypes (HSE/HSN and VS2/VS4).
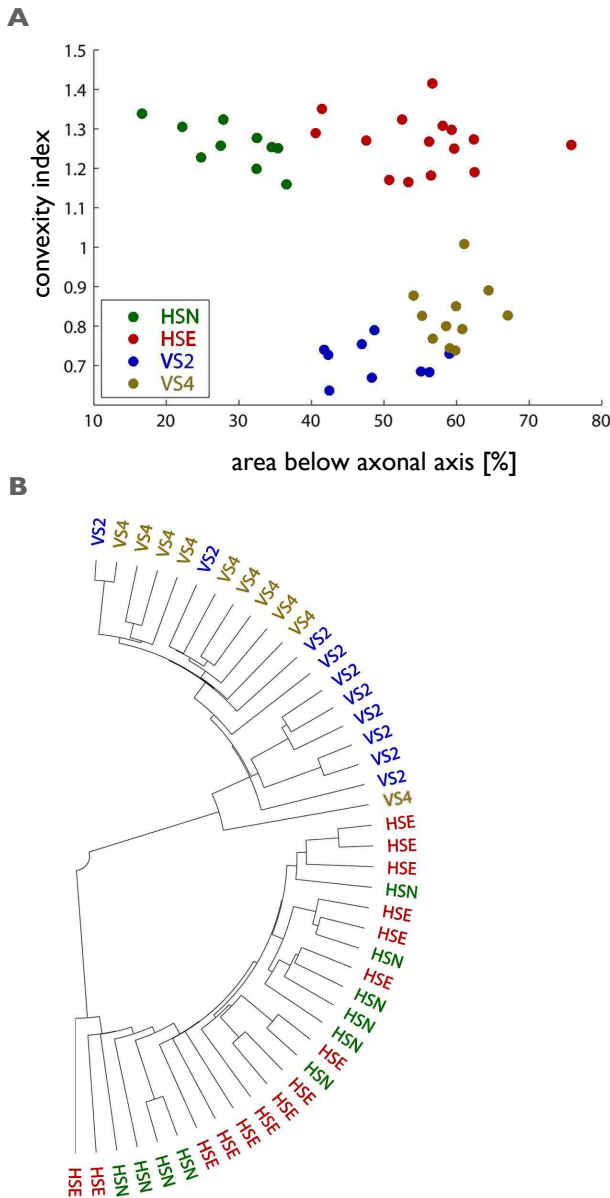
Figure 4.8: Clustering analysis. (A) Dot plot using two spanning field parameters. Each dot represents one cell. Color encodes the cellular identity. Cells can be well classified by their convexity index and the area below the axonal axis. (B) Branching parameters were fitted to generalized extreme value distributions (GEV). A GEV is defined by a shape, scale, and location parameter and hence, more flexible than a normal distribution only defined by mean and standard deviation. Each branching property distribution of each cell reconstruction was parameterized individually. Parameters were then assembled in cell specific feature vectors. Vectors were related using pairwise distance measures and clustered hierarchically according to their distance. Cluster results were plotted as dendrogram in order to illustrate their parameterized relation (see Matlab documentation for background). HS and VS cells can be easily distinguished, but not finer resolved into their subtypes.

coordinates of the real dendrite root (see methods chapter for details). At each step, a connection was added from the existing tree to one of the unconnected random points according to a cost function which minimized both total amount of wiring and total path length from the root to each point (Cuntz et al., 2007a). The number of random points was set to match the resulting number of topological points with the original dendrites. Improved appearance and overall path distance to the root was achieved by a subsequent smoothing step along primary branches.

This resulted in artificial dendrites confined to the same area as the corresponding *in vivo* dendrite reconstructions and similar appearance (Fig. 4.9). Interestingly, artificial dendrites also yielded quantitatively similar parameter distributions in all cases as seen in Figure 4.10, exemplified on HSN and VS2. VS and HS specific differences in distribution shape and mean value could be well reproduced. The exact same branching rule can therefore account for all individual morphologies after constraining the spanning field shape alone. It should be noted that the selected simple wiring constraints do not take into account neuronal proliferation. They ignore many previously proposed mechanisms of neuronal branching (Corty et al., 2009). Furthermore the algorithm works in a local fashion and does not necessarily lead to global optimization of the cost function. Considering all this, the artificial cells resemble their original counterparts surprisingly, though not perfectly well.

artificial cell statistics

As discussed in the materials and methods chapter 3 the algorithm can be adjusted to different cell morphologies by altering the balancing factor bf and correspondingly influencing the average path distances to the root. Qualitative and quantitative estimation of the best balancing factor both led to a value of 0.2. Visually, artificial dendrites grown with a bf of 0.1 and 0.2 resembled the *in vivo* reconstructions (Fig. 4.11). Lower values led to long, nested branches, while higher values resulted in star like dendrites. Numerically, the balancing factor was assessed by benchmarking the branching distributions of the artificial cells to ones obtained from the experimental data (Fig. 4.12). Different parameters required different optimal bf values. A balancing factor of 0.2 represented a compromise of all four branching distributions and performed quite well in all four cells types, considering the overall distributions.

bf estimation

The data presented here suggest that the morphological identity of the identified cell types is rooted in their spanning field properties. The branching structure and topology of LPTCs are then merely a result of a common branching rule that is constrained by the cell specific spanning field.

conclusion

Statistical analysis and synthetic modeling were performed together Dr. Hermann Cuntz. Fly preparation and image acquisition was done together with Renate Gleich and Dr. Juergen Haag. The project was supervised, structured and documented together with Dr. Hermann Cuntz and Prof. Dr. Alexander Borst. Results were
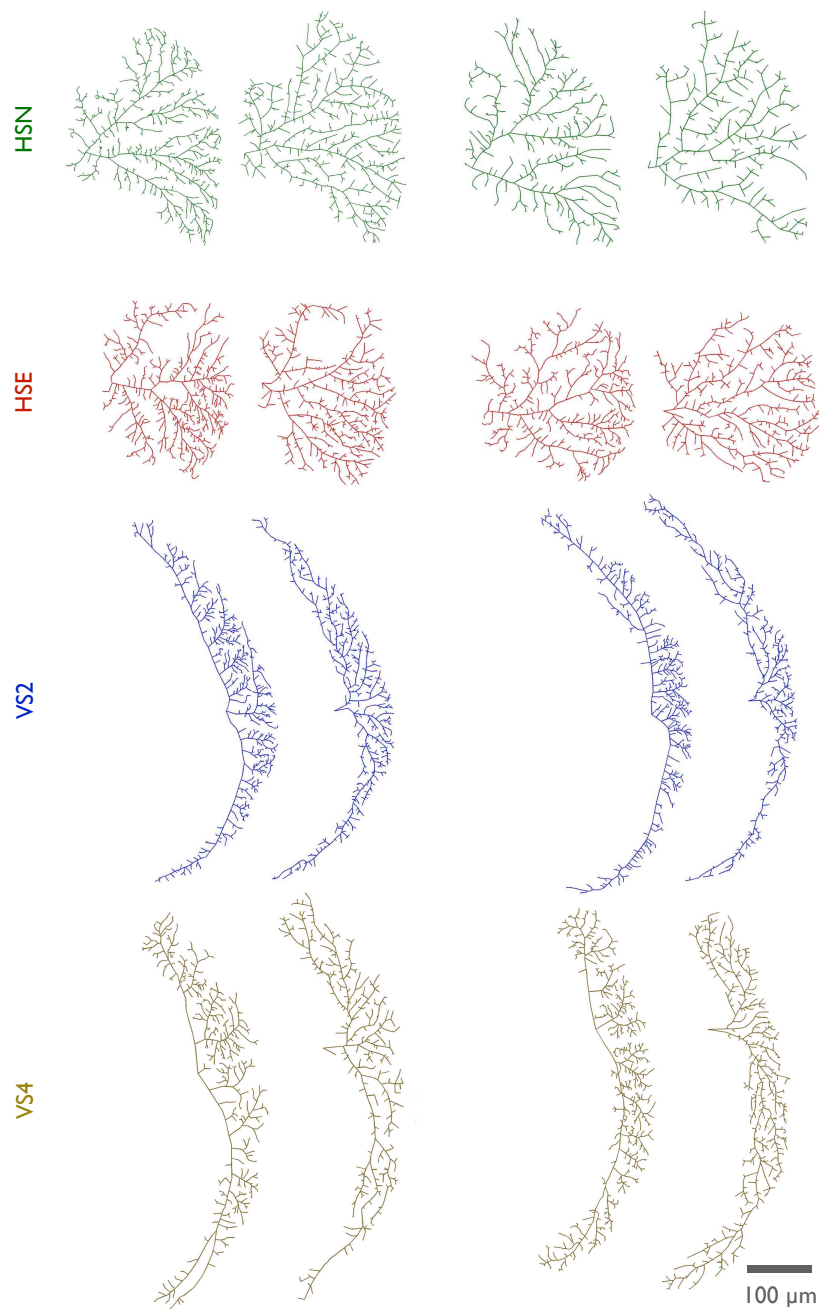
Figure 4.9: Computational synthesis of LPTCs. Real (left) and synthetic cell (right), two examples for each cell type. Synthetic cells were grown into the area of their *in vivo* counterpart using the same branching rule for all LPTCs. This resulted in realistic morphologies.
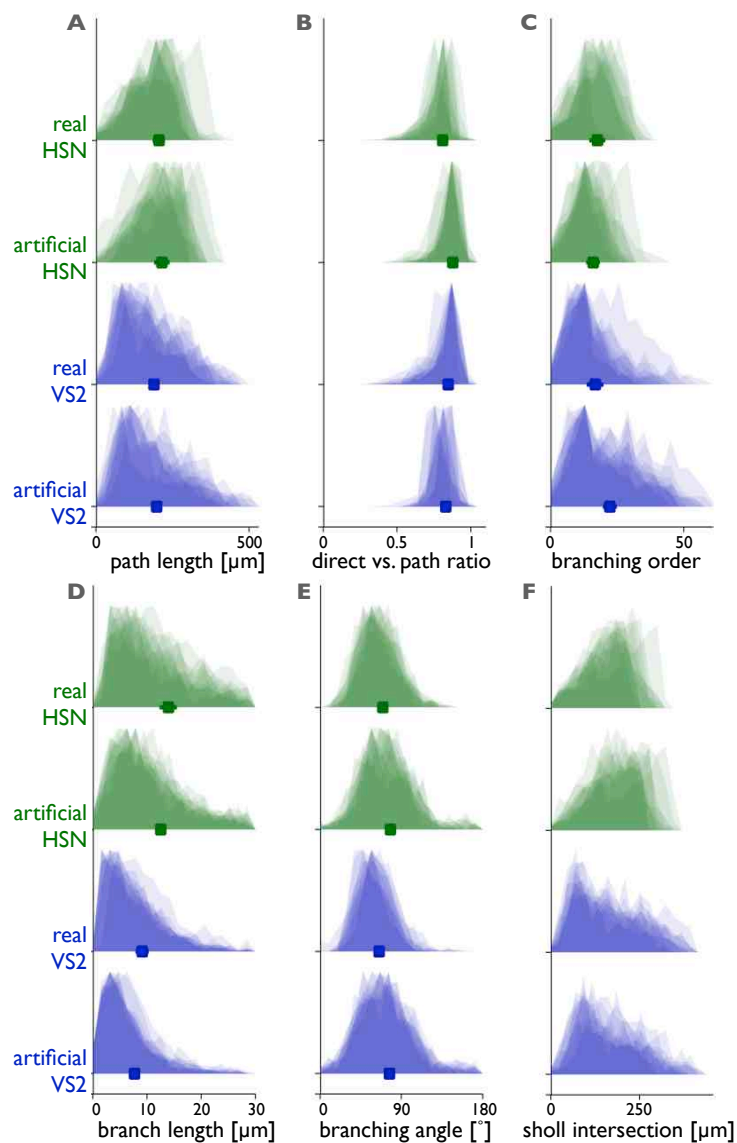
Figure 4.10: Evaluating synthetic branching patterns. HSN and VS2 cells as examples for the parametric performance of the growth algorithm, *in vivo* cells in the upper row, artificial cells in the row below. Characteristic shape and mean values are reproduced in all distributions (A-F).
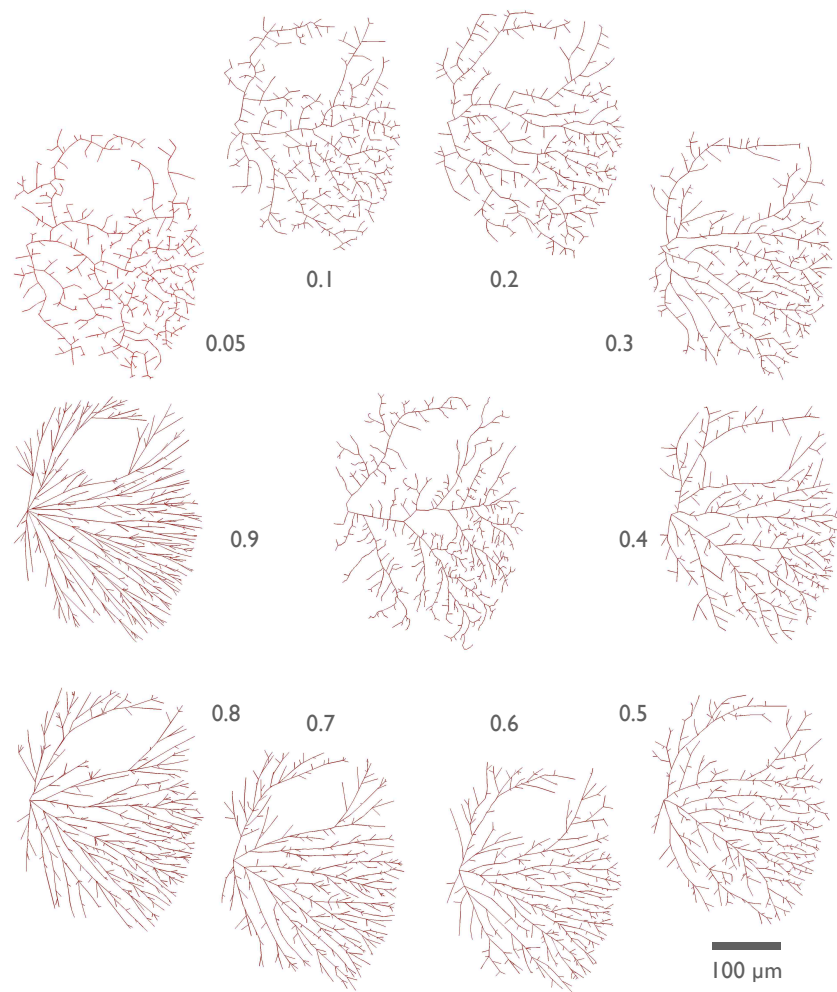
Figure 4.11: Visual evaluation of balancing factors. Artificial generation of cells grown into the same spanning field of an *in vivo* HSE reconstruction (middle plot) using different balancing factors. Factors of 0.1 and 0.2 lead to realistic results.
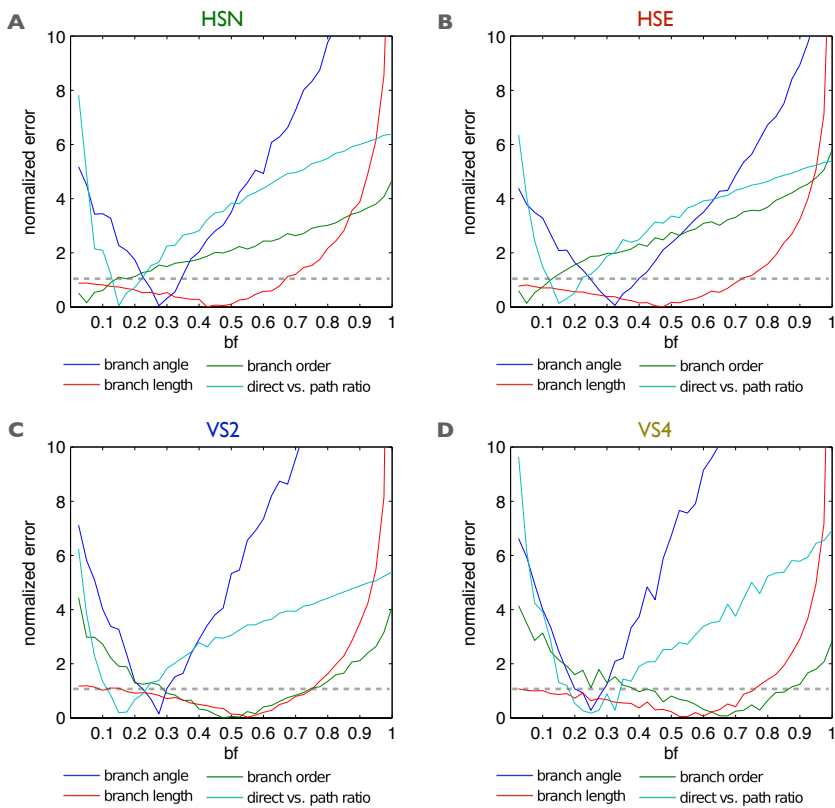
Figure 4.12: Analytical benchmark of balancing factors. The performance of the growth algorithm to reproduce branching parameter statistics was evaluated using different balancing factors (0.05 to 1). Each cell type was benchmarked individually (A-D). For each *in vivo* reconstruction and bf value one artificial cell was created and the branching parameterized. Curves represent mean errors over all cells of one bf normalized by the *in vivo* standard deviation. Values below the gray dotted line (error=1) are within the *in vivo* standard deviation. No clear optimum can be identified, but rather an optimal range from 0.1 to 0.3.

published in two articles:

H. Cuntz, F. Forstner, A. Borst, and M. Häusser. One rule to grow them all: a general theory of neuronal branching and its practical application
PLoS Comput Biol, 6(8): e1000877, 2010

The morphological identity of insect dendrites.
H. Cuntz*, F. Forstner*, J. Haag, A. Borst.
PLoS Comput Biol. 4(12):e1000251, 2008
(* equal contribution)

Robust coding of flow-field parameters by axo-axonal gap junctions between fly visual interneurons
H. Cuntz, J. Haag, F. Forstner, I. Segev, A. Borst.
Proc Natl Acad Sci USA.;104(24):10229-10233, 2007

4.2 morphological analysis of down-scaled LPTCs in fruit flies

HS cells in Drosophila

The HS system in *Drosophila* has been morphologically identified three decades ago (Fischbach and Heisenberg, 1984; Scott et al., 2002). Interestingly, the HS cell number and morphological appearance seem to be conserved not only in different individuals of the blow fly but even in different fly species. Recently, an electrophysiological study has shown that HS cells in *Drosphila* have similar response properties as their counterparts in *Calliphora* (Schnell et al., 2010). The subject of the following analysis was to investigate whether the conclusion held true for the similar, scaled down HS system of *Drosophila*. Furthermore, a quantitative comparison of *Calliphora* and *Drosophila* LPTCs was accomplished en passant.

identification and cell labeling

While *Calliphora* cells needed to be filled intracellularly to capture their three dimensional extension, in *Drosophila* a previously described genetic driver line NP0282 (Schnell et al., 2010; Otsuna and Ito, 2006) facilitated specific labeling of HSN and HSE cells in both optic lobes and dramatically simplified the preparation procedure (Fig. 4.13B). Once identified in one individual, cells could be simply imaged assuming conservation of cell specific expression in all targeted individuals (Brand and Perrimon, 1993).

qualitative assessment

Figure 4.13 depicts the results of a *Drosophila* NP0282 image stack with genetically labeled HSN and HSE cells and a *Calliphora* HSN/HSE double fill. The cells of the
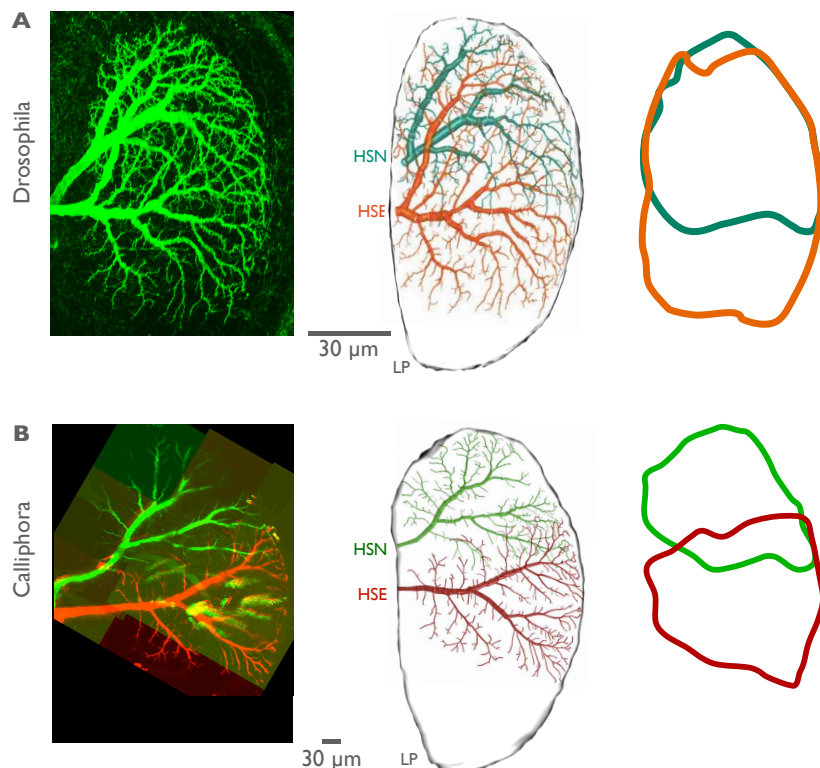
Figure 4.13: HS cells in fruit fly and blow fly. (A) *Drosophila* HSN and HSE cell, GFP labeled confocal microscopy image (left), cylinder reconstruction (middle) and covered area outline (right). (B) *Calliphora* HSN and HSE cell from one individual, 2-photon-microscopy multi-stack image of a Alexa green and red double fill (left), equivalent cylinder reconstruction (middle) and covered area outline (right). LP sketched from other recordings. Cells in both flies look similar and are easily identifiable by their relative and absolute location in the LP. However, the overlap between HS cells in *Drosophila* differs largely from the one in *Calliphora*. LP sketched from other recordings (image acquisition by Shamprasad Varija Raghu, PhD and Dr. Jürgen Haag).

fruit fly are downscaled by a factor of four, compared to the corresponding *Calliphora* LPTCs. *Drosophila* HS cells shows a very similar shape and location within the lobula plate and can be easily identified by their relative and absolute location: HSN is located in the dorsal part, HSE centers in the equatorial part of the lobula plate. Both cells lie in the anterior layer. A major difference to their counterparts in *Calliphora* can be observed in the spanning fields of *Drosophila* HS cells. While the HSN cell reaches until the LP midline, HSE covers major parts of the lobula plate, including most of the HSN spanning field. The general branching structure in both flies appears similar, but the complexity in *Drosophila* is clearly higher than in *Calliphora*, which is surprising considering the reduced optical resolution in smaller flies (Hardie, 1984; Götz, 1968). Also, the primary dendrites branching from the dendritic root appear much thicker relative to the overall size of HS cells in the fruit fly.

It could not be excluded that the cells in fact have a different identity, e.g. so far no CH cells have been identified in *Drosophila*. CH cells in *Calliphora* show a much higher complexity and LP coverage than HS cells (Meyer et al., 1986; Eckert and Dvorak, 1983). Hence, the high complexity and LP coverage of the here analyzed *Drosophila* cells could hint to a different cell type. On the other hand, CH cells have been confirmed to perform dendro-dendritic interactions via electrical and chemical synapses (Gauck et al., 1997). Experiments performed by Shamprasad Varija Raghu, PhD indicated no traces of presynaptic components in the dendrites of the here described *Drosophila* LPTCs (Raghu et al., 2007). In these experiments a genetically engineered Synaptobrevin-mRed was used as agent for presynaptic sites. Synaptobrevin represents an essential protein in the process of synaptic vesicle formation and degradation in the presynaptic terminal. Confocal images of HS and VS MARCM clones expressing Synaptobrevin-mRed and membrane attached GFP (mCD8-GFP) showed presynaptic sites to be exclusively localized in the axonal terminals. It was therefore presumed that these cells are indeed HS cells, although misattribution cannot be excluded.

reconstruction database

Confocal microscopy imaging was applied to establish a representative database of HSN and HSE morphologies. The genetic labeling and additional GFP tagged antibody treatment resulted in images with very good signal to noise ratio and consistent labeling penetration. Cells were not imaged in living animals but brains carefully remove and mounted to avoid compression artifacts. Cylindrical reconstructions of the cells took much longer ($\sim$5 hours each) than in *Calliphora* due to the higher branching complexity and the close proximity and overlap between the two cells. A total number of 10 HSE and 10 HSN cells were reconstructed from both optic lobes in five flies (Fig. 4.14). In the NP0282 line many other cells outside of the lobula plate were co-labeled and reliable reconstruction of axons and somata was not possible therefore (Schnell et al., 2010). Figure 4.15 confirms the qualitative finding of much higher complexity found in *Drosophila* HSN and HSE cells. *Drosophila* cell reconstructions
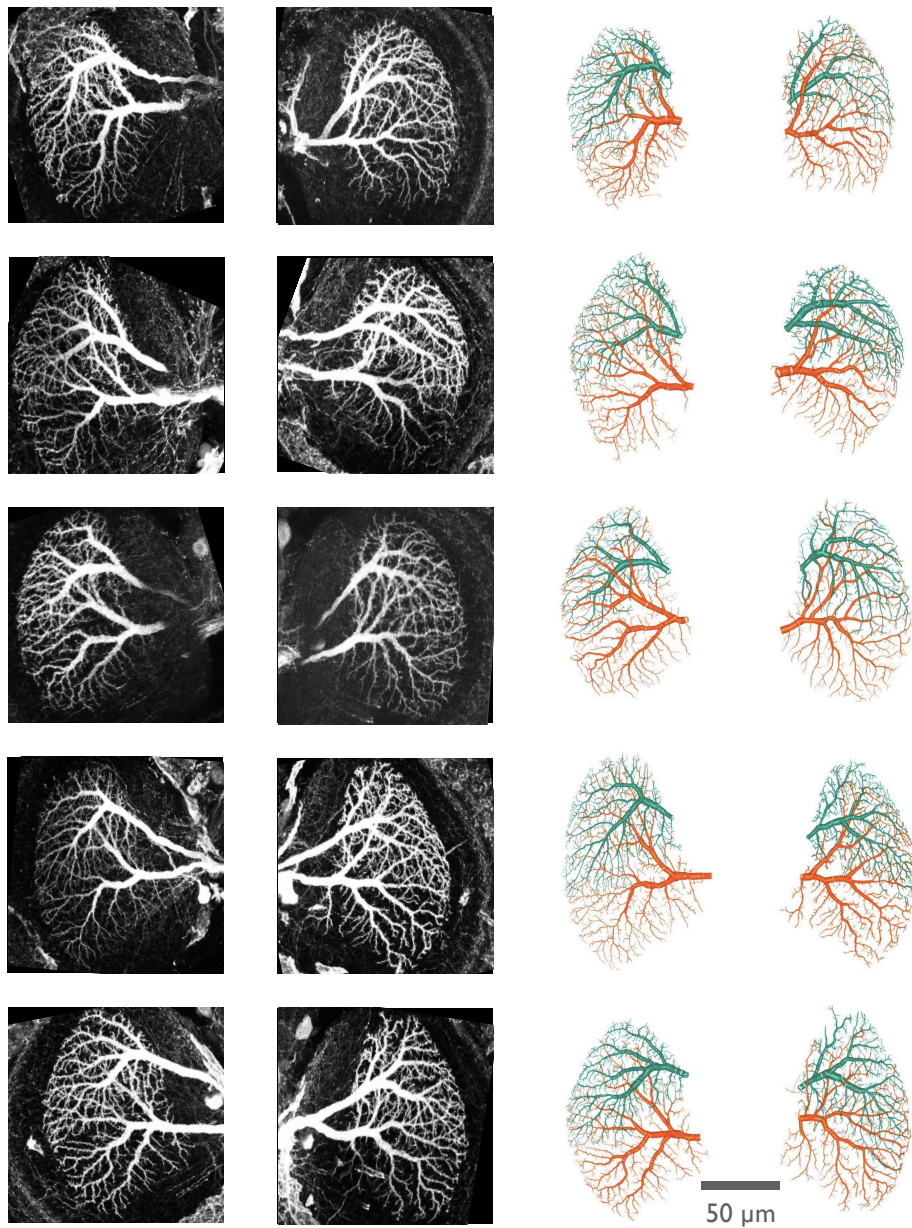
Figure 4.14: Drosophila HS database. 10 HSN and 10 HSE cells from five flies (both optic lobes), genetically GFP-labeled, imaged with confocal microscopy (left two columns) and reconstructed as cylinder models (right two columns). Although co-labeled with GFP, separation of the cells was possible as branches did not fasciculate (images recorded by Shamprasad Varija Raghu).

contain a little bit more than double the amount of branch points found in *Calliphora* reconstructions.
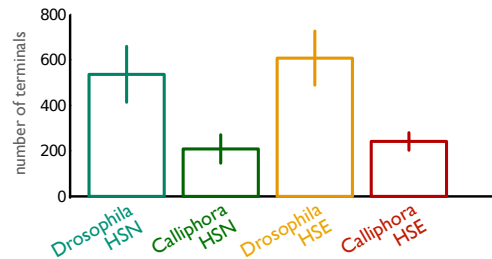
Figure 4.15: Comparison of complexity Mean and standard deviation of the number of branch points of HSN and HSE cell reconstructions in both fly species. *Drosophila* cell reconstructions contain more than double the amount of branch points found in *Calliphora* reconstructions.

orientation normalization

In order to align the dendritic spanning fields from different specimen the missing axonal reconstructions required the use of a different context clue than the axonal axis used in *Calliphora*. Instead of using the axonal midlines, the orientation of the cells were normalized by taking the combined spanning fields and minimizing the resulting overall width (Fig. 4.16). Horizontal lines were then drawn as reference through the dendritic root of the orientation normalized cells and termed root line. Root lines were later used for the measurement of area symmetry i.e. fraction of area below the root line. The procedure works well in the lobula plate since the combined dendritic spanning fields closely resembled the outline of the northern and equatorial lobula plate (this was confirmed with background stains, see section 4.4, Fig. 4.30).
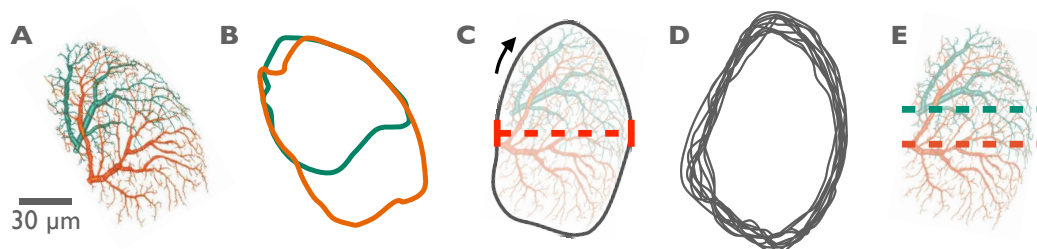
Figure 4.16: Orientation normalization of Drosophila HS cells. (A) Unregistered raw reconstructed HSN(turquoise)/HSE(orange) pair. (B) Dendritic coverage of each cell drawn as outline. (C) The combined outline was rotated until the minimum width was reached. (D) Overlay of 10 normalized HSN/HSE outlines. (E) Horizontal lines through the dendritic root of cells serve as reference line to distinguish upper and lower dendritic spanning field. (E) Root lines were then defined as horizontal lines drawn through the dendritic root of the orientation normalized cells.

spanning field

The similarity of the roundish convex spanning fields of HS cells in both *Calliphora*

and *Drosophila* was also apparent in the parametric space (Fig. 4.17). Still, due to their different scales, *Calliphora* and *Drosophila* cells could be easily separated by their spanning field properties e.g. the spanning field area (Fig. 4.17A) or the center of mass in the vertical dimension (Fig. 4.17F, different scales). The same held true for HSN and HSE cells of *Drosophila*, where hull area (Fig. 4.17A) and convexity index (Fig. 4.17C) allowed a clear discrimination. As in the *Calliphora* analysis of section 4.1 spanning field properties contained enough cell specific differences to classify each identified cell type in both species.
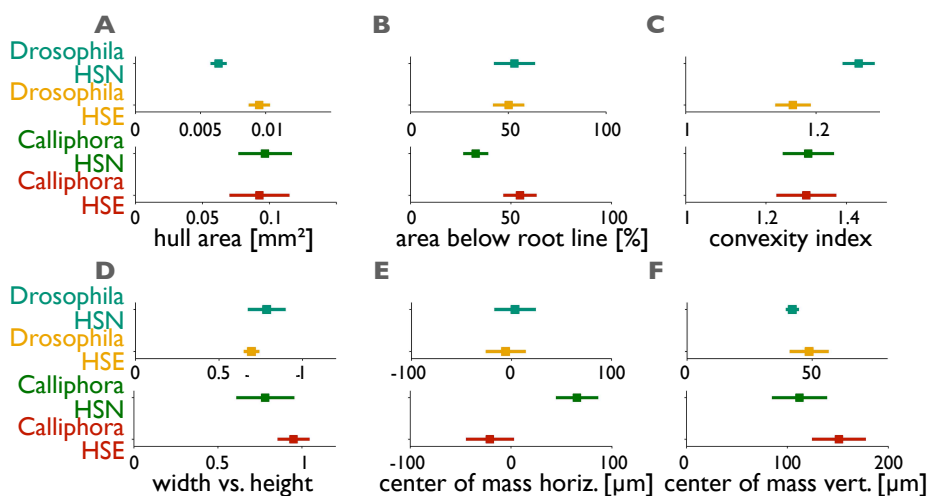
Figure 4.17: Spanning field parameterization in Drosophila. (A-F) Spanning field parameters of *Drosophila* (upper two rows) and *Calliphora* (lower two rows) HS cells. Mean and standard deviation for each identified cell type, parameter calculations are explained in Figure 4.4. Some parameters allowed the classification of *Drosophila* and *Calliphora* HS cells (A, F both with with different scales), others finer differentiation into *Drosophila* HSN and HSE (A, C).

Figure 4.18 depicts the branching pattern analysis. Direct vs. path ratio and the branching angle distributions (Fig. 4.18B and E) seemed to be largely conserved over the two species and didn't allow specification of *Drosophila* or *Calliphora* fly neurons. The downscaling and higher complexity led to shifted distributions in case of path and branch length, branching order and Sholl analysis (Fig. 4.18A and F). Interestingly the shape of the curves was similar in all distributions. This could be most probably attributed to the similarities in spanning field shape (also compare to distributions of VS cells in Figure 4.7). The *Drosophila* cells showed a lower deviation within one cell type as seen in the fuzziness among distribution curves, possibly due to the reduced degree of genetic variability as a result of the genetic balancing and closer relationship of the *Drosophila* flies.

branching statistics

A cluster analysis underlined the discriminative potential of the parameterized spanning

clustering
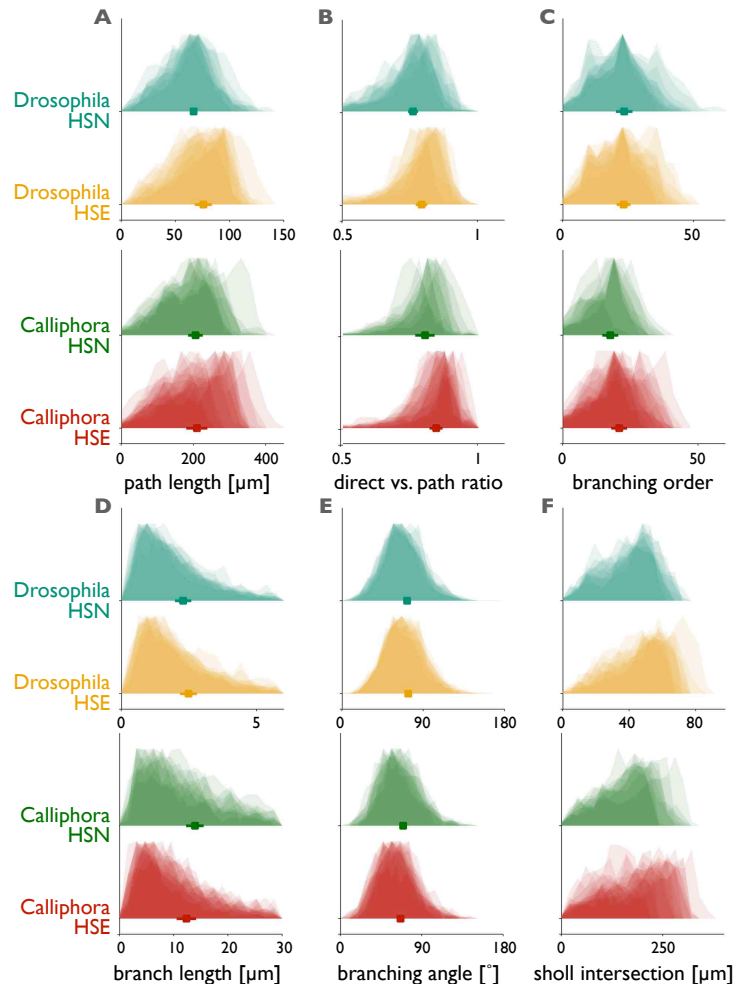
Figure 4.18: Branching parameter distribution. (A-F) Distributions according to the parameters described in Figure 4.6, upper two rows *Drosophila*, lower two rows *Calliphora*. HS cells from different species show branching parameter distributions all shaped similarly. Only metrics affected by the scaling led to significant differences (A,D,F)

field properties. In comparison to their *Calliphora* counterparts the *Drosophila* HS cells could not be separated by the area below the drawn root line, but instead by their convexity index (Fig. 4.19A). This might be a result of the different context cues used. Branching properties only allowed a separation of *Calliphora* and *Drosophila* HS cells and proved the general applicability of the cluster analysis (Fig. 4.19B). The branching statistics clearly failed to distinguish different HS cells in both species.

intra-individual comparison

Co-labeling of same cells in both hemispheres allowed the direct comparison of the variability within one and between different individuals. Again, a quiz in a Memory game fashion was developed to investigate the possible visual identification of two cells from the same animal. Each reconstruction was printed out on a single individual piece of paper, marked with a hidden fly ID. Paper sheets were mixed and it was tried to sort the cells by individuals. It was not possible to consistently relate two cells to one individual fly. Quantitative analysis of branching structure and spanning field properties yielded no significant difference in similarity between different lobes and different animals. These observations are visualized in the results of the cluster analysis (Fig. 4.19). Here, two cells from the same animal are labeled with the same letter. There is no significant co-localization of cells from the same animal neither within the dot plot of the spanning field properties (Fig. 4.19A) nor in the dendrogram of the parameterized branching characteristics (Fig. 4.19B). The value of this analysis was limited though, due to the small number of animals (n=5).

A small, preliminary screen (n=3) of double Alexa injections of cells from different optic lobes in *Calliphora* and a subsequent qualitative assessment indicated that this finding might also be true for blowflies (data not shown). The variability in same and different animals supports the idea of a common branching rule which is not rigidly constraining branching but rather optimizing costs within a fixed target area.

morphological synthesis

Next, the growth algorithm was tested on fruit fly neurons. The very same operations as described in the previous section were carried out. Only a few critical parameters needed to be adjusted to account for the difference in scale. The smaller cells required a finer resolution to estimate local spanning field properties: Branches were sketched by borders drawn by 6 μm distant contour lines instead of 25 μm and additionally the grid for the density calculation was down-sized too. The algorithm was able to synthesize cells with very similar appearance. Error curves allowed a selection of the balancing factor. Interestingly, it matched the bf value set for *Calliphora* cells (Fig. 4.20C and D), which is not surprising taken the similarities in general appearance and branching distributions.

conclusions

With a slightly modified analytical workflow it was possible to reproduce the results from the big fly: The morphological identity of *Drosophila* HS cells seems to be based on their spanning field characteristics alone. The branch pattern can be explained
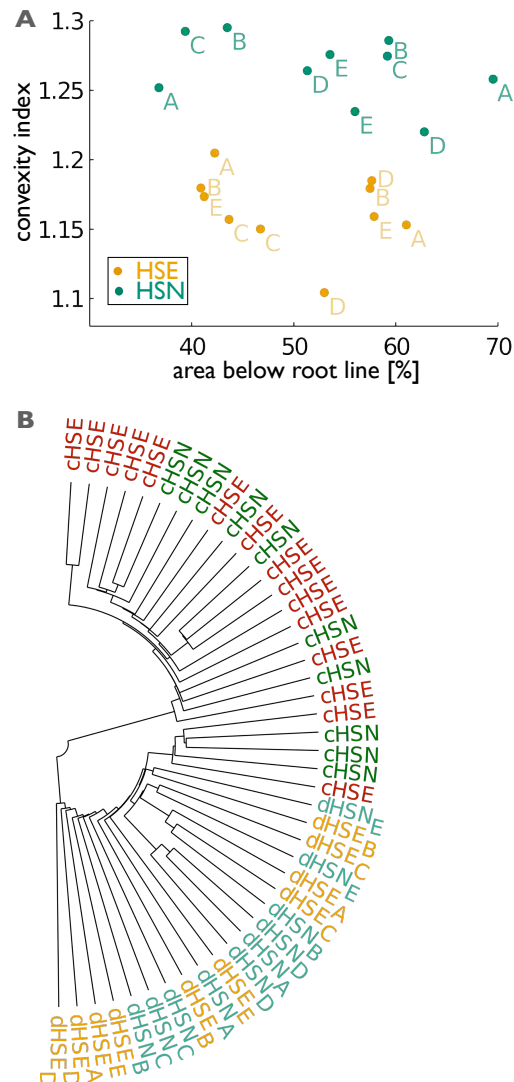
Figure 4.19: Clustering analysis. (A) Dot plot using two spanning field parameters. Each dot represents one cell, color coded by it's cellular identity. Letters indicate animal labels, the cells were reconstructed from. The area below root line was computed as described in Figure 4.16E. The convexity index was retrieved as mentioned in Figure 4.4C. Cells can be classified according to their convexity index. Two cells from the same animal do not co-locate. (B) Each branching property distribution of each cell reconstruction was parameterized individually. Parameters were then assembled in cell specific feature vectors. Vectors were related using pairwise distance measures and clustered hierarchically according to their distance. Cluster results were plotted as dendrogram in order to illustrate their parameterized relation (see Matlab documentation for background). HS and VS cells can be easily distinguished, but not finer resolved into their subtypes. HS cells from different species can be resolved but cells are parametrically intermingled within one species. Cells from the same individual can not persistently identified by their parametric relation.
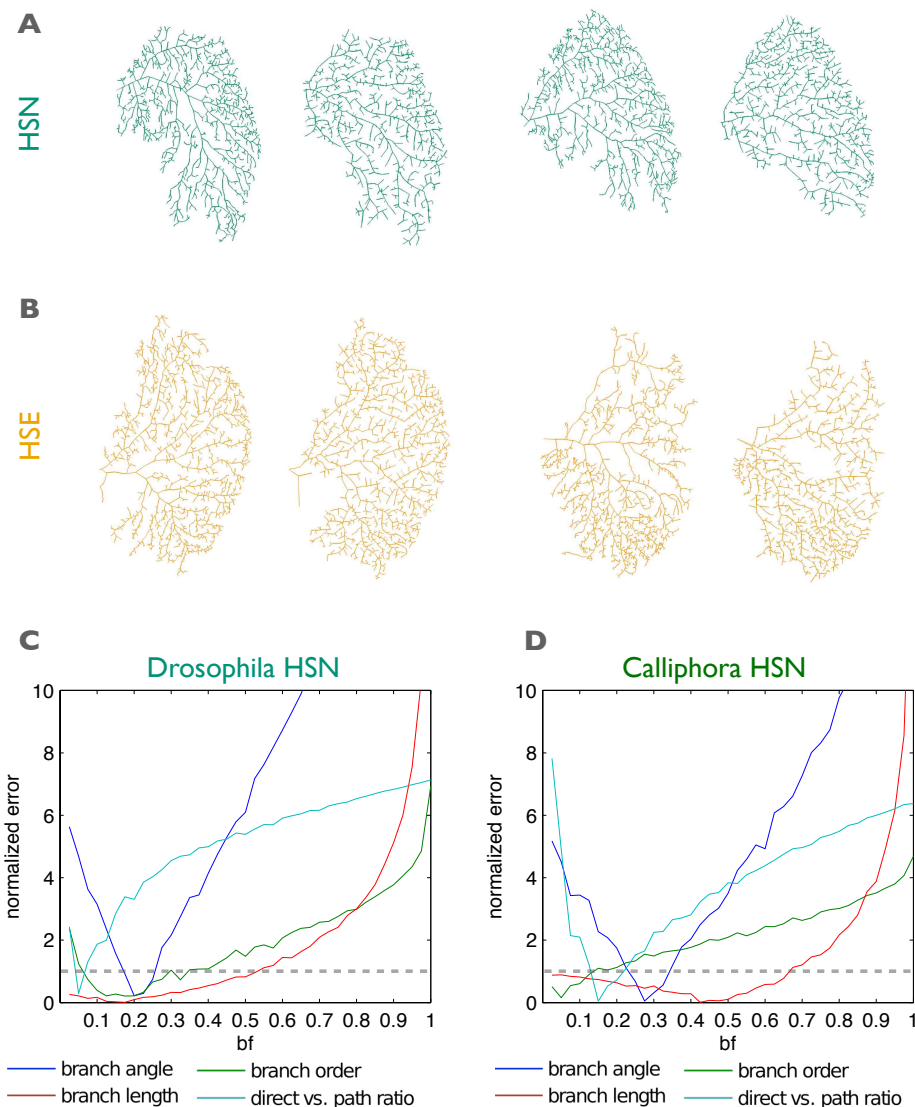
Figure 4.20: Computational synthesis of Drosophila HS cells. (A and B) Real (left) and synthetic cell (right), two examples for each cell type. Synthetic cells were grown into the spanning area of their *in vivo* counterpart using the same branching rule for both HSN and HSE. Comparison of best balancing factor fits in *Drosophila* HSN (C) and *Calliphora* HSN (D), tested for balancing factor ranges from 0.05 to 1. Each cell type in each species was benchmarked individually. For each *in vivo* reconstruction and bf value one artificial cell was created and the branching parameterized. Curves represent mean errors over all cells of one bf normalized by the *in vivo* standard deviation. Values below the gray dotted line (error=1) are within the *in vivo* standard deviation. Compared to *Calliphora*, *Drosophila* shows a more parameter-consistent optimal range between 0.05 and 0.2.
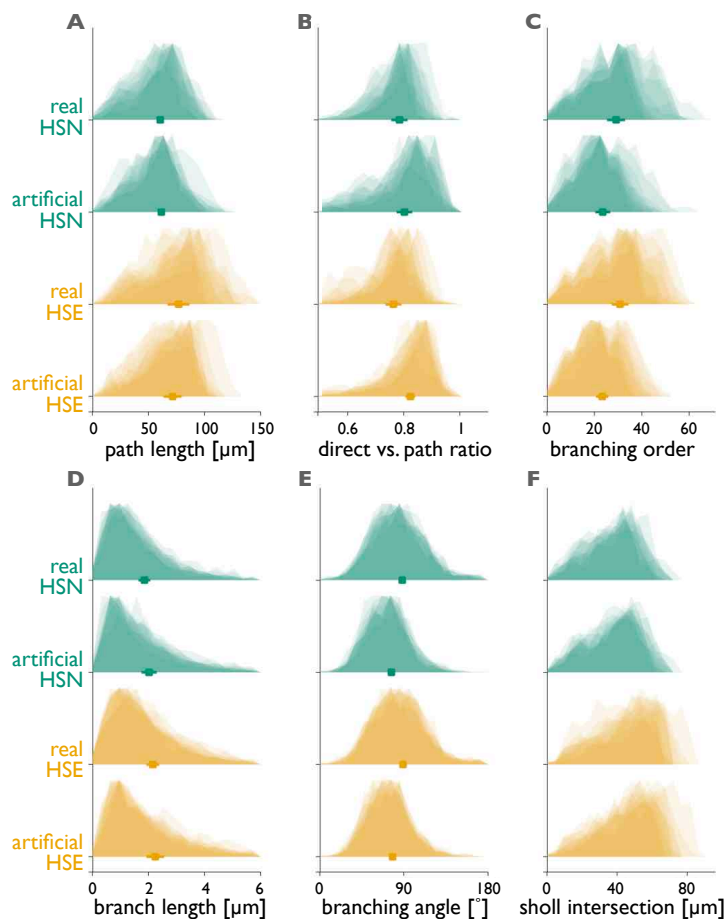
Figure 4.21: Evaluating synthetic branching patterns. (A-F) Synthetic *Drosophila* HS cells (upper two rows) grown with the minimum spanning tree algorithm ($bf{=}0.2$) are able to closely reproduce the *in vivo* branching statistics of the *in vivo* reconstructions (lower two rows). Shapes and mean values look very similar and even small cell specific drifts in path length distributions are conserved.

by a simple optimization rule of neuronal wiring which appears not only to be shared by different cells, but is even conserved through different fly species. While most branching properties are shared, the different scales and complexities represent a clear discriminator between the two HS cells in both fly species. The scaling properties and their functional implications are investigated in the following section.

Fly genetics and preparation as well as image acquisition was performed by Shamprasad Varija Raghu, PhD. The project was structured and supervised with the help of Dr. Hermann Cuntz and Prof. Dr. Alexander Borst. A publication about the quantitative part of this study is in preparation:

F. Forstner, H. Cuntz, B. Schnell, S. V. Raghu, and A. Borst. Functional impact of scaling in identified neurons of the fly. in preparation, 2011

Results of the qualitative analysis have been contributed to:

Processing of horizontal optic flow in three visual interneurons of the *Drosophila* brain. B. Schnell, M. Joesch, F. Forstner, S.V. Raghu, H. Otsuna, K. Ito, A. Borst, D.F. Reiff. J Neurophysiol., 103(3):1646-1657, 2010

4.3 functional implications of LPTC scaling in blow flies and fruit flies

Table 4.2 lists a few measures of *Drosophila*/*Calliphora* scaling. Additionally, for area and volume related measures the one-dimensional scale is given. For example, the mean brain volume in *Drosophila* is 81 times smaller than than in *Calliphora*. Assuming isomorphic scaling in all dimensions, this can be seen as an equal downscaling by a factor of $\sqrt[3]{81} = 4.3$ in the X, Y and Z dimension. The lobula plate area is scaled down by a factor of 20 in *Drosophila*, corresponding to an isomorphic downscaling of $\sqrt[2]{20} = 4.5$ in X and Y. Body length and dendritic diameter on the other hand are already one-dimensional.

morphological scale

Interestingly, most measures appear downscaled by a factor of around 4 in *Drosophila*, suggesting that the whole organism including its functional units is rigidly downscaled. While even the area covered by single neurons like the HSN cell followed this rule, the maximum HSN cell diameter showed a weaker downscaling by a factor of only two. Consequently blowing up a *Drosophila* HSN to the global width of a *Calliphora* HSN led to very thick dendrites - nearly twice as thick as in *Calliphora* (Fig. 4.22). Neither an isometric nor an isoelectrotonic scaling between the HS cells from the two species would therefore be expected (Olsen et al., 1996).

A similar observation can be made in *Drosophila* HSE cells. Here, the diameter is also disproportionally scaled by a factor of only 2. Additionally, the large spanning field expansion of HSE cells in the fruit fly (Fig. 4.13) leads to a lower downscaling ($<$4) of the spanning fields in respect to *Calliphora* HSE cells.

To further investigate the scaling properties, initially, *Calliphora* HSN cells and blown up *Drosophila* HSN cells are compared. This normalization not only allows for pronouncing morphological differences and similarities, but also to compare the electrotonic architecture when applying the same electrotonic model parameters to the cells of both species. Later, a real sized model of *Drosophila* HSN cells will be established, by fitting electrotonic parameters to experimental data.

entity	*Calliphora*	*Drosophila*	scale factor	1D scale factor
mean body length	11 mm	2.6 mm	4.2	4.2
mean brain volume	1.22 mm^3	0.015 mm^3	81.3	4.3
mean LP area	0.18 mm^2	0.009 mm^2	20	4.5
mean spanning area, HSN	0.075 mm^2	0.005 mm^2	15	3.9
mean spanning area, HSE	0.068 mm^2	0.0075 mm^2	9	3
max. dia., HSN	10.87 μm	5.59 μm	1.9	1.9
max. dia., HSE	11.6 μm	5.5 μm	2.1	2.1

Table 4.2: Structure scaling in Drosophila and Calliphora. Fly size measured in three adult flies (also see Fig. 2.4). Brain volumes (n=1) measured by Dr. Christoph Kapfer, unpublished. LP (n=1 in *Calliphora*, n=10 in *Drosophila*) and HSN (n=10) properties measured in reconstructions. 1D scale factors correspond to the quadratic and cubic root of the absolute scale factors for areas and volumes respectively.

diameter scaling

Compared to other neurons, LPTC dendrites exhibit rather large differences in their dendrite thickness. While a dendritic tip in *Calliphora* terminates at around 0.5 μm, the dendritic root grows up to 10 to 12 μm in diameter. Taken the large variance in diameter tapering, the electrotonic properties seem to play an important role, not only in the axonal but also in the dendritic information processing (Haag, 1991; Borst and Haag, 1996; Haag et al., 1997). One would therefore assume the different diameter scaling in *Drosophila* to be dictated by such functional constraints.

Indeed, it was possible to partially explain the biased diameter scaling factor when combining three observations: Firstly, the general branching patterns in both species was quite similar (see section 4.2). Secondly, the diameter of the blown up *Drosophila* HSN cells were around twice as thick as the *Calliphora* HSN cell (table 4.2), while the measured mean terminal diameter were practically identical. Thirdly, considering the most complex reconstructions (by topological point number) *Drosophila* HSN models contained around twice as many dendritic terminals compared to *Calliphora* HSN
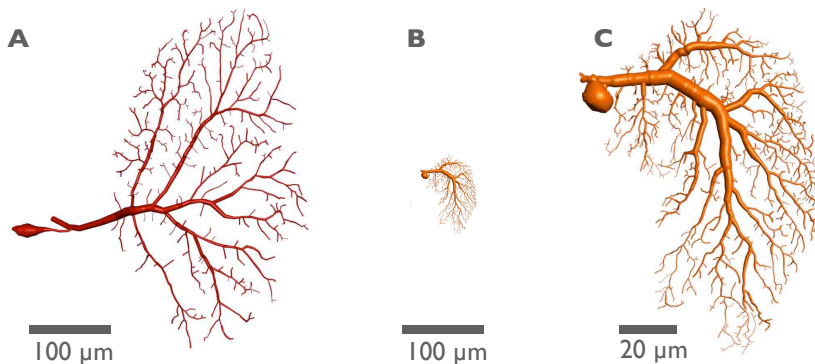
Figure 4.22: Morphological scaling. Comparing *Calliphora* HSN (A) and *Drosophila* HSN (B) at the same scale. (C) *Drosophila* HSN scaled up to the width of a *Calliphora* HSN. The diameter becomes much thicker when proportionally upscaled.

models.

In Figure 4.23A the diameter of every branch point is plotted against the number of all tips terminating from its subtree for both fly species. Assuming synapses being distributed homogeneously over the dendritic tips, this can be seen as an important electrotonic property of synaptic integration. The linear fit indicates a very similar diameter to number of terminals ratio in HSN cells of both species. In Figure 4.23B the same *Drosophila* cell is plotted, but additionally to the overall shape the diameter has been thinned to fit the *Calliphora* HSN cell diameter at the dendritic root. All other branches were scaled with the same factor. The resulting diameter distribution of this hypothetical neuron led to a significantly different ratio. This implies that in HSN cells of *Calliphora* and *Drosophila* a common diameter constraining law is implemented.

Other studies in *Calliphora* (Cuntz et al., 2007a) have proposed a quadratic diameter tapering from the terminal tips to the dendritic root of a neuron. Different optimal parameters for a quadratic decay were thereby precomputed from linear cable models of various lengths. The optimization was based on an optimal current transfer from the beginning to the end of the cable. A quadratic diameter fit for a cylinder reconstruction is then obtained by mapping the path length to the root for each node to the precomputed cables. In Figure 4.23C the original *in-vivo* reconstruction diameter, the terminal derived diameter fit and a quadratic fit are compared for *Calliphora* and *Drosophila* HSN. In *Calliphora*, both methods were able reproduce the *in vivo* diameter quite precisely. In *Drosophila* both approximations did not perfectly reconstruct thicker branches close to the dendritic root. Finer branches and their tapering on the other side matched quite well. This suggests an inherent relationship of the number of upstream terminals, the distance to the dendritic root and the cylinder diameter, that
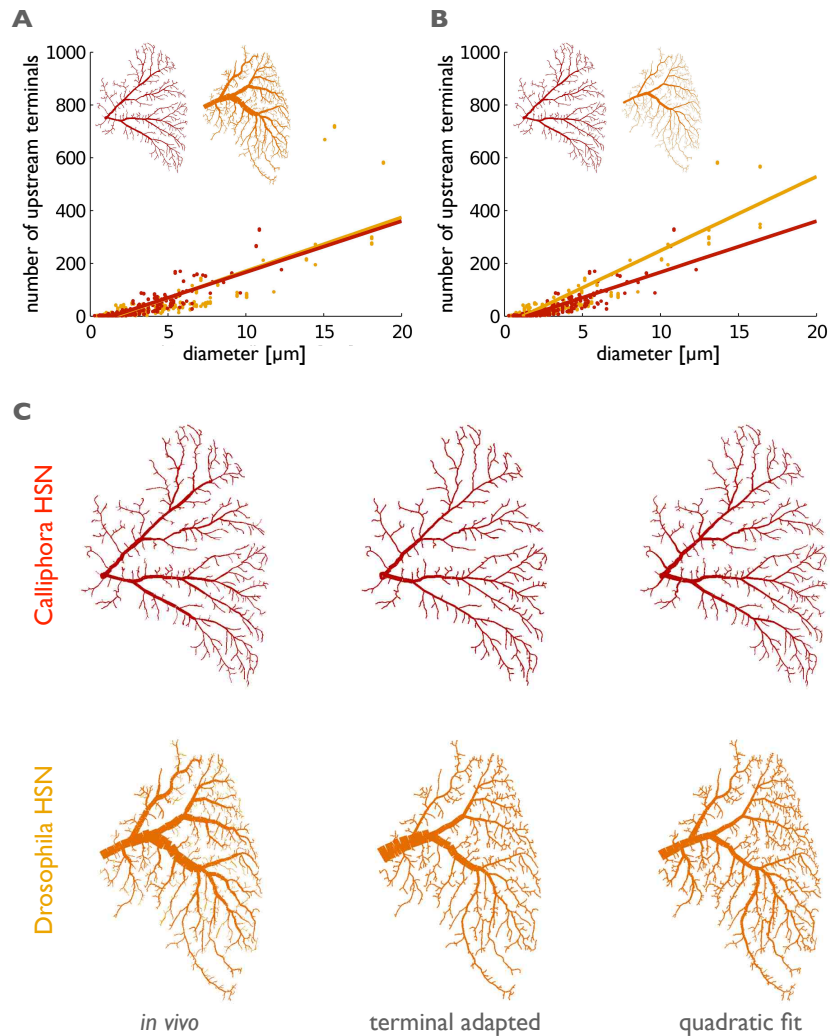
Figure 4.23: Diameter modeling. (A and B) For each branch point of the most complex *Drosophila* (orange) and *Calliphora* (red) reconstruction of the database the diameter is plotted against the number of terminals that lie upstream of that branch point. Lines denote linear fits to these points for both species. Thumbnails show the analyzed *Calliphora* and blown up *Drosophila* cell. (A) An isometrically upscaled *Drosophila* HSN cell shows a very similar terminal/diameter ratio as measured in the *Calliphora* cell. (B) In addition to it's size, the diameter of the *Drosophila* HSN cell is thinned to fit the *Calliphora* cell. The diameter at the dendritic root of the *Calliphora* HS cell is thereby taken as reference. An upscaled *Drosophila* cell with a diameter equalized this way leads to a significantly different diameter to number of upstream terminal ratio than its counterpart with realistic diameter distribution. (C) Visual comparison of diameters from the *in vivo* reconstruction, fitted to the number of terminals and fitted as a quadratic decay from the terminals to the root. In *Calliphora*, both diameter models are able to reproduce the diameter as seen in the *in vivo* reconstruction. In *Drosophila*, thicker dendrites aren't fit perfectly, while smaller dendrites can be reproduced quite realistically.

should be investigated in future studies. Also it might be interesting to compare these results to other relations of diameter tapering like Rall power (Rall, 1959) and Hillman threshold (Hillman, 1988).

Next, a steady state electrotonic analysis was performed on the *Calliphora* HSN dendrite and the blown up *Drosophila* HSN dendrite to characterize the functional implications of the increased diameter. A steady state, passive multi-compartmental electrotonic model was created by homogeneously assigning the axial resistivity R_a and the membrane resistance R_m to each compartment. Parameter values were taken from a previously published electrotonic analysis of *Calliphora* LPTCs (Borst and Haag 1996, $R_a = 40\Omega cm$, $R_m = 2k\Omega cm^2$). Absolute values r_a and r_m per unit length were then calculated individually, considering the radius and length of each compartment (see materials and methods, chapter 3). The conductance matrix and subsequently the compartmental model equation was derived. When using the same electrotonic parameters for size equalized HSN cells from both species and injecting current at the dendritic root, one can see that the dendritic compactness is preserved (Fig. 4.24A). On the other hand, diameter equalized cells show a reduced electrotonic compactness. Next, the opposite direction from terminals located in the middle of the dendritic spanning field to the dendritic root was investigated (Fig. 4.24B). Injections were distributed at the same absolute distance in all neurons and the same current was injected (-0.1 nA). The resulting hyperpolarization at the dendritic root was measured and compared between *Calliphora* HSN reconstruction, upscaled *Drosophila* HSN cell and upscaled, thinned *Drosophila* HSN cell. In the up scaled fruit fly neuron two injections at the same distance were needed to induce a similar hyperpolarization as measured in the blow fly HSN cell. Apparently, the electrotonic 'terminal democracy' is preserved: the doubled diameter and doubled amount of terminals of the blown up *Drosophila* cells halves the electrotonic influence of each individual terminal.

These results imply that - taken the higher complexity - the HSN cell diameters in *Drosophila* are in fact scaled isometrically as all other entities of table 4.2. While results of the previous section implied common branching principles to be applied in both flies species, here I could show that even the electrotonic organization appears conserved. The exact reason for the observed scaling ratio can only be speculated (see discussion section 5), but findings are in line with previously proposed conserved, conceptual implementations of neuronal features in the electrophysiological domain (Marder and Goaillard, 2006; Borst, 2008).

In order to understand the influence of the realistic morphological scaling on the electrotonic properties, a passive compartmental model of a real sized HSN reconstruction was setup and fitted to experimental measurements. The parameter space of the electrotonic model was confined by fitting parameters to a series of sinusoidal current injection experiments. Initially, the model was fitted to step current injection experi-

compartmental modeling
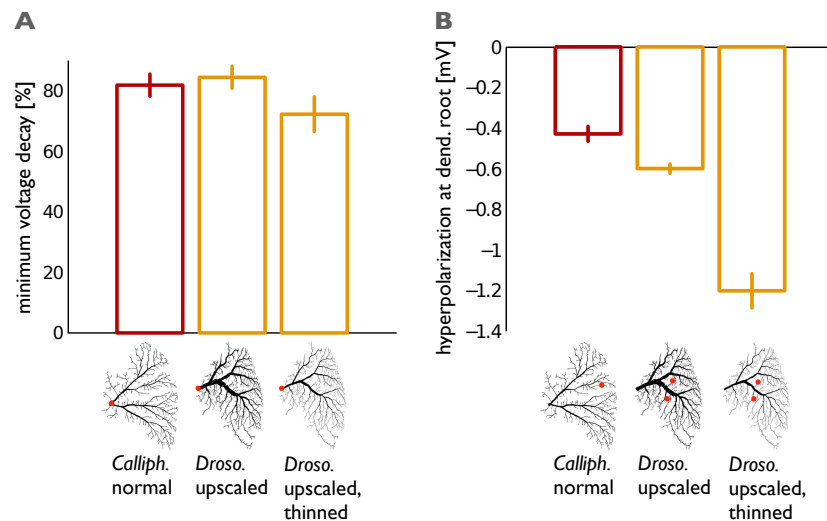
Figure 4.24: Morphological scaling. (A) Current injection simulation into the soma of *Calliphora* HSN, upscaled *Drosophila* HSN and upscaled, diameter-equalized *Drosophila* HSN. Upscaled *Drosophila* cells sustain the electrotonic compactness when modeled with the same electrotonic parameter setup; upscaled, diameter-equalized cells lose a substantial amount of the intitial potential. (B) Current injection into iso-distant terminals (-0.1 nA), one terminal in *Calliphora*, two in *Drosophila* cells. The bar plot shows the depolarization at the dendritic root. 'Terminal democracy' is sustained in the upscaled *Drosophila* cells when considering twice the number of terminals; upscaled, diameter-equalized cells show a larger increase instead. (A and B) Mean and standard deviation over all reconstructed HSN cells of both species.

ments. These yielded quite unstable voltage responses, possibly due to patch clamp specific artifacts of steady current injections and were therefore not considered in this analysis.

The sinusoidal input protocol consisted of a sequential injection of 1, 80, 160, 2, 40, 6, 120, 20, 60, 8, 100 and 4 Hz cosine current inputs with 0.025 nA amplitude, shifted by -0.025 nA. Each frequency pattern was injected for 1 second (except 1 Hz, injected for 2 seconds) and separated by 1 second intervals (protocol adapted from Borst and Haag 1996). Voltage responses were recorded simultaneously. Results were band pass filtered and cosine curves with the corresponding frequencies were fitted to each individual current injection and voltage trace. From these fits the absolute amplitude and relative phase shift of the voltage trace was computed and averaged for each frequency over all individuals. Parameterized responses were now used to benchmark the results of the compartmental model simulations.
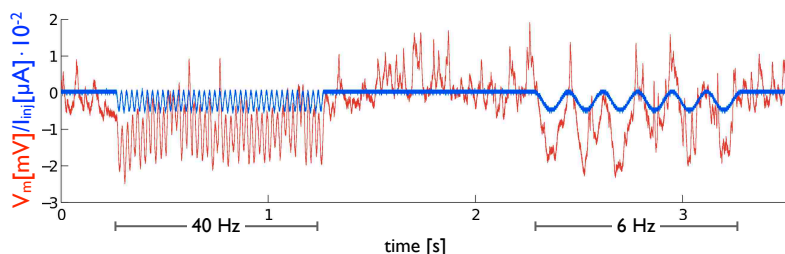
current injection

Figure 4.25: Current injection experiments. Two examples of sinusoidal current injections with current trace (blue): 10 Hz and 40Hz frequency, 0.025 nA amplitude, shifted by -0.025 nA and 1s in duration. The voltage trace (red) reflects the tight correlation of input current and voltage response (experiments performed by Bettina Schnell).
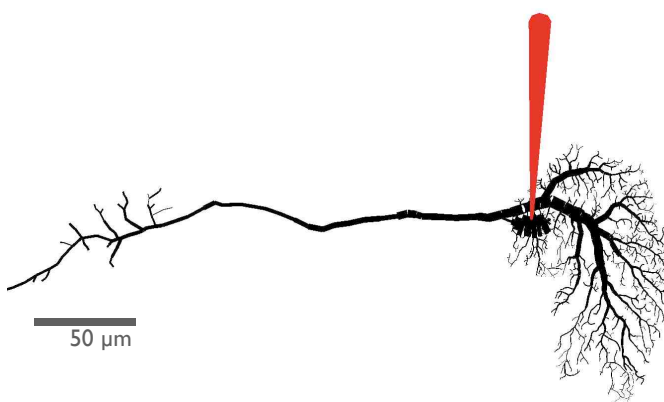
Figure 4.26: Compartmental model. Complete *Drosophila* HSN cell reconstruction. The red cone corresponds to the access site of current injection for *in vivo* experiments and simulations.

simulation

A complete cell including soma, axon and dendrite was reconstructed from a NP0282 stack where a GFP labeled HSN cell was additionally dye injected to follow it's axonal and somatic outgrowth (Fig. 4.26). Active components were not considered in this model. A passive multi-compartmental electrotonic model including the temporal domain was created by homogeneously assigning the specific axial resistivity R_a, the specific membrane resistance R_m and the specific membrane capacitance C_m. r_a, r_m and c_m were then calculated individually, considering the diameter and radius of each compartment (see materials and methods chapter 3)

Sinusoidal current injection simulations were performed according to the *in vivo* protocol: 1, 80, 160, 2, 40, 6, 120, 20, 60, 8, 100 and 4 Hz frequency, 0.025 nA amplitude, shifted by -0.025 nA, 1 second in duration. The conductance matrix and subsequently the compartmental model equation was derived (see materials and methods chapter 3). The simulation time step was set to 0.1 ms. In order to explore the physiological parameter space of the *Drosophila* HSN cell, a parameter scan was initiated with

- R_a ranging from 1 to 1000 Ωcm

- R_m ranging from 1 to 20 $k\Omega cm^2$

- and C_m ranging from 0.1 to 1.2 $\mu F/cm^2$

Amplitude and phase shift of the simulated voltage trace were extracted, compared to the averaged *in vivo* results. The error for each frequency was computed individually and then pooled:

$$E_{A,sim} = \sqrt{\sum_{f \in F} (A_{sim,f} - \overline{A}_{exp,f})^2} \tag{4.1}$$

$$E_{\Theta,sim} = \sqrt{\sum_{f \in F} (\Theta_{sim,f} - \overline{\Theta}_{exp,f})^2} \tag{4.2}$$

With F being the injected input frequencies. Results were then normalized by the standard deviation and combined.

$$E_{A,exp} = \sqrt{\sum_{f \in F} \sigma_{A_{exp,f}}{}^2} \tag{4.3}$$

$$E_{\Theta,exp} = \sqrt{\sum_{f \in F} \sigma_{\Theta_{exp,f}}{}^2} \tag{4.4}$$

$$E_{R_a,R_m,C_m} = 0.5 \left(\frac{E_{A_{m,sim}}}{E_{\Theta_{m,exp}}} + \frac{E_{A_{inj,sim}}}{E_{\Theta_{inj,exp}}} \right) \tag{4.5}$$
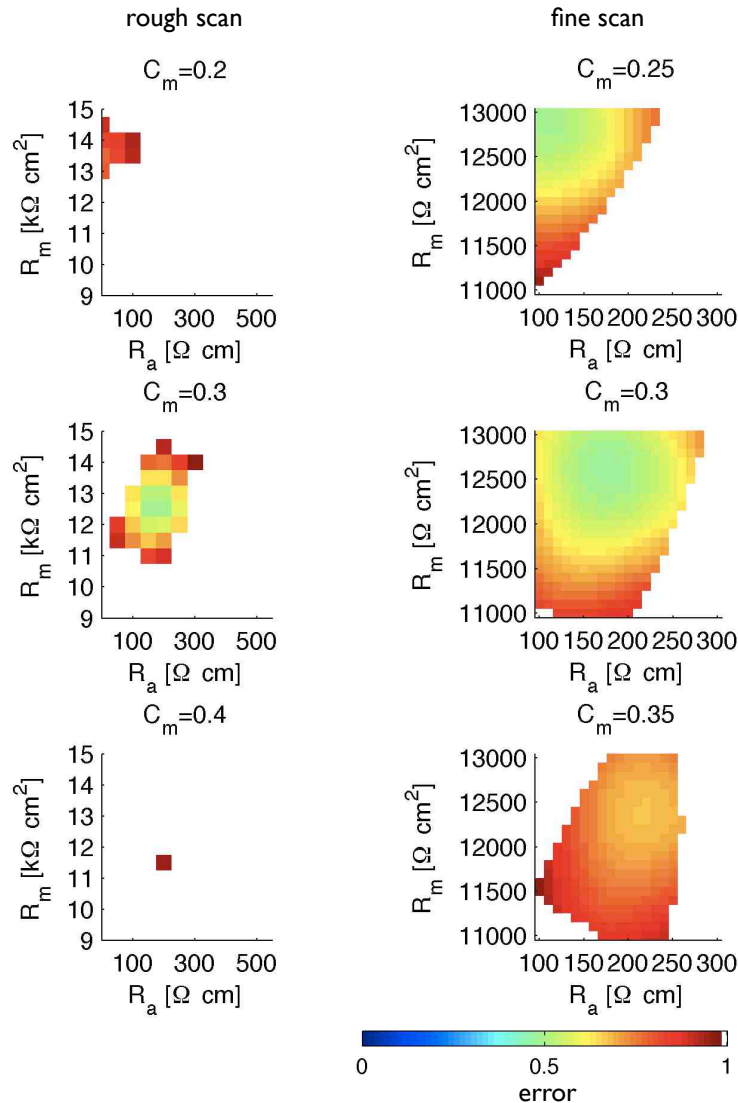
Figure 4.27: Extract of the compartmental simulation parameter scan. Results of the compartmental simulations (see text) for different parameter setups of R_a, R_m and C_m. Each panel corresponds to one fixed value of C_m. X and Y axis denote different values of R_a and R_m. Colors represent error values normalized by the *in vivo* standard deviation. White spots indicate errors larger than the standard deviation. The left column shows results of a rough parameter scan. A broadened minimum at around $C_m = 0.3\mu F/cm^2$, $R_m = 12.5k\Omega cm^2$ and $R_a 170\Omega cm$ can be observed. The right column represents a finer scan within the minimum error value cloud found during the roug scan. Combinations outside of the plotted range but within the here analyzed range $\left(R_a\text{:1 to 1000 } \Omega cm,\ R_m\text{:1 to 20 } k\Omega cm^2,\ C_m\text{: 0.1 to 1.2 } \mu F/cm^2\right)$ did not yield error values within the *in vivo* measured standard deviation.

Error function values below 1 were considered to be a reasonable fit, since in the range of *in vivo* measured variability. Figure 4.27 shows the results of the parameter scan. A local minimum can be found at $C_m = 0.3\mu F/cm^2$, $R_m = 12.5k\Omega cm^2$ and $R_a 170\Omega cm$. This parameter setup performed quite well in reproducing the amplitude (Fig. 4.28A) and phase shift of the *in vivo* recordings.

Does this represent a biologically reasonable parameter setup? C_m has traditionally been fixed to values of $1\mu F/cm^2$ (Gentet et al., 2000). Therefor, a value of $0.3\mu F/cm^2$ appears quite low. On the other hand the membrane capacitance has never been measured directly in cells of this size and morphological character. R_m does conform with previous studies in *Drosophila* (Gouwens and Wilson, 2009). R_a is very variable in our analysis. This might be an artifact of the used fitting constraints. R_a is experimentally only constrained by R_{inj}. Injecting and measuring at the same compartment might represent a quite weak method to adequately constrain R_a as different values only moderately affect the R_{inj} of the compartmental model. Instead the current transfer to a more distant location in the dendrite could represent stronger constraint, but so far, *Drosophila*'s size has limited injection experiments to the soma compartment.

Table 4.3 depicts different parameters from a previously published electrotonic analysis of *Calliphora* LPTCs (Borst and Haag, 1996) and the results of the analysis performed on *Drosophila* cells. Values vary quite strongly. On the other hand it becomes obvious why such low values of C_m were obtained for *Drosophila*: R_{inj} is around 20 times larger in *Drosophila*, while the measured time constant (estimated by $\tau_m = C_m R_m$) reaches similar values as in *Calliphora*. As noted before, R_a has only moderate influence on R_{inj} of the compartmental model and thus R_m has to compensate alone. Altering R_m and keeping τ_m fixed implies a reduction of C_m. This way the intrinsic logic of the parameter values validate the identified parameter setup. Interestingly the square rooted ratio of R_m and R_a as used for the calculation of the length constant $\lambda = \sqrt{\frac{r}{2}}\sqrt{\frac{R_m}{R_a}}$ (with the radius r) is similar in both species.

Parameter [unit]	*Calliphora* HSN	*Drosophila* HSN
R_{in} $[M\Omega]$	5	190
R_a $[\Omega cm]$	40	170
R_m $[k\Omega cm^2]$	2	12.5
C_m $[\mu F/cm^2]$	0.9	0.3
τ_m $[ms]$	2.1	3.75
$\sqrt{\frac{R_m}{R_a}}$ $[\sqrt{cm}]$	7	8.6

Table 4.3: Passive simulation parameters of blow fly and fruit fly HSN. *Calliphora* parameter values from Borst and Haag 1996.

While the somata in both blow fly and fruit fly HSN cells were anatomically secluded   *compactness*
compartments, simulations showed that current can spread freely into the axon: The
differences in input resistance measured in the axon the soma appeared to be rather
marginal with differences of 20% in *Calliphora* and 10% in *Drosophila*. Injections into
the pruned soma led to a large increase in input resistance by a factor of 20 in HS cells
of both species. Furthermore, Figure 4.28B depicts a current injection simulation into
the soma of a *Drosophila* HSN cell. In accordance with *Calliphora* HS cells (Borst and
Haag, 1996), the current can spread easily and penetrate the complete neuron. These
results also show that the *in vivo* recordings performed in somata of *Drosophila* are
adequate for estimating the overall electrotonic properties, assuming homogeneously
distributed parameters.
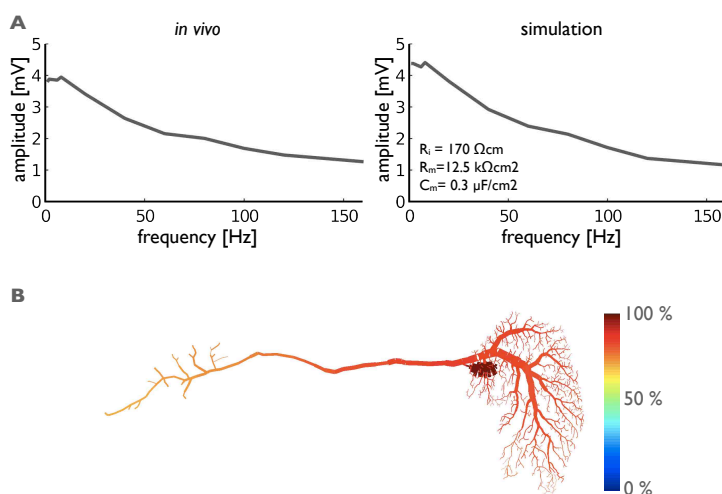
Figure 4.28: Amplitude spectrum and electrotonic compactness. (A) Response amplitude
spectrum of *in vivo* recordings and simulation (see box for parameter setup). (B) Simulated input
of a 0.1 nA current injection into the soma of a *Drosophila* HSN cell. The steady state voltage
decay is mapped as color code on to the cylinders. Current is able to freely flow into the dendrite
and axon.

In this study the functional implications of LPTC scaling was investigated. Most   *conclusion*
entities in *Drosophila* were downscaled by a factor of four. The relative diameter in
fruit fly cells turned out to be significantly larger than their blow fly counterparts. It
was possible to explain this with a conservation of the overall electrotonic architecture
of the cells. An electrotonic analysis revealed different membrane parameters in blow
fly and fruit fly.

Current injection experiments and cell fillings were performed by Bettina Schnell. The
project was supervised by Dr. Hermann Cuntz and Prof. Dr. Alexander Borst. A
manuscript is in preparation:

F. Forstner, H. Cuntz, B. Schnell, S. V. Raghu, and A. Borst. Functional impact of scaling in identified neurons of the fly. in preparation, 2011

4.4 impact of Dscams onto LPTC morphology and function

Dscam genes have been convincingly attributed to the control of dendritic targeting and branching in *Drosophila* (Chen et al., 2006; Schmucker et al., 2000; Hughes et al., 2007; Hummel et al., 2003; Zhu et al., 2006; Wang et al., 2004; Zhan et al., 2004). However, no study investigated this observation quantitatively nor did anyone analyze functional implications of *Dscam* manipulations. In this respect, LPTCs represented a perfect system to further investigate *Dscam*'s influence on the morphological and electrophysiological properties. Their conserved location, shape and functionality throughout individuals should allow easy identification and quantification of *Dscam* induced alterations. HSE and HSN cells were selected as targets. HS cells were previously investigated in depth (see section 4.2) and represented a reliably identifiable system of three cells. Wild type HS cells show no overlap of sister branches and spread quite homogeneously into their lobula plate location. Between cells, no fasciculation but a large overlap of spanning area was observable - all effects that have been shown to be Dscam protein mediated in other systems. In addition, HS cell specific driver lines existed and allowed a cell targeted *Dscam* profile manipulation (see details in the materials and methods chapter 3).

expression experiments   Dscams have been shown to be responsible for tiling behavior in neurons (Hattori et al., 2008). The huge overlap of the HSN and HSE cell in *Drosophila* (see also Fig. 4.13) and their close proximity in the anteroposterior axis raised the question whether an overexpression of the same Dscam isoform could lead to heteroneural repulsion and subsequent tiling behavior in these neurons. The two-dimensional extension should allow clear identification of these effects. Hence, a single Dscam isoform (11.31.25.1) was over-expressed in LPTCs in addition to the endogenously expressed Dscam repertoire. 11.31.25.1 was chosen from a small collection of different UAS-*Dscam* constructs because its overexpression caused a reproducible dendritic phenotype in LPTCs. As depicted in Figure 4.29 ectopic expression of Dscam 11.31.25.1 caused severe defects in the elaboration of HS dendrites. The example shows a NP0282 driven overexpression of *Dscam* 11.31.25.1 in HSN and HSE as confocal stack Z-projection and cylinder reconstruction. While HSN remains largely unaltered, the HSE cell lost large parts of its lateral branching pattern compared to the control case.

DB331 driver line   Unfortunately, the NP0282 line did not generate stable phenotypes over a larger pop-
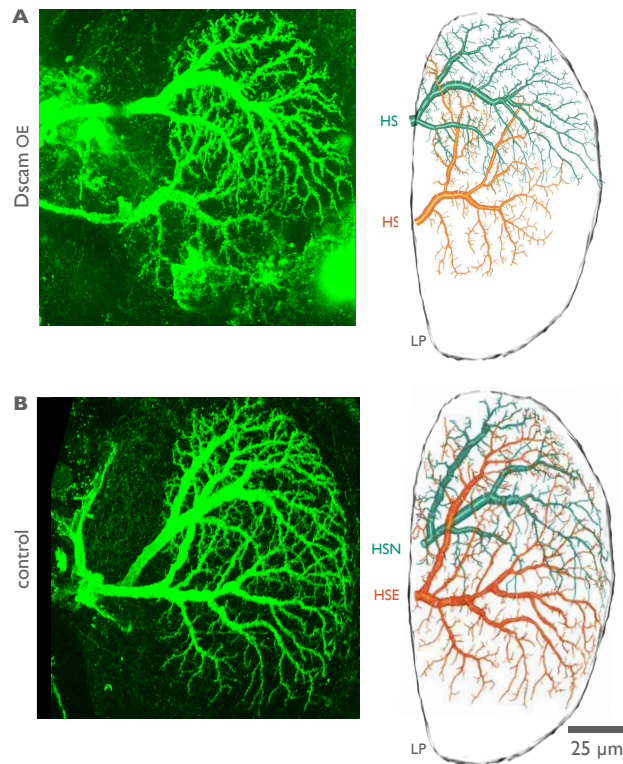
Figure 4.29: Control and Dscam HS cells. (A) Dscam over-expession NP0282-GFP line, confocal microscopy image (left) and cylinder reconstruction (right). (B) Control NP0282-GFP line, confocal image (left) and corresponding cylinder reconstruction (right). LP sketched and fitted from other images stacks containing background staining. The spanning area of the HSE cell appears much reduced in the *Dscam* mutant, especially the lateral branches contacting the lobula plate are largely missing (image acquisition performed by Jing Shi and Shamprasad Varija Raghu, PhD).

ulation of flies possibly due to its weak expression pattern. In order to see consistent effects, a stronger driver line was introduced. The DB331 line had shown to be a such a line and was therefore chosen as replacement (Joesch et al., 2008). However, DB331 co-labeled VS cells and finer branches e.g. in the dorsal LP area that could not be resolved consistently due to the large overlap and the background illumination (Fig. 4.30B). Analysis was therefore limited to the area covered by the dendrites. Thicker, easily attributable branches were followed from the root to the dendritic tips until the dendritic coverage was faithfully sampled (Fig. 4.30B). Background stains allowed reconstruction of the lobula plate volume, facilitating faithful registration and normalization of the cell reconstructions. Dscam alterations driven by DB331 appeared not only more consistently but with even stronger phenotypes than in NP0282 (Fig. 4.30A). HSN and HSE both lost large parts of their spanning area.
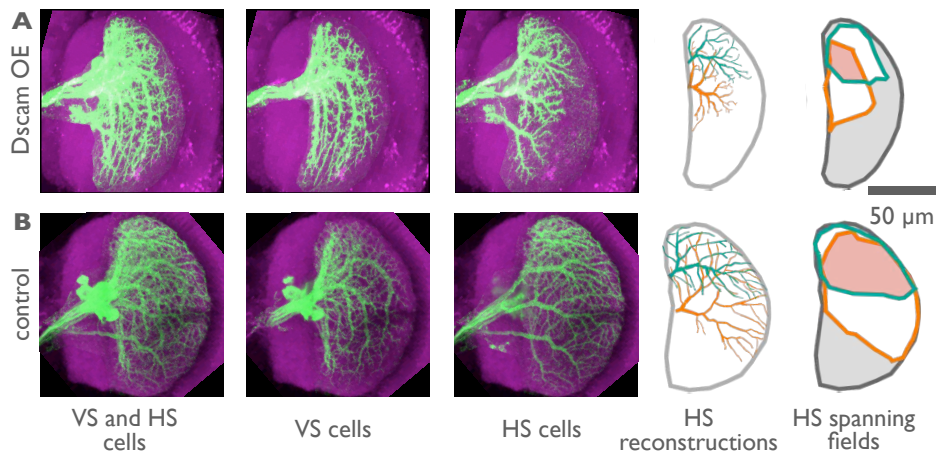
Figure 4.30: DB331 driver line. Control (A) and *Dscam* overexpression (B) stacks based on the DB331 line. DB331 targets both HS and VS cells in the lobula plate. The distance in the anterior-posterior dimension allowed the separation into VS (second column) and HS cells (third column). The HS cells could then be reconstructed (fourth column, HSN: turquoise, HSE: orange) and the spanning fields calculated (last column). DB331 allows stronger expression patterns and *Dscam* overexpression phenotypes appeared more pronounced and consistent (image acquisition by Jing Shi).

database   In order to quantify initial observations, a total number of 16 HSN and HSE cells from 16 different animals were reconstructed to capture the spanning fields of the cells (Fig. 4.31A and B, middle column). Reconstructions were normalized by the height of their lobula plate, outlines and overlaps were digitally sketched (Fig. 4.31A and B, left and right columns). In comparison to the control cells (Fig. 4.31B) a consistent and strong reduction in spanning field area and inter-cellular overlap in *Dscam* overexpressing cells became visible (Fig. 4.31B). Lobula plate outlines established a valuable context and supported these observations. Exceptions with normal or partly normal

spanning fields also occurred once (Fig. 4.31A, last row, right HSE/HSN). Additional screens confirmed that the observable difference in LP shape and size (Fig. 4.31) was independent of Dscam profile manipulations but rather related to the different ages of the flies. This did not affect the significance of the findings since for both conditions a similar range of ages were pooled and in all cases the flies were adult, functionally fully developed and all measures were normalized for the size differences.
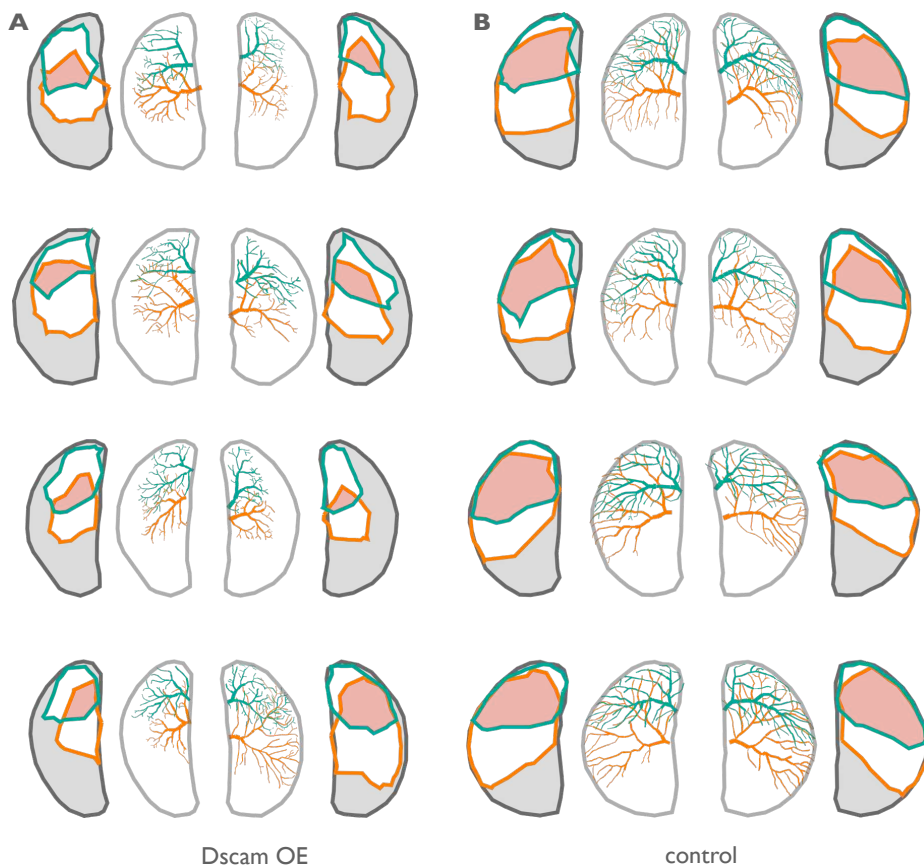
Dscam OE   control

Figure 4.31: DB331 Dscam overexpression database. Normalized HSE/HSN/LP reconstructions and spanning fields from 8 different DB331 *Dscam* overexpressing (A) and 8 different DB331 control flies (B). Turquoise colors correspond to HSN, orange colors to HSE. The grey border represents the reconstructed lobula plate. In the spanning field graphs the grey area labels the uncovered LP area, the red area the intersection area of HSE and HSN. Most *Dscam* overexpressing cells are reduced in overall cell size and do not reach the lateral border of the lobula plate anymore (reconstructions based on images acquired by Jing Shi).

The visual observations were quantified in Figure 4.32. Indeed, the area covered by the dendrites was strongly reduced. In average, HSN and HSE lost nearly half of their spanning area within the lobula plate. The average dendritic overlap of the two cells

quantification

was reduced to a third of the original value. Still, a perfect tiling as expected from the resulting repulsion of HSN and HSE cells could not be observed.
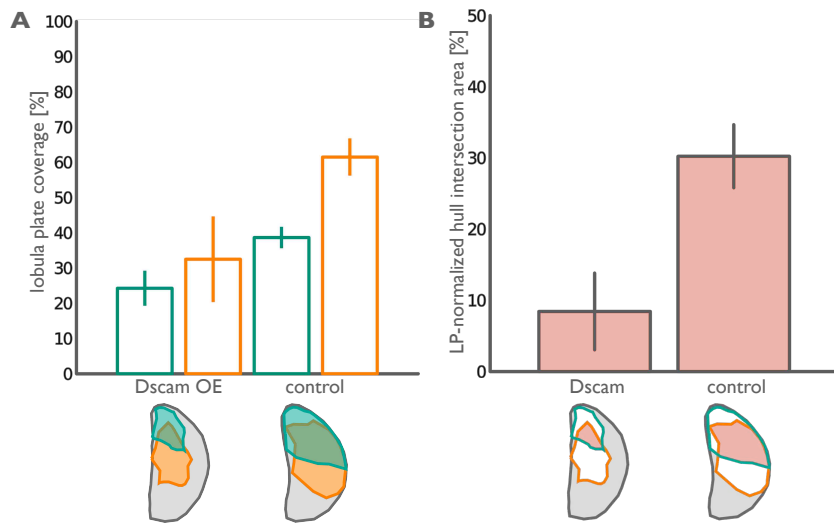
Figure 4.32: Dscam statistics. (A) Mean and standard deviation of the lobula plate coverage for *Dscam* overexpressing vs. control flies. A large reduction in coverage was observed. (B) The intersection area between HSN and HSE, normalized by the LP area. The overlap of the two cells was largely reduced in *Dscam* overexpressing animals.

mapping receptive fields

Based on this phenotype and the topographic arrangement of the lobula plate input is was predicted that motion stimuli in the lateral field of view (corresponding to the medial lobula plate) should still be processed normally whereas motion in the frontal field of view (corresponding to the lateral lobula plate) should be impaired. The following experiments were performed by Bettina Schnell: The receptive fields of HS cells were mapped by small, moving bars (6 deg elevation and 1.4 deg width) for each positions of a LED display used to stimulate the fly. Control HS and Dscam HS cells depolarized when the bar moved right (PD, preferred direction) and hyperpolarized when the bar moved left (ND, null direction) with respect to the right eye. The ND response was subtracted from the PD response and stored for each position of the field of view of the fly (Fig. 4.33A). This protocol was repeated for several cells of each type (HSN, HSE) in both genotypes.

changes in the receptive field

According to the position of their dendrite in the equatorial area of the lobula plate, HSN/HSE cells were most sensitive to horizontal motion in the northern/equatorial field of view in both genotypes (Fig. 4.33A and B). However, control HS cells had much broader receptive fields compared to Dscam HS cells. Responses to motion presented to the frontal area were strongly reduced in Dscam HS cells. A more detailed description of the changes in these receptive fields of HSN and HSE induced by *Dscam*
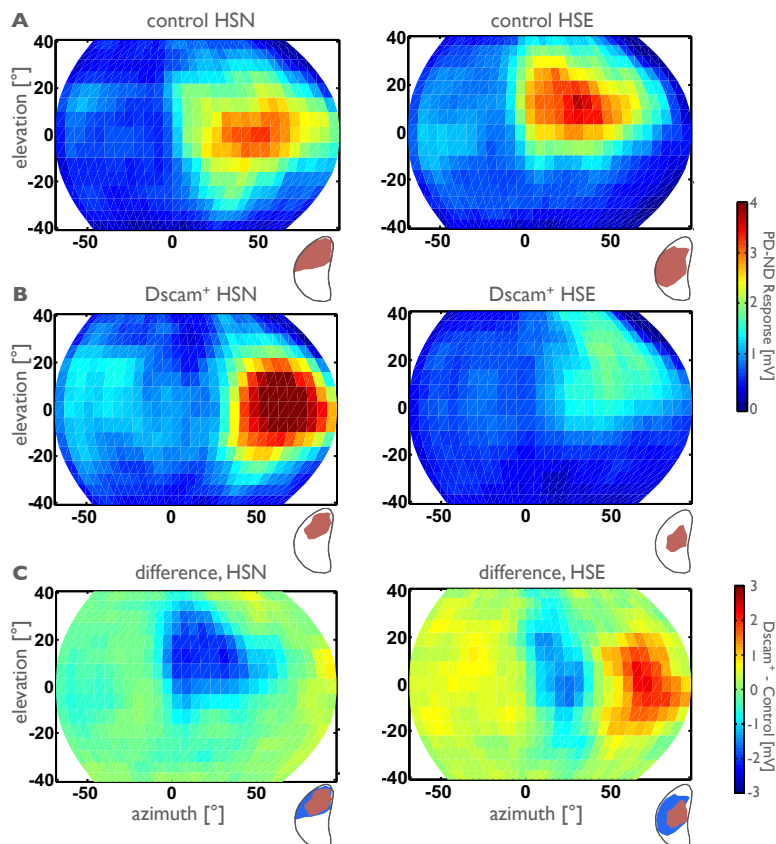
Figure 4.33: Changes in receptive field properties. (A and B) Receptive fields of control and *Dscam* overexpressing HS cells. PD minus ND responses elicited by a small, horizontally moving bar at different positions in the field of view are depicted in false colors. Thumbnails exemplify the morphological spanning fields of the plotted cells and the lobula plate silhouette. (A) Control HS cells have large receptive fields extending the whole stimulated area on the ipsilateral side, including the frontal field of view. (B) Overexpression of *Dscam* causes a strong reduction in sensitivity or complete motion blindness in the frontal area (ipsilateral side, from frontal 0° to lateral 20° in HSN, from frontal 0° to lateral 30-40° in HSE) corresponding well to the absence of dendritic branches in the corresponding lateral area of the lobula plate (thumbnail and Fig. 4.31). The absolute response amplitudes of *Dscam* overexpressing HS cells are increased at more lateral positions and on the contralateral side compared to control HS cells. (C) Differences in the receptive field of control and *Dscam* overexpressing HS cells displayed as false color coded contour plots. The differences between the local mean response amplitudes (mV) are visualized by subtracting the receptive fields of control HS cells (A) from the ones of *Dscam* (B) overexpressing HS cells. HSN and HSE exhibit strongly reduced sensitivity in the frontal area of the ipsilateral field of view (blue/green, between 0° and 50° along the azimuth). This deficit corresponds well to the lack of dendritic branches in the lateral lobula plate. In addition, HSE exhibits increased response amplitudes at more lateral positions and on the contralateral side (experiments and data analysis performed by Bettina Schnell)

11.31.25.1 overexpression was provided by subtracting the receptive field of control HS cells from the one of Dscam HS cells (Fig. 4.33C). Plotting the difference in the absolute response amplitude for HSN (Fig. 4.33C, left) and HSE (Fig. 4.33C, right) provided a visualization of the exhibited reduction in motion responses in the frontal field of view (blue/green).

conclusions   In this analysis we investigated the influence of the Dscam protein onto the wiring process of LPTCs. One Dscam isoform was overexpressed using a driver line targeting a subgroup LPTCs (DB331). It was expected that repulsion of same Dscam proteins would lead to clear tiling behavior. Initial results yielded a dramatic reduction of spanning field area in these cells. Although intercellular overlap of cells was reduced, tiling behavior was not induced. Dscam HS cells lost part of their receptive field sensitivity in accordance with their morphological degeneration. The analysis represents a novel approach in LPTC research and an initial attempt to establish a new model system to study Dscams on the level of morphology, function and behavior.

Fly genetics, preparation and image recording were performed by Jing Shi. Electrophysiological experiments were all done by Bettina Schnell. The project was supervised by Dr. Dierk Reiff and Prof. Dr. Alexander Borst. A manuscript is in preparation:

J. Shi, B. Schnell, V. Haikala, F. Forstner, H. He, M.-L. Erfurth, D. Schmucker, A. Borst, and D. F. Reiff. Dscams control dendritic shape and motion processing and are behaviorally relevant in *Drosophila*. in preparation, 2011

5 discussion

In this thesis I have studied the morphological properties of LPTCs in the fly. First, investigated four individually identifiable blow fly LPTCs. I could show that the inherent difference between the individual cells came from the different areas in which they specifically span their dendrites. The inner branching structure was similar throughout all cells.

Secondly, I compared the anatomy of two of these cells with corresponding cells of the fruit fly, which is downscaled by a factor of four. Instead of exhibiting a less complex branching pattern as expected from the lower sensory resolution in the fruit fly, the branching structures were more complex. Also, the maximum diameters in *Drosophila* were much thicker when considering the overall downscaling. As in *Calliphora* LPTCs, the morphological identity of *Drosophila* cells seemed to be based on their spanning field characteristics alone. The observed branching structure could be explained and synthesized by a simple branching rule constrained by the spanning field. *Drosophila* cells from the same individual and cells from different individuals showed the same degree of variability in branching structure and spanning field properties.

Thirdly, I studied the functional consequence of the large scaling differences of LPTCs between fruit fly and blow fly. The large diameters of the fruit fly cells were found to electronically compensate for the increased number of potential inputs and conserve the electrotonic compactness of the cells. The passive electrotonic parameters largely differed in LPTCs in blow fly and fruit fly.

Fourthly, I studied the effect of manipulations on the Dscam protein profiles in LPTCs to see in which way it affects the dendritic outgrowth and response properties. Dscam led to strongly reduced dendrite spanning fields with less overlap between individual cells.

morphological analysis

Due to their particular constancy of form and function, LPTCs are an ideal subject for studying neuronal morphology. LPTCs can be easily identified by their topographic location, morphology and response properties. The projects described in this thesis shed light on the morphological constraints leading to this constancy.

While cells were easily identified by their global appearance, the intrinsic branching structure appeared to be quite variable from individual to individual. This observation of highly variable branching patterns within the same identified cell types are in line with previously published qualitative studies on LPTCs (Hausen, 1982). Similar observations have also been made in identified cells of isogenic grasshoppers, where the branching behavior even in genetically identical individuals was found to differ substantially (Goodman, 1978).

The database of reconstructed cells and the quantitative rather than qualitative ap-

proach allowed us to reveal the underlying principles of these observations in the fly. The presented results imply that the branching pattern in all cells analyzed in this study - in *Drosophila* as well as in *Calliphora* - is merely a result of the same branching rule, common to all cells. The key to their individual morphological identity lies in their dendritic spanning fields. This conclusion is supported by the presented spanning field and branching statistics and eventually by the application of a growth algorithm, capable of faithfully synthesizing LPTC morphologies. This solution not only provided evidence for the general applicability of this growth algorithm to all LPTCs, but led to the question whether these principles might be inherent to many others if not all neurons.

The quality of our results was largely dependent on the labeling technique and the manual reconstruction method. *Calliphora* cells had to be filled and it was not clear whether the labeling agent was able to diffuse into the small dendrites. This could explain the observable difference in terminal numbers between blowflies and fruit flies for which the cells were genetically labeled. We therefore applied the same Alexa labeling protocol used in *Calliphora* cells in *Drosophila* cells. Here, image recordings yielded complete stains, even in small dendrites of *Drosophila* when comparing genetically expressed GFP and injected Alexa color channels. This validated our labeling method for the larger *Calliphora* cells. Still, smaller labeling molecules like Neurobiotin (Huang et al., 1992) should be used to further investigate this issue. In *Drosophila*, complete labeling could be assumed, but available driver lines didn't resolve individual cells which complicated the reconstruction process. Future, more specific driver lines will most probably solve this issue.

At the beginning of this project only a few reconstruction systems were available with the commercial system Neurolucida being the most widely in use (Glaser and Glaser, 1990). I decided to develop my own system, taking advantage of the primarily planar outgrowth of LPTCs. This allowed me to adapt the semi-automatic algorithm and user interface to the current data set and hence, to accelerate the reconstruction procedure. In the meantime, other reconstruction systems have emerged that could potentially outperform my software, especially in 3D (Evers et al., 2005; Myatt and Nasuto, 2008; Cuntz et al., 2010). Some systems even advertise fully automatic reconstruction (Uehara et al., 2004; Yamasaki et al., 2006; Peng et al., 2010). Automatic reconstructions have been the aim for decades (Macagno et al., 1979; Capowski, 1983), though, with limited practical success. Clearly, a universal, fully automatic reconstruction system would largely widen our view on neuronal morphology. A recent challenge for the best fully automatic reconstruction system will reflect the current state of development in this field (Mann, 2010).

synthetic algorithm

In electrophysiology, the process of reproducing experimental data with a theoretical model allows one to condense a complex biophysical system to its functional essence. It represents a critical step in truly understanding the underlying functional principles of a neuron by synthesizing its experimentally observed behavior. In anatomical neuroscience such a model could represent a powerful tool e.g. to verify previous morphological classifications, to understand rules of dendritic growth (Ascoli, 2002) or to create network simulations with populations of synthetic neurons (Markram, 2006).

Here, such a model was used to confirm the critical impact of the spanning field properties on the identity of the LPTCs. The applied, previously proposed branching rule (Cuntz et al., 2007a) is based on a minimum spanning tree algorithm that is grown into the spanning fields of cell reconstructions. The algorithm requires three constraints: First, realistic target points have to be defined, that the algorithm then connects in an iterative fashion. These target points are derived from original branch and termination points in the cell reconstruction. To introduce branching variability but conserve local features of the cells, random point seeds are generated based on local densities of branch and termination points. As a second constraint the origin of the synthetic dendrite has to be defined. Different starting points for the algorithm can lead to different morphologies. The third parameter, the so called 'balancing factor', defines the behavior of the minimum spanning tree algorithm. The branching rule tries to optimize the overall length and the path length to the root of each point. A balancing factor sets the weights of these two costs when connecting points. Results show that the algorithm is capable to faithfully reproduce LPTCs visually and statistically. Initial attempts to synthesize LPTCs with branching rules that do not consider the spanning field extension and target points did not produce visually acceptable results (Forstner, 2005). Still, it will be interesting to see how other algorithms perform in comparison to the minimum spanning tree algorithm.

The generation of adequate target points was critical for the success of the algorithm. Depending on the point of view, target points can be chosen in different ways. In procedural algorithms e.g. Lindenmeyer based systems like LNeuron (Ascoli et al., 2001) all rules of neuronal outgrowth are cell intrinsically encoded. In each iteration branching or elongation of an existing branch is decided according to a predefined rule set. Parameters of this rule set like mean branch angle, branch length and branch order are adjusted according to morphological statistics of cell reconstructions. Modeling of parameter distributions and randomness introduce variability into the resulting fractal like structures. Compared to such a defined rule set, the choice of target points for the minimum spanning tree algorithm represents quite a strong constraint. On the other hand, one could consider modeling the large number of known growth factors

influencing molecular mechanisms (Corty et al., 2009), from Dscam mediated neurite interactions, molecular cues in the extracellular domain to cell intrinsic actin dynamics in the growth cone of spreading dendrites. In this respect, the branching rule and its constraints is a comparably simple and compact representation of the branched structures. As is the case for electrophysiological simulations, the model should be chosen individually to fit its needs (Herz et al., 2006). Hence, the algorithm might be a good compromise between constraints and insights obtained as a result.

Nonetheless, our results clearly suggest that the particular cost function is biologically implemented. In fact the algorithm resembles those fundamental growth principles, stated more than 100 years ago by Ramón y Cajal. In Cajal's own view neuronal structure followed three principles when branching out: it conserves space, cytoplasm and conduction time (y Cajal, 1995). The latter two are objectives of the cost function implemented in the minimum spanning tree algorithm. Computational processing power and large data driven approaches allowed us to validate Cajal's theories in LPTCs. A recently published article confirms that this claim is not limited to cells with topographically arranged inputs like LPTCs, but instead applies to a wide range of neurons in other species (Cuntz et al., 2010).

The simplified and reduced nature of the cost function of the algorithm also defines its shortcomings to reproduce more complex features as can be exemplified by the VS cell synthesis. Although the general appearance of the cells can be synthesized, features like the dominant, T-shaped dendrites with other neurites primarily branching to the lateral LP border cannot be reproduced faithfully. In fact, different domains and subregions might follow different balancing factors. The algorithm might therefore be seen as a predominant principle or backbone model that is subject to further morphological influences like neurotrophic gradients, continuous growth, space limitations, synaptic input and cell competition. All these effects can be modeled on top of the general conservation of space and cytoplasm. The ongoing exploration of the molecular principles of neuronal branching might unravel the genetical program for neuronal growth. It will be interesting to see if and how organisms encode Cajal's morphological growth constraints.

scaling properties

The last decade of brain research in the fruit fly has revealed strong similarities between *Calliphora* and *Drosophila* (Fischbach and Heisenberg, 1984; Scott et al., 2002; Schnell et al., 2010; Joesch et al., 2008). It is possible to take advantage of studies spanning both species in order to unravel the common feature space of neuronal wiring (Borst et al., 2010). The obvious difference in size of the two flies raises the question to which extent networks and their architecture have to be modified to completely compensate for differences in their spatial dimensions.

I could show at the example of HS cells that *Drosophila* LPTCs follow the same branching principles as *Calliphora* LPTCs and that even the electrotonic architecture is maintained. However, the morphology of *Drosophila* HS cells is not downscaled in an isoelectrotonic manner, which would imply a quadratic relation of diameter scaling (Olsen et al., 1996). Instead, I observed the diameter to be scaled down by a lesser extend compared to the overall cell scaling. As I could demonstrate, this disproportional scaling of the branching diameter can be attributed to the conservation of electrotonic compactness and synaptic integration properties, when considering the increased number of dendritic tips, as potential carriers of synaptic sides. Other studies have shown the impact of the electrotonic architecture and it's optimization to execute individual tasks (Egelhaaf et al., 1994; Mainen and Sejnowski, 1996; London and Häusser, 2005).

The complexity of *Drosophila*'s HS cells is a mystery itself. The lower spatial resolution of the fruit fly visual system with roughly 700 ommatidia per eye (Götz, 1968) vs. 4500 in Calliphora (Sukontason et al., 2008) would suggest a lower number of terminals instead. The increased complexity could be a compensatory effect for replacing other neurons e.g. the CH cells which so far have not been discovered in *Drosophila*. In this respect, electron microscope based high resolution serial block face scanning (Denk and Horstmann, 2004; Mishchenko et al., 2010) and differential whole brain fluorescent molecule expression techniques (Livet et al., 2007) represent methods in development to reconstruct the complete LPTC circuit of *Drosophila*. Both methods carry the potential to establish a comprehensive view on the morphological foundation of the fly brain.

Direct comparison of electrotonic properties of HS cell models revealed different values (Borst and Haag, 1996) for both flies species. Experimentally measured input resistances show that electrotonic parameters do not compensate for the difference in scale. Considering the similar response properties of the cells in both species (see Fig. 2.4D), synaptic strength and efficacy have to be adjusted to fit the large difference in input resistance in fruit fly LPTCs. Simulation of synaptic inputs into the cells might help to further explore this issue. Experimental measurements were performed using sharp electrodes in *Calliphora* and patch electrodes in *Drosophila* flies. While the former have been shown to introduce higher leak conductances, the latter have unknown influence on ion concentrations (Staley et al., 1992). Patch clamp experiments in *Calliphora* might help to make this interspecies comparison of electrotonic properties more transparent.

Other studies performed in maturing crickets describe constancy of electrophysiological features even with large differences in size (Kamper and Murphey, 1994; Chiba et al., 1992). Interestingly, the functional syntax (e.g. spike timing), but not the absolute response intensity were conserved within growing cricket neurons, supporting the

idea that functional concepts rather than the entire neuronal complexity are encoded genetically (Marder and Goaillard, 2006; Borst, 2008).

In general the number of detailed electrotonic studies in *Drosophila* is quite limited. Nathan Gouwens and Rachel Wilson (Gouwens and Wilson, 2009) described antennal lobe projection neurons with very different function, morphology and electrotonic properties compared to the LPTC cells described here. Electrotonic studies in other giant neurons in other animals reflect the wide diversity of morphological structures and specific parameter values (Yamasaki and Narahashi 1959; Peron et al. 2009; Edwards and Mulloney 1984; for an overview of electrotonic investigations see table 4 in Borst and Haag 1996). Reconstruction of other *Drosophila* LPTCs will allow us to further explore the range of membrane parameters and to correlate the electrotonic architecture and scaling in cells and networks with same function.

Dscam

HS cells are highly polarized neurons with a topographic input arrangement (Schnell et al., 2010; Hausen, 1982). Their arborization pattern and occupied lobula plate territory define the area of synapse formation and the range of visual inputs that a particular HS cell receives (Strausfeld, 1984). It must be assumed that the surrounding neuronal context represents a significant constraint in the determination of the shape of HS cell dendrites.

To investigate the role of this neuronal context in LPTC development the effect of Dscam has been studied. Dscams represent a family of transmembrane proteins that have been shown to mediate the process of adhesion and repulsion of neurites and consequently, have been attributed to essential wiring behaviors such as tiling, self-avoidance and synapse formation. In LPTCs, specific overexpression of one isoform in an otherwise Dscam wildtype background led to significantly reduced spanning fields. This reduction implies that the overexpression of a single Dscam isoform interferes with the molecular cues that normally mediate the outgrowth of the cells. HS cell processes were forced out of the territory that they usually occupy and thus could not establish inhibitory and excitatory synaptic connections with presynaptic columnar neurons in this area anymore (Raghu et al., 2007, 2009). Considering the influence on the response properties, this process should cause motion blindness in areas from which branches are repelled. Indeed, a large gap in the frontal field of view of the fly could be observed in the receptive field of such cells. The dendritic branching deficit in this area caused the input from local motion detectors in the stereotypic and hard-wired visual circuitry (Hiesinger et al., 2006; Fischbach and Hiesinger, 2008; Scott et al., 2002) to be no longer sampled.

Dscam research in *Drosophila* has been performed primarily in electrophysiological and

behaviorally inaccessible neurons of in the medulla in adult flies and Da sensory neurons in larvae (Hattori et al., 2008). Kenyon cells represent the only electrophysiologically accessible system (Murthy et al., 2008), where Dscams have been investigated (Zhan et al., 2004). However, no functional characterization of Dscam profile manipulations has been reported to date. With their planar extension, topological position and electrophysiological accessibility LPTCs fill this gap well. This study is a first step in the establishment of LPTCs as a model system in Dscam protein research.

Many questions remain unresolved. This study focused on the overexpression of one single Dscam isoform out of more than 30.000 in a Dscam wildtype background. It will be interesting to look at LPTCs that completely lack any Dscam protein. Also, different isoforms have to be screened, in wildtype as well as in Dscam null background. In different model networks different Dscam mediated effects have been shown (Hattori et al., 2008) and in this respect the Dscam influence on LPTC morphology has to be mapped in detail. Maybe the initially predicted tiling behavior of HSN and HSE can be induced by other isoforms (Hughes et al., 2007).

This analysis was limited to a spanning field analysis, the detailed branching structure of the Dscam cells could not be faithfully sampled. More specific driver lines might overcome this issue and might open access to the analysis of Dscam's influence on the finer branching pattern of LPTCs. While the LPTCs have been described quite intensively, their input layers are subject to ongoing research (Borst et al., 2010). The idea here is to have independent Dscam control on the topographically arranged presynaptic input on the one hand and the contacting postsynaptic LPTCs on the other. With the lobula plate as reference area this might allow one to thoroughly map Dscam influence on morphology and function like on a two dimensional petri dish.

tools

The tools presented here for the morphological analysis all became part of the TREES toolbox, a Matlab toolbox established and maintained by Dr. Hermann Cuntz. It promotes the applied workflow from cylinder reconstructions to statistics and finally to the generation of synthetic cells and can be freely downloaded and modified. Please refer to the TREES toolbox website (http://www.treestoolbox.org) and the related publication (Cuntz et al., 2010). Reconstruction data can be downloaded on the website of the MPI of Neurobiology (MPI website, http://www.neuro.mpg.de) and have been sent to the Neuromorpho.org internet archive (Neuromorpho.org website, http://www.neuromorpho.org). For raw image data, please contact the author or his affiliated group at the MPI.

Bibliography

G. Ascoli. *Computational neuroanatomy: Principles and methods*. Humana Press Inc., 2002.

G. Ascoli, D. Donohue, and M. Halavi. Neuromorpho.org: a central resource for neuronal morphologies. *J Neurosci*, 27(35):9247–9251, 2007.

G. A. Ascoli. Progress and perspectives in computational neuroanatomy. *Anat Rec*, 257(6):195–207, 1999.

G. A. Ascoli, J. L. Krichmar, R. Scorcioni, S. J. Nasuto, and S. L. Senft. Computer generation and quantitative morphometric analysis of virtual neurons. *Anat Embryol*, 204(4):283–301, 2001.

J. Bilen and N. Bonini. *Drosophila* as a model for human neurodegenerative disease. *Annu Rev Genet*, 39(1):153–171, 2005.

S. Bok. *A quantitative analysis of the structure of the cerebral cortex*. Noord-Hollandsche Uitg.-Mij., 1936.

A. Borst. How does nature program neuron types? *Front Neurosci*, 2(1):4–5, 2008.

A. Borst. *Drosophila*'s view on insect vision. *Curr Biol*, 19(1):R36–R47, 2009.

A. Borst and J. Haag. The intrinsic electrophysiological characteristics of fly lobula plate tangential cells: I. Passive membrane properties. *J Comput Neurosci*, 3(4): 313–336, 1996.

A. Borst and J. Haag. Neural networks in the cockpit of the fly. *J Comp Physiol A Neuroethol Sens Neural Behav Physiol*, 188(6):419–437, 2002.

A. Borst, J. Haag, and D. F. Reiff. Fly motion vision. *Annu Rev Neurosci*, 33:49–70, 2010.

J. Bower, D. Beeman, and A. Wylde. *The book of GENESIS: exploring realistic neural models with the GEneral NEural SImulation System*. Telos, 1998.

V. Braitenberg. Ordnung und Orientierung der Elemente im Sehsystem der Fliege. *Biol Cybern*, 7(6):235–242, 1970.

A. H. Brand and N. Perrimon. Targeted gene expression as a means of altering cell fates and generating dominant phenotypes. *Development*, 118(2):401–415, 1993.

E. Buchner, S. Buchner, and I. Bülthoff. Deoxyglucose mapping of nervous activity induced in *Drosophila* brain by visual movement. *J Comp Physiol A Neuroethol Sens Neural Behav Physiol*, 155(4):471–483, 1984.

J. M. L. Budd, K. Kovács, A. S. Ferecskó, P. Buzás, U. T. Eysel, and Z. F. Kisvárday. Neocortical axon arbors trade-off material and conduction delay conservation. *PLoS Comput Biol*, 6(3):e1000711, 2010.

R. C. Cannon, D. A. Turner, G. K. Pyapali, and H. V. Wheal. An on-line archive of reconstructed hippocampal neurons. *J Neurosci Methods*, 84(1-2):49–54, 1998.

J. J. Capowski. An automatic neuron reconstruction system. *J Neurosci Methods*, 8 (4):353–364, 1983.

B. E. Chen, M. Kondo, A. Garnier, F. L. Watson, R. Püettmann-Holgado, D. R. Lamar, and D. Schmucker. The molecular diversity of Dscam is functionally required for neuronal wiring specificity in *Drosophila*. *Cell*, 125(3):607–620, 2006.

A. Chiba, G. Kamper, and R. Murphey. Response properties of interneurons of the cricket cercal sensory system are conserved in spite of changes in peripheral receptors during maturation. *J Exp Biol*, 164:205–226, 1992.

D. B. Chklovskii and A. A. Koulakov. Maps in the brain: what can we learn from them? *Annu Rev Neurosci*, 27:369–392, 2004.

M. M. Corty, B. J. Matthews, and W. B. Grueber. Molecules and mechanisms of dendrite development in *Drosophila*. *Development*, 136(7):1049–1061, 2009.

H. Cuntz, A. Borst, and I. Segev. Optimization principles of dendritic structure. *Theor Biol Med Model*, 4:21, 2007a.

H. Cuntz, J. Haag, F. Forstner, I. Segev, and A. Borst. Robust coding of flow-field parameters by axo-axonal gap junctions between fly visual interneurons. *Proc Natl Acad Sci U S A*, 104(24):10229–10233, 2007b.

H. Cuntz, F. Forstner, J. Haag, and A. Borst. The morphological identity of insect dendrites. *PLoS Comput Biol*, 4(12):e1000251, 2008.

H. Cuntz, F. Forstner, A. Borst, and M. Häusser. One rule to grow them all: a general theory of neuronal branching and its practical application. *PLoS Comput Biol*, 6(8): e1000877, 2010.

W. Denk and H. Horstmann. Serial block-face scanning electron microscopy to reconstruct three-dimensional tissue nanostructure. *PLoS Biol*, 2(11):e329, 2004.

W. Denk, J. H. Strickler, and W. W. Webb. Two-photon laser scanning fluorescence microscopy. *Science*, 248(4951):73–76, Apr 1990.

B. J. Dickson. Molecular mechanisms of axon guidance. *Science*, 298(5600):1959–1964, 2002.

H. Eckert and D. Dvorak. The centrifugal horizontal cells in the lobula plate of the blowfly, phaenicia sericata. *J Insect Physiol*, 29(7):547–553, 1983.

D. H. Edwards, Jr and B. Mulloney. Compartmental models of electrotonic structure and synaptic integration in an identified neurone. *J Physiol*, 348:89–113, 1984.

F. Eeckman, F. Theunissen, and J. Miller. *Neural network simulation environments*, chapter Nemosys: a system for realistic single neuron modeling, pages 114–135. Kluwer (Boston), 1994.

M. Egelhaaf, J. Haag, and A. Borst. Processing of synaptic information depends on the structure of the dendritic tree. *Neuroreport*, 6(1):205–208, 1994.

Y. M. Elyada, J. Haag, and A. Borst. Different receptive fields in axons and dendrites underlie robust coding in motion-sensitive neurons. *Nat Neurosci*, 12(3):327–332, 2009.

J. F. Evers, S. Schmitt, M. Sibila, and C. Duch. Progress in functional neuroanatomy: precise automatic geometric reconstruction of neuronal morphology from confocal image stacks. *J Neurophysiol*, 93(4):2331–2342, 2005.

K.-F. Fischbach and M. Heisenberg. Neurogenetics and behaviour in insects. *J Exp Biol*, 112:65–93, 1984.

K.-F. Fischbach and P. R. Hiesinger. Optic lobe development. *Adv Exp Med Biol*, 628: 115–136, 2008.

F. Forstner. Die neuroanatomische Modellierung von LPTC in *Calliphora vicina*. Master's thesis, Ludwig-Maximilians Universitaet München, 2005.

F. Forstner, H. Cuntz, B. Schnell, S. V. Raghu, and A. Borst. Functional impact of scaling in identified neurons of the fly. in preparation, 2011.

V. Gauck, M. Egelhaaf, and A. Borst. Synapse distribution on VCH, an inhibitory, motion-sensitive interneuron in the fly visual system. *J Comp Neurol*, 381(4):489–499, 1997.

L. J. Gentet, G. J. Stuart, and J. D. Clements. Direct measurement of specific membrane capacitance in neurons. *Biophys J*, 79(1):314–320, 2000.

P. C. Georges, N. M. Hadzimichalis, E. S. Sweet, and B. L. Firestein. The yin-yang

of dendrite morphology: unity of actin and microtubules. *Mol Neurobiol*, 38(3): 270–284, 2008.

J. Glaser and E. Glaser. Neuron imaging with neurolucida - a pc-based system for image combining microscopy. *Computerized Medical Imaging and Graphics*, 14(5): 307–317, 1990.

P. Gleeson, V. Steuber, and R. Silver. neuroconstruct: a tool for modeling networks of neurons in 3d space. *Neuron*, 54(2):219–235, 2007.

C. S. Goodman. Isogenic grasshoppers: genetic variability in the morphology of identified neurons. *J Comp Neurol*, 182(4):681–705, 1978.

K. G. Götz. Flight control in *Drosophila* by visual perception of motion. *Kybernetik*, 4(6):199–208, 1968.

N. W. Gouwens and R. I. Wilson. Signal propagation in *Drosophila* central neurons. *J Neurosci*, 29(19):6239–6249, 2009.

J. Haag. Dendritische Integration von Bewegungsinformation in den Vertikalzellen der Schmeissfliege *Calliphora erythrocephala*. Master's thesis, Max-Planck-Institut für biologische Kybernetik, Tübingen, 1991.

J. Haag and A. Borst. Neural mechanism underlying complex receptive field properties of motion-sensitive interneurons. *Nat Neurosci*, 7(6):628–634, Jun 2004.

J. Haag, F. Theunissen, and A. Borst. The intrinsic electrophysiological characteristics of fly lobula plate tangential cells: II. Active membrane properties. *J Comput Neurosci*, 4(4):349–369, 1997.

J. Haag, W. Denk, and A. Borst. Fly motion vision is based on reichardt detectors regardless of the signal-to-noise ratio. *Proc Natl Acad Sci U S A*, 101(46):16333–16338, 2004.

R. Hardie. *Progress in Sensory Physiology 5*, chapter Functional organization of the fly retina, pages 1–79. Springer (Berlin, Heidelberg, New York, Tokyo), 1984.

D. Hattori, S. S. Millard, W. M. Wojtowicz, and S. L. Zipursky. Dscam-mediated cell recognition regulates neural circuit formation. *Annu Rev Cell Dev Biol*, 24:597–620, 2008.

H. Haug. History of neuromorphometry. *J Neurosci Methods*, 18(1-2):1–17, 1986.

K. Hausen. Motion sensitive interneurons in the optomotor system of the fly. *Biol Cybern*, 45:143–156, 1982.

K. Hausen. The neural architecture of the lobula plate of the blowfly. *unpublished*, 1984.

R. Hengstenberg. Common visual response properties of giant vertical cells in the lobula plate of the blowfly *Calliphora*. *J Comp Physiol [A]*, 149(2):179–193, 1982.

A. V. M. Herz, T. Gollisch, C. K. Machens, and D. Jaeger. Modeling single-neuron dynamics and computations: a balance of detail and abstraction. *Science*, 314 (5796):80–85, 2006.

P. R. Hiesinger, R. G. Zhai, Y. Zhou, T.-W. Koh, S. Q. Mehta, K. L. Schulze, Y. Cao, P. Verstreken, T. R. Clandinin, K.-F. Fischbach, I. A. Meinertzhagen, and H. J. Bellen. Activity-independent prespecification of synaptic partners in the visual map of *Drosophila*. *Curr Biol*, 16(18):1835–1843, 2006.

D. Hillman. *Intrinsic determinants of neuronal form and function*, chapter Parameters of dendritic shape and substructure: Intrinsic and extrinsic determination?, pages 83–113. Liss (New York), 1988.

D. E. Hillman. *The Neurosciences, Fourth Study Program. Cambridge*, chapter Neuronal shape parameters and substructures as a basis of neuronal form, pages 477–498. MIT Press (Cambridge, MA), 1979.

M. Hines and N. Carnevale. The neuron simulation environment. *Neural Comput*, 9 (6):1179–1209, 1997.

T. Hollingworth and M. Berry. Network analysis of dendritic fields of pyramidal cells in neocortex and purkinje cells in the cerebellum of the rat. *Philos Trans R Soc Lond B Biol Sci*, 270(906):227–264, 1975.

Q. Huang, D. Zhou, and M. DiFiglia. Neurobiotin, a useful neuroanatomical tracer for in vivo anterograde, retrograde and transneuronal tract-tracing and for in vitro labeling of neurons. *J Neurosci Methods*, 41(1):31–43, 1992.

M. E. Hughes, R. Bortnick, A. Tsubouchi, P. Bäumer, M. Kondo, T. Uemura, and D. Schmucker. Homophilic Dscam interactions control complex dendrite morphogenesis. *Neuron*, 54(3):417–427, 2007.

T. Hummel, M. Vasconcelos, J. Clemens, Y. Fishilevich, L. Vosshall, and S. Zipursky. Axonal targeting of olfactory receptor neurons in *Drosophila* is controlled by Dscam. *Neuron*, 37(2):221–231, 2003.

M. Joesch, J. Plett, A. Borst, and D. F. Reiff. Response properties of motion-sensitive visual interneurons in the lobula plate of *Drosophila melanogaster*. *Curr Biol*, 18(5): 368–374, 2008.

G. Kamper and R. Murphey. Maturation of an insect nervous system: Constancy in the face of change. *Comp Biochem Physiol A*, 109(1):23–32, 1994.

H. Krapp, B. Hengstenberg, and R. Hengstenberg. Dendritic structure and receptive-field organization of optic flow processing interneurons in the fly. *J Neurophysiol.*, 79(4):1902–1917, 1998.

J. Livet, T. A. Weissman, H. Kang, R. W. Draft, J. Lu, R. A. Bennis, J. R. Sanes, and J. W. Lichtman. Transgenic strategies for combinatorial expression of fluorescent proteins in the nervous system. *Nature*, 450(7166):56–62, 2007.

M. London and M. Häusser. Dendritic computation. *Annu Rev Neurosci*, 28:503–532, 2005.

L. Luo and J. G. Flanagan. Development of continuous and discrete neural maps. *Neuron*, 56(2):284–300, 2007.

E. R. Macagno, C. Levinthal, and I. Sobel. Three-dimensional computer reconstruction of neurons and neuronal assemblies. *Annu Rev Biophys Bioeng*, 8:323–351, 1979.

Z. F. Mainen and T. J. Sejnowski. Influence of dendritic structure on firing pattern in model neocortical neurons. *Nature*, 382(6589):363–366, 1996.

A. Mann. Teams battle for neuron prize. *Nature*, 467(7312):143, 2010.

E. Marder and J.-M. Goaillard. Variability, compensation and homeostasis in neuron and network function. *Nat Rev Neurosci*, 7(7):563–574, 2006.

H. Markram. The blue brain project. *Nat Rev Neurosci*, 7(2):153–160, 2006.

E. P. Meyer, C. Matute, P. Streit, and D. R. Nässel. Insect optic lobe neurons identi-fiable with monoclonal antibodies to GABA. *Histochemistry*, 84(3):207–216, 1986.

J. P. Miller and J. G. A. Relationships between neuronal structure and function. *J Exp Biol*, 112:129–145, 1984.

Y. Mishchenko, T. Hu, J. Spacek, J. Mendenhall, K. M. Harris, and D. B. Chklovskii. Ultrastructural analysis of hippocampal neuropil from the connectomics perspective. *Neuron*, 67(6):1009–1020, 2010.

M. Muqit and M. Feany. Modelling neurodegenerative diseases in *Drosophila*: a fruitful approach? *Nature Rev Neurosci*, 3(3):237–243, 2002.

M. Murthy, I. Fiete, and G. Laurent. Testing odor response stereotypy in the *Drosophila* mushroom body. *Neuron*, 59(6):1009–1023, 2008.

D. Myatt and S. Nasuto. Improved automatic midline tracing of neurites with neuro-mantic. *BMC Neurosci*, 9(Suppl 1):81, 2008.

O. Olsen, F. Nadim, A. A. Hill, and D. H. Edwards. Uniform growth and neuronal integration. *J Neurophysiol*, 76(3):1850–1857, 1996.

H. Otsuna and K. Ito. Systematic analysis of the visual projection neurons of *Drosophila melanogaster*. I. lobula-specific pathways. *J Comp Neurol*, 497(6):928–958, 2006.

H. Peng, Z. Ruan, D. Atasoy, and S. Sternson. Automatic reconstruction of 3d neuron structures using a graph-augmented deformable model. *Bioinformatics*, 26(12):38–46, 2010.

S. P. Peron, P. W. Jones, and F. Gabbiani. Precise subcellular input retinotopy and its computational consequences in an identified visual interneuron. *Neuron*, 63(6):830–842, 2009.

R. Pierantoni. A look into the cock-pit of the fly. *Cell Tissue Res*, 171(1):101–122, 1976.

P. Prezemyslaw and A. Lindenmayer. *The Algorithmic Beauty of Plants*. Springer (New York, USA), 1996.

S. V. Raghu, M. Joesch, A. Borst, and D. F. Reiff. Synaptic organization of lobula plate tangential cells in *Drosophila*: gamma-aminobutyric acid receptors and chemical release sites. *J Comp Neurol*, 502(4):598–610, 2007.

S. V. Raghu, M. Joesch, S. J. Sigrist, A. Borst, and D. F. Reiff. Synaptic organization of lobula plate tangential cells in *Drosophila*: Dalpha7 cholinergic receptors. *J Neurogenet*, 23(1-2):200–209, 2009.

K. P. Rajashekhar and V. R. Shamprasad. Golgi analysis of tangential neurons in the lobula plate of *Drosophila melanogaster*. *J Biosci*, 29(1):93–104, 2004.

W. Rall. Branching dendritic trees and motoneuron membrane resistivity. *Exp Neurol*, 1:491–527, 1959.

S. Schmitt, J. F. Evers, C. Duch, M. Scholz, and K. Obermayer. New methods for the computer-assisted 3-D reconstruction of neurons from confocal image stacks. *Neuroimage*, 23(4):1283–1298, 2004.

D. Schmucker, J. C. Clemens, H. Shu, C. A. Worby, J. Xiao, M. Muda, J. E. Dixon, and S. L. Zipursky. *Drosophila* Dscam is an axon guidance receptor exhibiting extraordinary molecular diversity. *Cell*, 101(6):671–684, 2000.

B. Schnell, M. Joesch, F. Forstner, S. V. Raghu, H. Otsuna, K. Ito, A. Borst, and D. F. Reiff. Processing of horizontal optic flow in three visual interneurons of the *Drosophila* brain. *J Neurophysiol*, 103(3):1646–1657, 2010.

R. Scorcioni and G. Ascoli. *Connectionist Models of Neurons, Learning Processes, and Artificial Intelligence*, chapter Algorithmic extraction of morphological statistics from electronic archives of neuroanatomy, pages 30–37. Springer, 2001.

E. Scott, T. Raabe, and L. Luo. Structure of the vertical and horizontal system neurons of the lobula plate in *Drosophila*. *J Comp Neurol*, 454(4):470–481, 2002.

S. Senft. *Neural-Network Models of Cognition - Biobehavioral Foundations*, chapter A statistical framework to present developmental neuroanatomy, pages 37–57. Elsevier, 1997.

J. Shi, B. Schnell, V. Haikala, F. Forstner, H. He, M.-L. Erfurth, D. Schmucker, A. Borst, and D. F. Reiff. Dscams control dendritic shape and motion processing and are behaviorally relevant in *Drosophila*. in preparation, 2011.

D. A. Sholl. Dendritic organization in the neurons of the visual and motor cortices of the cat. *J Anat*, 87(4):387–406, 1953.

M. Sokolowski. *Drosophila*: genetics meets behaviour. *Nature Rev Genet*, 2(11): 879–890, 2001.

C. Sotelo. Viewing the brain through the master hand of ramón y cajal. *Nat Rev Neurosci*, 4(1):71–77, 2003.

K. J. Staley, T. S. Otis, and I. Mody. Membrane properties of dentate gyrus granule cells: comparison of sharp microelectrode and whole-cell recordings. *J Neurophysiol*, 67(5):1346–1358, 1992.

N. Strausfeld. *Atlas of an insect brain*. Springer (Berlin), 1976.

N. J. Strausfeld. *Photoreception and vision in invertebrates*, chapter Functional neuroanatomy of the blowfly's visual system, pages 483–522. Plenum Press, New York London, 1984.

K. L. Sukontason, T. Chaiwong, S. Piangjai, S. Upakut, K. Moophayak, and K. Sukontason. Ommatidia of blow fly, house fly, and flesh fly: implication of their vision efficiency. *Parasitol Res*, 103(1):123–131, 2008.

D. Turner, H. Wheal, E. Stockler, and H. COLE. *Cellular neurobiology: a practical approach*, chapter Three-dimensional reconstructions and analysis of the cable properties of neurons, pages 225–239. Oxford University Press, USA, 1991.

C. Uehara, C. Colbert, P. Saggau, and I. Kakadiaris. Towards automatic reconstruction of dendrite morphology from live neurons. *Conf Proc IEEE Eng Med Biol Soc*, 3: 1798–1801, 2004.

H. B. Uylings, A. Ruiz-Marcos, and J. van Pelt. The metric analysis of three-dimensional dendritic tree patterns: a methodological review. *J Neurosci Methods*, 18(1-2):127–151, 1986.

H. B. M. Uylings and J. van Pelt. Measures for quantifying dendritic arborizations. *Network*, 13(3):397–414, 2002.

J. van Pelt and U. H. B. *Modeling in the Neurosciences: From Ionic Channels to Neural Networks*, chapter Natural variability in the geometry of dendritic branching patterns., pages 79–108. Amsterdam: Harwood Academic Publishers, 1999.

J. Wang, X. Ma, J. S. Yang, X. Zheng, C. T. Zugates, C.-H. J. Lee, and T. Lee. Transmembrane/juxtamembrane domain-dependent Dscam distribution and function during mushroom body neuronal morphogenesis. *Neuron*, 43(5):663–672, 2004.

F. Weber, H. Eichner, H. Cuntz, and A. Borst. Eigenanalysis of a neural network for optic flow processing. *New J Phys*, 10:015013, 2008.

R. I. Wilson and G. Laurent. Role of GABAergic inhibition in shaping odor-evoked spatiotemporal patterns in the *Drosophila* antennal lobe. *J Neurosci*, 25(40):9069–9079, 2005.

R. I. Wilson, G. C. Turner, and G. Laurent. Transformation of olfactory representations in the *Drosophila* antennal lobe. *Science*, 303(5656):366–370, 2004.

R. y Cajal. *Histology of the Nervous System of Man and Vertebrates*. Oxford University Press, USA;, 1 edition, 1995.

T. Yamasaki and T. Narahashi. Electrical properties of the cockroach giant axon. *J Insect Physiol*, 3(3):230–232, 1959.

T. Yamasaki, T. Isokawa, N. Matsui, H. Ikeno, and R. Kanzaki. Reconstruction and simulation for three-dimensional morphological structure of insect neurons. *Neurocomputing*, 69(10-12):1043–1047, 2006.

R. Yuste and D. W. Tank. Dendritic integration in mammalian neurons, a century after cajal. *Neuron*, 16(4):701–716, 1996.

A. Zador, H. Agmon-Snir, and I. Segev. The morphoelectrotonic transform: a graphical approach to dendritic function. *J Neurosci*, 15(3):1669–1682, 1995.

X.-L. Zhan, J. C. Clemens, G. Neves, D. Hattori, J. J. Flanagan, T. Hummel, M. L. Vasconcelos, A. Chess, and S. L. Zipursky. Analysis of Dscam diversity in regulating axon guidance in *Drosophila* mushroom bodies. *Neuron*, 43(5):673–686, 2004.

H. Zhu, T. Hummel, J. C. Clemens, D. Berdnik, S. L. Zipursky, and L. Luo. Dendritic

patterning by Dscam and synaptic partner matching in the *Drosophila* antennal lobe. *Nat Neurosci*, 9(3):349–355, 2006.

acknowledgments

I would like to thank my supervisor and scientific father Prof. Dr. Alexander Borst. He send me out on this scientific journey with all its adventures and challenges. He always encouraged me to learn and grow, as a person and as researcher. The last few years have been the most exciting ones in my life, thank you Axel.

I would not have been able to reach my destination without the help of my scientific adviser and good friend Dr. Hermann Cuntz. Thank you Hermann, for your unlimited patience, your great professional advice and for encouraging me to think out of the box.

I would like to thank Dr. Jürgen Haag, Prof. Dr. Dierk Reiff and Dr. Shamprasad Varija Raghu for sharing their experience in the field of neuroscience in its various facets. Also, I very much enjoyed to have Prof. Dr. Johannes Müller from the TUM/GSF in my thesis committee who brought a different point of view in our meetings. Thank you.

In Prof. Borst department I had the chance to work and live with exceptional people and I would like thank all of them for their great support, interesting collaborations and all the fun we had.

Finally, I would like to thank my family and friends and in particular my mother for her warm, unlimited, unconditional support. Thank you.

résumé

Friedrich Förstner, Max Planck Institute of Neurobiology, Am Klopferspitz 18, D-82152 Martinsried

forstner@neuro.mpg.de

2006-2010	PhD thesis Max Planck Institute of Neurobiology, Martinsried Department of Systems and Computational Neurobiology Supervised by Prof. Dr. Alexander Borst and Dr. Hermann Cuntz "The morphological identity of insect dendrites"
2005	Diploma thesis Max Planck Institute of Neurobiology, Martinsried Department of Systems and Computational Neurobiology Supervised by Prof. Dr. Alexander Borst and Dr. Hermann Cuntz "Die neuroanatomische Modellierung von LPTC in Calliphora vicina"
2003-2005	Research Trainee Max Planck Institute of Neurobiology, Martinsried Department of Systems and Computational Neurobiology Prof. Dr. Alexander Borst
2002-2003	Research Trainee Max Planck Institute of Biochemistry, Martinsried Protein Analysis, Dr. Friedrich Lottspeich
2001-2006	Undergraduate studies in Bioinformatics Ludwig Maximilian University and Technical University of Munich, Germany
2001	Graduation from High School Albert Einstein Gymnasium, Buchholz in der Nordheide, Germany

publications

J. Shi, B. Schnell, V. Haikala, **F. Forstner**, H. He, M.-L. Erfurth, D. Schmucker, A. Borst, and D. F. Reiff. Dscams control dendritic shape and motion processing and are behaviorally relevant in Drosophila. in preparation

F. Forstner, H. Cuntz, B. Schnell, S. V. Raghu, and A. Borst. Functional impact of scaling in identified neurons of the fly. in preparation

J. Negele, C. Delandre, Y. Zhang, **F. Forstner**, A. W. Moore and G. Tavosanis. The actin bundling protein Fascin operates the distinction between two sensory neuron morphologies, in preparation

H. Cuntz, **F. Forstner**, A. Borst, and M. Häusser. The TREES toolbox - probing the basis of neuronal branching, submitted

A. Ertürk, C. P. Mauch, F. Hellal, **F. Forstner**, T. Keck, K. Becker, N. Jährling, H. Steffens, M. Richter, A. Borst, M. Hübener, E. Kramer, F. Kirchhoff, H. U. Dodt and Frank Bradke. Three-dimensional imaging of the unsectioned adult spinal cord to assess axon regeneration and glial responses after injury, submitted

H. Cuntz, **F. Forstner**, A. Borst, and M. Häusser. One rule to grow them all: a general theory of neuronal branching and its practical application. PLoS Comput Biol, 6(8): e1000877, 2010.

M. C. Kremer, F. Christiansen, F. Leiss, M. Paehler, S. Knapek, T. F. Andlauer, **F. Forstner**, P. Kloppenburg, S. J. Sigrist, G. Tavosanis. Structural long-term changes at mushroom body input synapses. Curr Biol, 20(21):1938-1944, 2010.

B. Schnell, M. Joesch, **F. Forstner**, S. V. Raghu, H. Otsuna, K. Ito, A. Borst, and D. F. Reiff. Processing of horizontal optic flow in three visual interneurons of the Drosophila brain. J Neurophysiol, 103(3):1646-1657, 2010.

H. Cuntz*, **F. Forstner***, J. Haag, and A. Borst. The morphological identity of insect dendrites. PLoS Comput Biol, 4(12):e1000251, 2008.
(* equal contribution)

H. Cuntz, J. Haag, **F. Forstner**, I. Segev, and A. Borst. Robust coding of flow-field parameters by axo-axonal gap junctions between fly visual interneurons. Proc Natl

Acad Sci U S A, 104(24):10229-10233, 2007